SIMULATIONS FOR AN EXPANDING GAS JET WITH JOULE-THOMSON COOLING

MASTER THESIS

Stan de Muijnck

Delft University of Technology

TU Delft Delft University of Technology

Challenge the future

SIMULATIONS FOR AN EXPANDING GAS JET WITH JOULE-THOMSON COOLING

MASTER THESIS

by

Stan de Muijnck

in partial fulfillment of the requirements for the degree of

Master of Science
in Mechanical Engineering

PE report number 2874

at the Delft University of Technology,
to be defended publicly on Thursday January 18, 2018 at 10:00 AM.

Student number:	4102290	
Supervisor:	Prof. dr. ir. R.A.W.M. Henkes	TU Delft
Thesis committee:	Dr. ir. F.F.J. Schrijer,	TU Delft
	Dr. ir. M.J.B.M. Pourquie	TU Delft

TU Delft Delft University of Technology

PREFACE

First and foremost I would like to thank one of my supervisors in this project, Ruud Henkes: without him I would be completely lost in the jungle of this Master Thesis project.

I would also like to thank Ferry Schrijer and Mathieu Pourquie, for their contributions during the different stages of this project.

A great thanks in this preface goes out to my parents (Bram and Hermien), brother (Tom), girlfriend (Puck) and her parents (Quinten and Nienke) who were very close to me during the past period. It has been a great personal adventure and experience, but not without their dedication to help me. Thank you for your continued support.

Lastly I also would like to express my gratitude to the staff at the Fluid Flow and Flow Assurance departments of the Shell Technology Centre in Amsterdam for providing me with a pleasant working environment during my stay at their office when I carried out this project.

Stan de Muijnck
Delft, January 2018

ABSTRACT

This study was aimed at improving the accuracy of the model predictions for the minimum fluid and inner wall temperatures for cold, low-pressure start-up of wells that produce oil or gas. Due to the large pressure drop over the well head choke, the so-called Joule-Thomson cooling will give a very low temperature of the expanding gas jet. Low-temperatures can give brittle fracture of the material in the piping downstream of the choke. Models are needed to verify whether the material temperature remains above the lower-design temperature. For the model validation, Imperial College in London (on request by Shell) has carried out lab experiments with argon gas that expands through an orifice from 120 bara to 1 bara. Awaiting the results of the lab experiments, detailed simulations were carried out in the present study using the Fluent CFD programme.

The 3D, steady, compressible Reynolds-Averaged Navier-Stokes equations were solved with the SST $k-\omega$ model for the turbulence. The considered configuration is the same as in the lab. It consists of an upstream chamber with argon at 120 bara, that expands through a 5 mm long orifice with 1.55 mm diameter, into a square outlet section with 50 mm sides and 500 mm length. The inlet temperature is -17 ^{o}C and the outlet pressure is 1 bara. The supersonic flow leaving the orifice reaches a maximum Mach number of about 9, just before a shock to subsonic flow is found. The jet reaches very low temperatures due to isentropic expansion, and reaches the isenthalpic expansion temperature of 196 K (or -77 ^{o}C) downstream of the shock. The jet reaches the sides of the outlet at a distance of about 100 mm.

The maximum Mach number of about 9 predicted by Fluent is higher than the value of about 6 found in a previous simulation study that used the STAR-CCM+ CFD programme. To verify the Fluent results, the distributions of grid cells was varied and the number of grid cells was increased. Also, a MATLAB programme was written that solved the inviscid compressible equations (Euler equations) for an axisymmetric jet. This confirmed the Fluent results.

In addition to the 3D square outlet section, also 3D and 2D Fluent simulations were carried out for a cylindrical outlet (using a hydraulic diameter of 50 mm). The maximum Mach number and the jet structure (velocity, temperature) are not affected by the side walls. This is because the side walls are sufficiently far from the jet.

Furthermore, the temperature and the heat transfer at the walls of the outlet section were investigated. Thereto both adiabatic and non-adiabatic walls were considered. The ambient temperature is 20 ^{o}C. Thermal boundary layers are formed along the side walls, that are exposed to a temperature of 196 K (the isenthalpic expansion temperature) in the centre of the pipe, up to a distance of about 1.5 m, where the outer edge of the boundary layer reaches the centre of the pipe. Thereafter the centre line temperature increases due to heat inflow from the ambient.

List of Symbols

a	Local speed of sound $[ms^{-1}]$
hc	Heat transfer coefficient $[W \cdot m^{-2} \cdot K^{-1}]$
$k-\epsilon$	Type of turbulence model
$k-\omega$	Type of turbulence model
$\dot{m}$	Mass flow rate$[kg \cdot s^{-1}]$
w	Wavelength of shock diamond [m]
y^+	Dimensionless viscous wall distance [-]

A	Area $[m^2]$
A_e	Critical area $[m^2]$
D_e	Diameter of the nozzle [m]
D_m	Diameter of the Mach disc [m]
E	Total internal energy $[J]$
F	Force $[N]$
H	Total enthalpy $[J]$
K_e	Thermal conductivity $[W \cdot m^{-1} \cdot K^{-1}$
L	Length $[m]$
M	Mach number defined as V/a [-]
NPR	Normal Pressure Ratio [-]
P	Pressure $[bara]$
P_0	Upstream pressure or stagnation pressure $[bara]$
P_e	Pressure at the exit of the nozzle [bara]
P_{out}	Downstream pressure [bara]
Q	Heat flux $[W \cdot m^{-2}]$

Q	Work $[J]$
R_g	Universal gas constant $[J^{-1} \cdot mol^{-1} \cdot K^{-1}]$
Re	Reynolds number [-]
S	Schlieren function
S	Surface $[m^2]$
T	Temperature $[K]$
T_0	Stagnation temperature $[K]$
V	Velocity $[m \cdot s^{-1}]$
V	Volume $[m^3]$
x_m	Location of the Mach disc [m]
ϵ	Turbulent dissipation rate $[m^2 \cdot s^{-3}]$
γ	Ratio of specific heat capacity of gas, c_p/c_v [-]
κ	Turbulent kinetic energy $[m^2 \cdot s^{-2}]$
λ	Eigenvalue of the compressible flow system
μ	Mach angle [rad]
μ_{JT}	Joule-Thomson coefficient $[bar \cdot K^{-1}]$
ν	Kinematic viscosity of fluid $[m^2 \cdot s^{-1}]$
ν_{pm}	Prandtl-Meyer angle [rad]
ω	Turbulent dissipation rate $[J \cdot kg^{-1} \cdot s^{-2}]$
ρ	Density $[kg \cdot m^{-3}]$
ρ_0	Stagnation density $[kgm^{-3}]$
σ	Shock angle [rad]
Γ	Gas dynamical characteristic
Θ	Flow angle [rad]

CONTENTS

1

INTRODUCTION

A well is a subsurface pipe that is designed to bring hydrocarbon gas and oil from the reservoir to the surface. In an oil well usually some natural gas is co-produced, and in a gas well usually some condensate (light oil) is co-produced. Furthermore often water is produced in addition to the hydrocarbons.

A well that is designed to produce mainly or only gas can be indicated as a gas well. The production from the well can be started or stopped by opening or closing the choke valve at the top of the well (i.e. the well head). Just before opening the valve, there is a large pressure drop over the valve (typically 50 to 300 bar). When the flow goes through the valve with such a large pressure drop, there is also a large temperature drop that will cool down the steel of the piping downstream of the well head to very low temperatures. This is due to the so-called Joule-Thomson effect, wherein a gas will be cooled down during a depressurization. With a composition of gas rich in light fractions (methane, ethane) and a large pressure difference the fluid temperature can drop to a value as low as -100 °C. In this low temperature range there is an increased risk of brittle fracture of materials (sudden failure without plastic deformation), which poses a significant risk to the asset integrity.

There are various incidents in the oil and gas industry that are due to this low-temperature phenomenon. In September 1998 the Esso plant at Longford in Victoria (Australia) had a major fire. Two men were killed and the state's gas supply was interrupted for two weeks, causing chaos in the local industry and considerable hardship in houses which were dependent on the domestic gas supply. What happened was that a warm liquid system (known as the "lean oil" system) failed, allowing a metal heat exchanger to become intensely cold and therefore brittle. When operators tried to reintroduce warm lean oil, the vessel was fractured and released a large quantity of gas which found an ignition source and exploded. Figure 1.1 denotes the failure of the heat exchanger after the explosion, according to [19].

As follow-up to this serious brittle fracture incident, a number of guidelines have been developed for the design of new structures and the maintenance of existing assets subjected to low temperatures. Avoiding brittle fracture is one of the main Process Safety Basic Requirements, PSBR 8, used within Shell [6].

To control the flow in a well, a choke valve is used at the well head. When gas flows through this choke valve during a cold, low-pressure start-up, the large pressure drop leads to supersonic flow with shock waves formed downstream of the choke. The initial flow expansion through the choke is isentropic, which results in a very low fluid or gas temperature upstream of the shock. The larger the pressure drop, or the larger the expansion ratio, the stronger the shock and the lower the minimum fluid temperature. Thus, the accurate prediction of the location and strength of the shock is necessary for the thermal behaviour in the choke.

One of the operations in which very low temperatures are a concern is the already mentioned cold, low-pressure start-up of a well. This scenario is carried out as follows:

- After normal production, the well has been shut-in for a long period of time such that it has reached ambient conditions ("cold"). For oil wells, a gas cap usually has formed at the top of the well. For gas

wells, the production column of the well will be filled with gas. There will be a high pressure upstream of the closed choke valve (the value of which depends on the reservoir pressure and of the weight of the fluid column in the well).

- The flow line downstream of the wellhead choke has been depressurized to prevent the formation of hydrates at shut-in, which gives a low pressure downstream of the choke.

- The choke valve at the well head is opened. The by-passing gas expands and starts to cooldown the piping immediately downstream of the choke. After some time warmer fluids from the reservoir reach the well head, which stops the cooldown process. The minimum in the temperature found for the materials during this start-up process should not fall below the Lower Design Temperature (LDT).

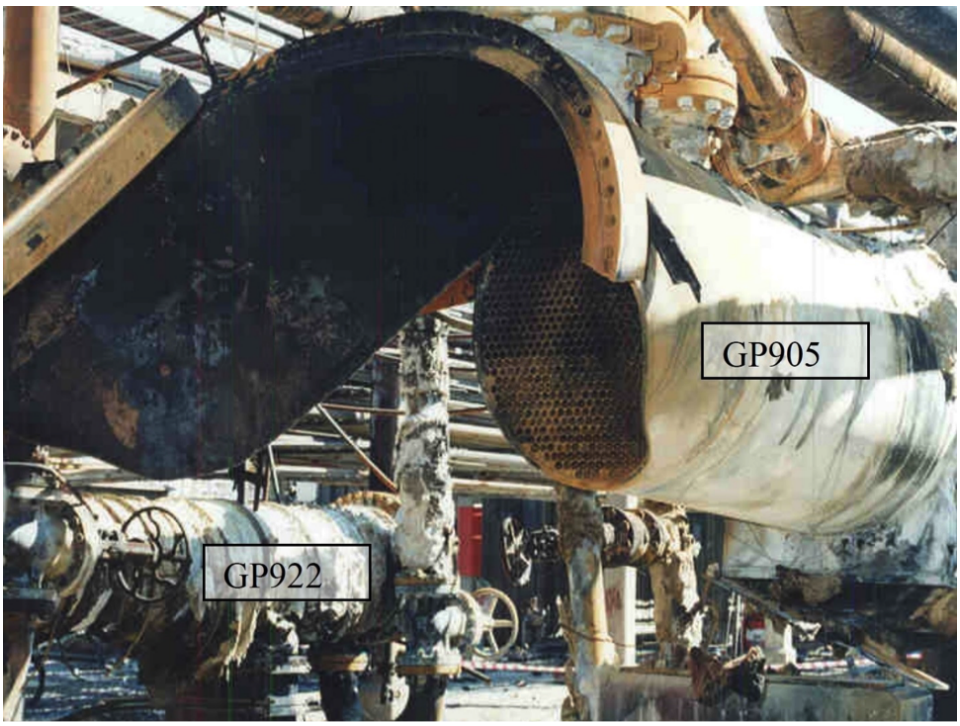

Figure 1.1: Cold brittle fracture at the heat exchanger after the Esso Longford gas explosion.

1.1. RESEARCH GOAL

Shell Projects and Technology has asked Imperial College in London to set up an experiment to study the flow field and the heat transfer from the flowing fluid to the pipe wall for the expanding gas through an orifice. In this experiment an argon jet was expanding from 120 bara to ambient pressure into a rectangular box, where four wall boundaries are defined. In parallel to this experiment CFD calculations have been carried out using the commercial package STAR-CCM+, the results of which are given in [17]. In order to further validate and completely understand the simulations, a second commercial CFD package, Fluent, has also been applied. This modelling in Fluent is the topic of the present Master Thesis.

The overall goal of this thesis is to determine how Joule-Thomson cooling induced by an expanding real gas jet through an orifice affects the cooldown of the surrounding wall materials. The Fluent results were also compared with the existing simulation results obtained with STAR-CCM+. It was found that the two CFD tools gave different results although the input was quite similar. To clarify this difference in the flow field a mesh dependence study was carried out. Furthermore a MATLAB model was built, that solved the inviscid, incompressible flow equations. This allowed comparing the inviscid results with the viscous results obtained with STAR-CCM+ and Fluent.

1.2. METHOD

The ultimate goal of this study is to use Computational Fluid Dynamics to obtain an accurate estimation of the temperature of the fluid and of the inner wall for an expanding gas layer through a valve with high pressure drop. This can help to improve the guidelines for the design of the cold, low-pressure start-up of wells, eliminating the risk of brittle fracture.

In the lab experiment and in the simulation model the choke inlet and choke outlet were both 1.55 mm in diameter The fluid at 256 K was expanded through the nozzle from 120 bara to 1 bara. Simulations were made with both the inviscid and viscous, compressible equations. Both the ideal gas and the real gas descriptions were used. The well-known analytical 1D solution for the inviscid, compressible equations with an ideal gas (gas dynamics) was considered. In addition the two-dimensional, axi-symmetric inviscid gas dynamics theory has been used in a MATLAB solver for an even better description. The solver applied the method of characteristics for a supersonic rotational flow. These inviscid solutions were also compared with the FLUENT results. The latter are obtained by solving the viscous flow equations (RANS, Reynolds-Averaged Navier-Stokes Equations), using a $k-\omega$ model for the turbulence.

The effects of real gas properties and of the gas viscosity on the minimum temperature were also evaluated. The minimum temperature is lower for a real gas than for an ideal gas due to Joule-Thomson cooling (J-T cooling), which is zero for ideal gas. The fluid was chosen to be argon, because it has a cooling J-T coefficient that is comparable to methane gas (note that in the experiments carried out a Imperial College, it was saver to use argon than methane). The overall cooling far enough downstream of the choke, where velocities were low enough, was only due to J-T cooling (isenthalpic expansion) and was independent of the choke size. Thus, to account for J-T cooling, it is important to model the fluid as a real gas. The outlet temperature due to J-T cooling was calculated to be 196 K, a 60 K drop from the inlet temperature. The calculations were firstly done with an adiabatic wall condition (Neumann boundary conditions). Thereafter also Dirichlet (or first-type) boundary conditions were used at the walls, and the heat transfer through the wall was determined from the simulation results.

1.3. SOFTWARE

Three software programs were used in this thesis. The first one is Fluent, which is an ANSYS CFD package. This tool was used to execute the CFD simulations. Computational power was obtained by clusters from Shell and the TU Delft to speed up the calculations. The second program was MATLAB, in which we programmed a solver for the inviscid gas dynamics of a supersonic jet. Furthermore MATLAB was used to create the plots from the CFD results. The third program used in this thesis is a thermodynamic tool, REFPROP or Flashmate, which can calculate the Joule-Thomson cooling from applying an isenthalpic flash from a high pressure to a low pressure.

2

PRINCIPLES OF FLUID FLOW IN A FREE UNDER-EXPANDED JET

In order to understand the principles of the fluid flow trough a nozzle, the basic physics of the nozzle flow and the resulting jet have to be explained. This can help to understand the benchmark results obtained with the detailed simulations that will be considered in the next chapters of this thesis.

2.1. ORIFICE/NOZZLE

In fluid dynamics, the (subsonic) velocity of a fluid parcel will increase when it passes through a constriction, in accordance with the principle of mass continuity, while the static pressure must decrease in accordance with the principle of conservation of mechanical energy. Thus any gain in kinetic energy that a fluid parcel may obtain due to its increased velocity through a constriction is balanced by a drop in the pressure. By measuring the change in pressure, the flow rate can be determined, as is done in various flow measurement devices such as venturi meters, venturi nozzles and orifices.

The Venturi effect [7], which also occurs in an orifice, is the reduction in fluid pressure that results when a fluid flows through a constricted section (or choke) of a pipe. The Venturi effect is named after an Italian physicist: Giovanni Battista Venturi (1746–1822).

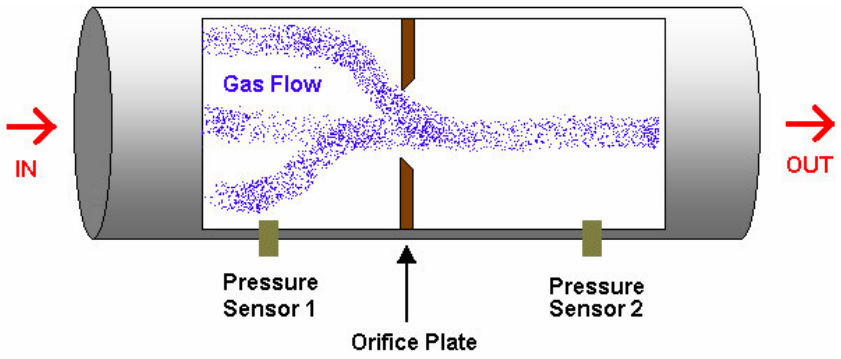

Figure 2.1: Orifice geometry with sharp edge.

2.1.1. CHOKED FLOW

Choked flow is a phenomenon that limits the mass flow rate of a compressible fluid flowing through nozzles, orifices and sudden expansions. The limiting case is when a fluid reaches the state of choked flow, where the fluid velocity approaches the local speed of sound (Mach number $M = V/a = 1$). Generally speaking it is the mass flux after which a further reduction in the downstream pressure or the further increase of the upstream

pressure will not result in an increase in mass flow rate. Choked flows do not only occur during a well start-up but also in power generation and in chemical process industries where, without a more precise knowledge of the critical flow behaviour, the safety or performance of a system may be compromised.

Choked flows come in a variety of shapes depending on the application: from small leakages of pressure vessels [9] to space applications [8]. In figure 2.1 a schematic is drawn of an orifice geometry with a sharp edge. The Normal Pressure Ratio (NPR) over the orifice plays a crucial role in the expansion characteristics of the gas, denoted by:

$$NPR = \frac{P_0}{P_{out}}, \tag{2.1}$$

where P_0 is the upstream pressure (assuming a large reservoir with zero fluid velocity) and P_{out} is the (static) downstream pressure. The critical pressure ratio is obtained when there is choked flow (or critical flow) in the throat of the orifice or valve, which is when :

$$\frac{P_0}{P^*} = (\frac{2}{\gamma+1})^{\frac{-\gamma}{\gamma-1}}, \tag{2.2}$$

where γ is the ratio of the specific heat capacities of the gas (i.e. $\gamma = c_p/c_v$), P^* is the static downstream pressure, and P_0 is the total upstream pressure. At critical flow the Mach number in the throat is equal to one, i.e. the fluid velocity in the throat is equal to the velocity of sound. If the NPR is lower than the critical value, then sonic flow cannot occur in the throat. If the NPR is higher than the critical value, then the fluid will accelerate towards a Mach number of 1 in the orifice/nozzle and further increase to supersonic properties downstream of the throat. For a choked flow in the nozzle or orifice, the critical area is the same as the area of the nozzle exit:

$$A_c = A_{nozzle} \tag{2.3}$$

The critical quantity is denoted by the sub-script 'c'. The mass flow across a choked nozzle is only dependent on the stagnation pressure P_0 and on the temperature T_0 of a particular ideal gas:

$$m^*_{nozzle} = m^*_c = A_c\sqrt{\frac{\gamma}{R_g}}\frac{P_0}{\sqrt{T_0}}(\frac{2}{\gamma+1})^{\frac{\gamma+1}{2(\gamma-1)}} \tag{2.4}$$

Here R_g is the universal gas constant and T_0 is the upstream temperature. Note that the difference between a nozzle and an orifice is the smoothness of the converging geometry towards the throat. For a nozzle the throat is gradually reached, whereas in an orifice the throat is an abrupt occurrence in the flow stream.

2.1.2. FLOW IN CONVERGING NOZZLES

The compressible flow in a converging nozzle has been studied by many authors like Shapiro [18]. The pressure difference between the two sides of the converging nozzle will result in a jet. The properties of the jet across the length of the nozzle are dependent on the stagnation pressure and temperature and on the area ratio at any point (the area ratio is the ratio of the local cross section and the cross section in the throat). Up to the location where a shock occurs, the flow can assumed to be isentropic. Figure 2.2 describes the isentropic flow through a converging-diverging nozzle (which can also be referred to as a Laval tube). The gas enters the inlet from a wide area (reservoir) which has the stagnation conditions. The gas reaches sonic conditions at the throat where the area section is at its minimum. The gas is expanded isentropically to supersonic conditions in the diverging section. In this section an under-expanded jet is formed which exits the diverging section at the downstream end (note that "under-expanded" refers to a pressure condition that is still above the ambient pressure value).

At any point across the length of the nozzle a Mach number (M) of the flow can be given as function of the cross section area at that point:

$$\frac{A}{A^*} = \frac{1}{M}\left((\frac{2}{\gamma+1})(1+\frac{\gamma-1}{2}M^2)\right)^{(\gamma+1)/(2\gamma-2)} \tag{2.5}$$

The density, pressure and temperature of the gas can be expressed as a function of the local Mach number:

$$\frac{\rho_0}{\rho} = \left(1+\frac{\gamma-1}{2}M^2\right)^{\frac{1}{\gamma-1}} \tag{2.6}$$

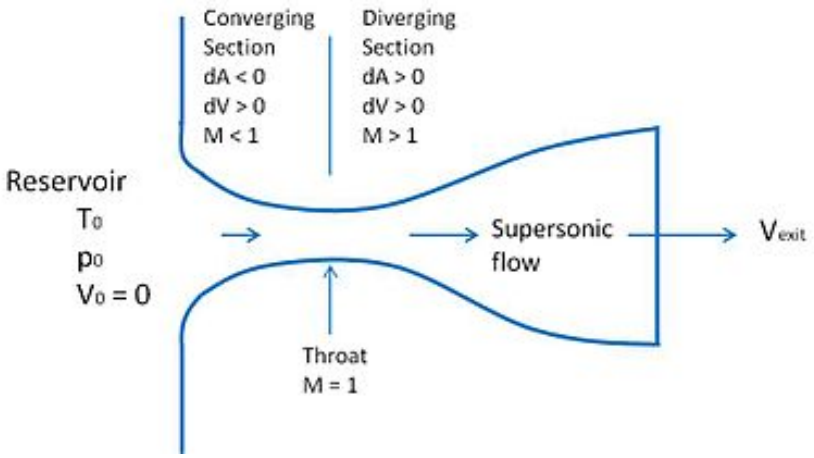

Figure 2.2: Converging-diverging nozzle.

$$\frac{T_0}{T} = 1 + \frac{\gamma - 1}{2} M^2 \tag{2.7}$$

$$\frac{P_0}{P} = \left(1 + \frac{\gamma - 1}{2} M^2\right)^{\frac{\gamma}{\gamma - 1}} \tag{2.8}$$

These expressions are obtained by assuming that the flow can be described by the inviscid, one-dimensional flow equations.

2.1.3. SONIC FLOW IN PIPE SECTION

The compressible fluid flow through constant area nozzles cannot be governed by a changing cross sectional area as given in equation 2.5. The flow is driven by the pressure gradient applied across the length of the nozzle or pipe. Due to the finite viscosity of the flow, a boundary layer will develop along the wall of the pipe section, which leads to a decrease of the apparent pipe diameter, as experienced by the expanding jet. The increasing thickness of the boundary layer can thus lead to a point in the pipe section where the flow reaches a sonic condition. This type of expansion is referred to as a Fanno flow, see [16].

2.2. FREE UNDER-EXPANDED JET

A fluid is initially present in a large reservoir with a total pressure P_0. From here the fluid flow through a nozzle, where it reaches the sonic velocity (see [11]). At the exit of when it further expands in downstream direction. When the pressure of the jet at the exit of the nozzle P_e is higher than that of the ambient back pressure P_{out}, this results in a so-called under-expanded jet. The reservoir pressure is larger than the ambient pressure, which classifies the nozzle as underexpanded. The underexpanded gas jet expands to the atmospheric pressure by means of an expansion fan. The boundary of the freely expanding gas jet causes the expansion waves to be reflected as compression waves.

Figure 2.3 shows the structure of an under-expanded jet emerging from a converging nozzle. The choked flow has $M = 1$ at the exit of the nozzle. At the exit the pressure has the value P_e. Thereafter the fluid expands rapidly through an expansion fan, and the pressure decreases to reach the value P_{out}. The expansion waves intercept the jet boundary and are converted to compression waves, which are deflected towards the centreline. The compression waves converge to form an intercepting shock. Closer to the centreline, the jet flow is forced to turn parallel to the direction of the centreline, which gives the normal (first) shock; this phenomenon is called the Mach disc, named after Ernst Mach who was the first to describe its existence. The second shock is the reflected oblique shock, which is normal to the centreline. The third shock is another oblique shock wave which is reflected at the boundary as an expansion fan. The shocks mark the boundaries between supersonic and subsonic flow regions. In downstream direction this pattern of shocks is repeated which gives a pattern of diamonds with supersonic flow.

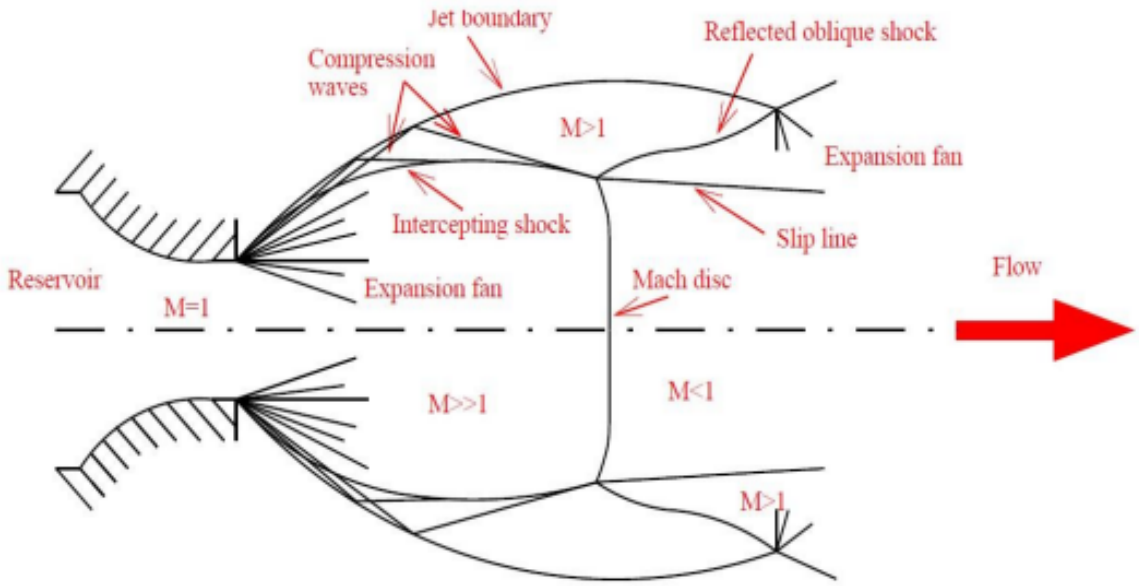

Figure 2.3: Characteristic of the first cell of an underexpanded gas jet.

Large gradients in the pressure and temperature occur when the fluid passes through a normal shock or through a Mach disk. Thus due to the large difference between the reservoir pressure and the ambient pressure, the under-expanded gas jet forms a repeating and decaying series of shock waves and expansions waves until the ambient pressure is reached. There are several parameters that affect the flow pattern for the jet flow discharged from a straight or converged nozzle. These are: the nozzle diameter, the nozzle exit pressure and the ambient pressure. When the pressure ratio is more than two the jet is denoted as a highly under-expanded jet (Ref. [3]).

2.2.1. LABORATORY SUPERSONIC JETS

The jet structures as were shown in the figures above are idealizations of the actual flow. Figure 2.4 shows a more realistic steady-state structure for an over-expanded jet. The Mach reflections that occur have a regular shape, but the mixing layer, which is formed as a result of the Kelvin-Helmholtz instability, changes the supersonic core of the jet. When the mixing layer reaches the axis of the jet, the flow is fully turbulent and subsonic. This is somewhat comparable to the plume of a cigarette; because of the turbulent boundary layer the wave structures within the core are not steady state anymore. However, time-averaging can be applied to the unsteady flow to find, for example, the shock location.

2.2.2. MACH DISK CHARACTERISTICS

Many of these flow structures including Mach disks, barrel shocks, and shear layers, are clearly visible in the flow pattern of an expanding yet. The location, shape and size of such structures, as observed in lab experiments, provide quantitative data that can be used for the validation of the solutions of computational models. For the present study, we have chosen three readily identifiable flow structure dimensions to compare with computational results. These three dimensions, indicated in Fig. 2.5, are: the Mach disk location (x_m), the Mach disk diameter (D_m) and the primary wavelength (w) of the flow, where in figure 2.4 the wavelengths are defined as w_1,w_2 and w_3.

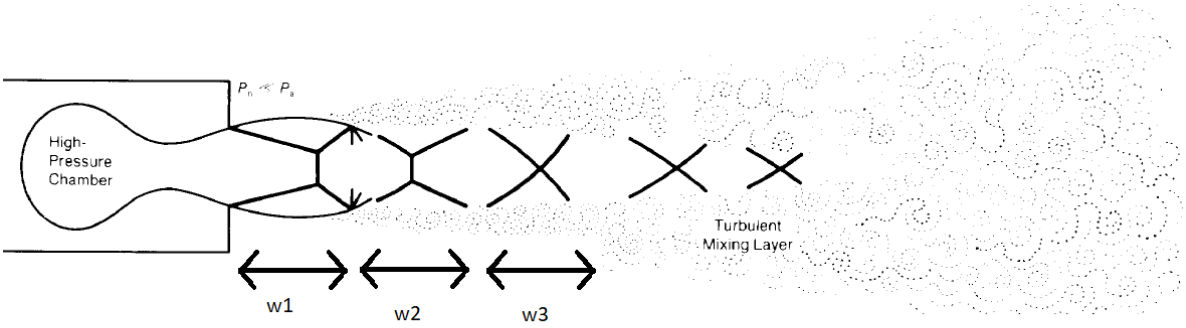

Figure 2.4: Realistic steady-state structure of an over-expanded supersonic jet.

WAVELENGTH

Several theories have been developed for the prediction of the primary wavelength, which is the length of the first periodic segment of the free supersonic jet; see for example Pack et al. [13]. The assumption that the wavelength normalized with the diameter is independent of M and only a function of the ratio between the reservoir pressure and the ambient pressure has turned out to be insufficient. Based on lab experiments there is an empirical relation to describe the variation of w/d. There is a sudden change in the variation of w/d due to the reappearance of the Riemann wave within the jet that occurs at about P_0/P_{out}:

$$\frac{w}{D_e} = 1.52\left(\frac{P_0}{P_{out}}\right)^{0.437} + 0.5\left(\frac{1}{1.55}\sqrt{\frac{P_0}{P_{out}} - 2} - 1\right) \tag{2.9}$$

The yellow curve in figure 2.6 shows the wavelength as function of the NPR.

DIAMETER OF THE MACH DISK

Crist et al. [5] carried out experiments for under-expanded free jets to derive the following empirical expression for the diameter D_m of the Mach disk:

$$\frac{D_m}{D_e} = 0.36\sqrt{\frac{P_0}{P_{out}} - 3.9} \tag{2.10}$$

The red curve in figure 2.6 shows the Mach disk diameter as function of the NPR.

LOCATION OF THE MACH DISK

In addition Love et al. [10] performed an experiment to validate Crist's expression for the location of the Mach disk:

$$\frac{x_m}{D_e} = 0.65\sqrt{\frac{P_0}{P_{out}}} \tag{2.11}$$

The red curve in figure 2.6 shows the location of the Mach disk as function of the NPR.

This relation allows a "local" check of our numerical results in the highly-compressible fluid region. An observation from this empirical relation is the fact that the Mach disc location is not dependent on the thermodynamic parameter γ (fluid nature).

2.2.3. SCHLIEREN PATTERNS

Schlieren methods are often used in experiments of compressible flows to obtain a flow visualization. Schlieren measures the gradient in the fluid density and hence shows any pressure waves in the system. To compare the flow field obtained in simulations with the Schlieren measurements, a numerical Schlieren function can be defined that is based on the density gradient as:

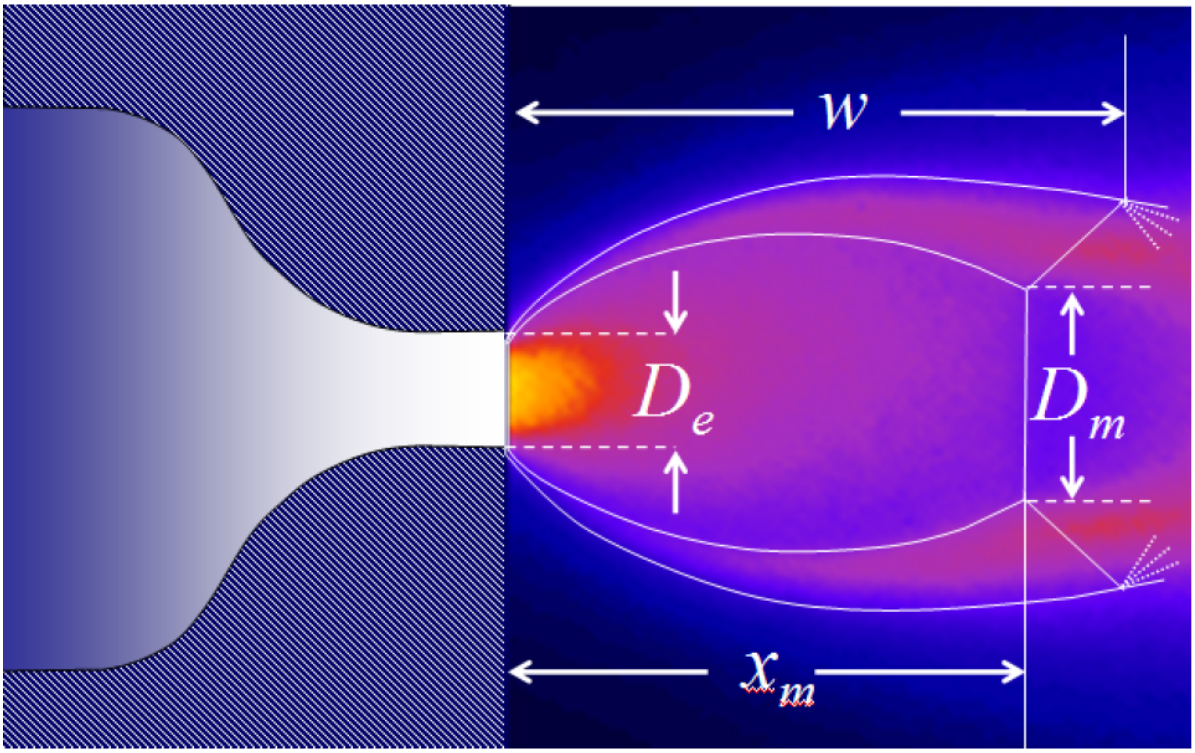

Figure 2.5: Main flow structures of interest, including: the nozzle exit diameter D_e, The Mach disk diameter D_m, the distance to the Mach disk x_m and the primary wave length of the jet w.

$$S = exp(-a\frac{\|\nabla\rho\|}{\|\nabla\rho\|_{max}}) \tag{2.12}$$

Here 'a' is an adjustable parameter, which can be varied to obtain the required contrast between the background and foreground of the image.

2.3. JOULE-THOMSON EFFECT

In thermodynamics, the Joule-Thomson effect or Joule-Kelvin effect explains the increase or decrease in the temperature of an actual gas when it is allowed to expand freely through a valve, or through another throttling device like a nozzle or choke, while being kept fully insulated from the ambient, so that no heat is transferred to or from the gas, and no external mechanical work is extracted from the gas. This gives an isenthalpic expansion. This is referred to as the Joule-Thomson process or the throttling process [15].

The Joule-Thomson effect is named after James Prescott Joule and William Thomson, 1st Baron Kelvin who discovered it in 1852 following an earlier study by Joule on Joule expansion, in which a gas experiences free expansion in a vacuum.

The JT effect does not apply for ideal gases because there is no temperature variation when an ideal gas is allowed to expand through an insulated throttling device. The adiabatic expansion of a gas may be performed in many ways. The change in temperature undergone by the gas during expansion depends not only on the initial and final pressure, but also on the way in which the expansion is performed. If the expansion procedure is reversible, indicating that the gas is in thermodynamic equilibrium at all times, there is an isentropic expansion. Such an isentropic process can be maintained up to the location of a shock.

When a gas expands, the average distance between molecules increases. Due to intermolecular attractive forces, expansion causes an increase in the potential energy of the gas. If no external work is extracted and no heat is transferred, the total energy of the gas remains constant due to the conservation of energy. The increase in potential energy thus indicates a decrease in kinetic energy and therefore a decrease in temperature.

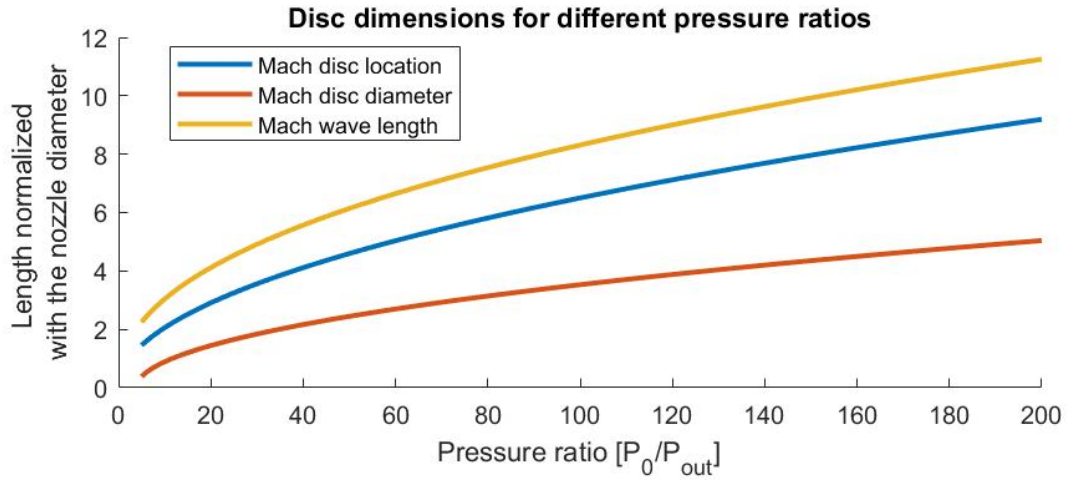

Figure 2.6: Non-dimensionalized lengths of various Mach disk properties.

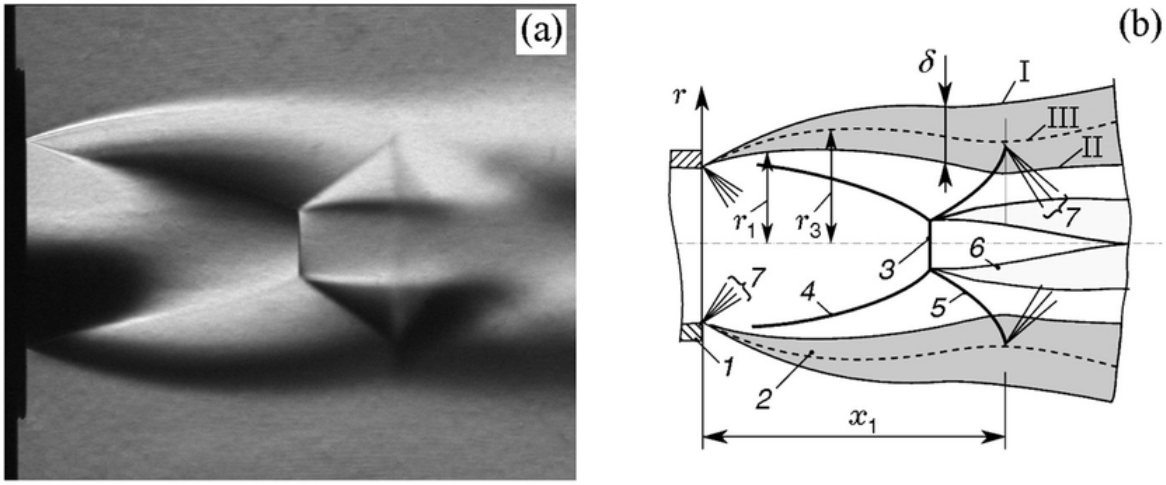

Figure 2.7: Schlieren flow visualization. (Source: [4])

During collisions of gas molecules, kinetic energy is momentarily converted into potential energy. When the average intermolecular distance increases, there is a decrease in the number of collisions per time unit, which causes a drop in the average potential energy. Furthermore, the total energy must be kept constant, thus this causes an increase in kinetic energy (temperature). Below the Joule-Thomson inversion temperature, the former effect (work done internally due to intermolecular attractive forces) at free expansion leads to a drop in the temperature.

In a Joule–Thomson process the enthalpy is kept constant. To verify this, the first step is to calculate the net work done by the gas that moves as a plug. Assume that the gas has a volume of V_1 in region 1 at pressure P_1 and a volume of V_2 when it comes to the region 2 at pressure P_2. Then the work done on the gas by the remainder of the gas in region 1 is P_1V_1. In region 2, the quantity of work done by the gas is P_2V_2. Consequently, the total work done by the gas is:

$$P_1V_1 - P_2V_2 \tag{2.13}$$

Due to the first law of thermodynamics, the change in internal energy plus the work done by the gas is the total quantity of heat absorbed by the gas (here it is assumed that there is no change in kinetic energy). In the Joule-Thomson process the gas is kept insulated, thus no heat is absorbed. This means that

Table 2.1: Joule-Thomson warming or cooling effect.

μ_{jt}	∂p	∂T	J-T effect
+	Always negative	Negative	Cooling
-	Always negative	Positive	Warming

$$E_2 - E_1 + P_2 V_2 - P_1 V_1 = 0 \tag{2.14}$$

where E_1 and E_2 indicate the internal energy of the gas in regions 1 and 2, respectively. The equation above then implies that:

$$H_1 = H_2 \tag{2.15}$$

where H_1 and H_2 indicate the enthalpy of the gas in regions 1 and 2, respectively.

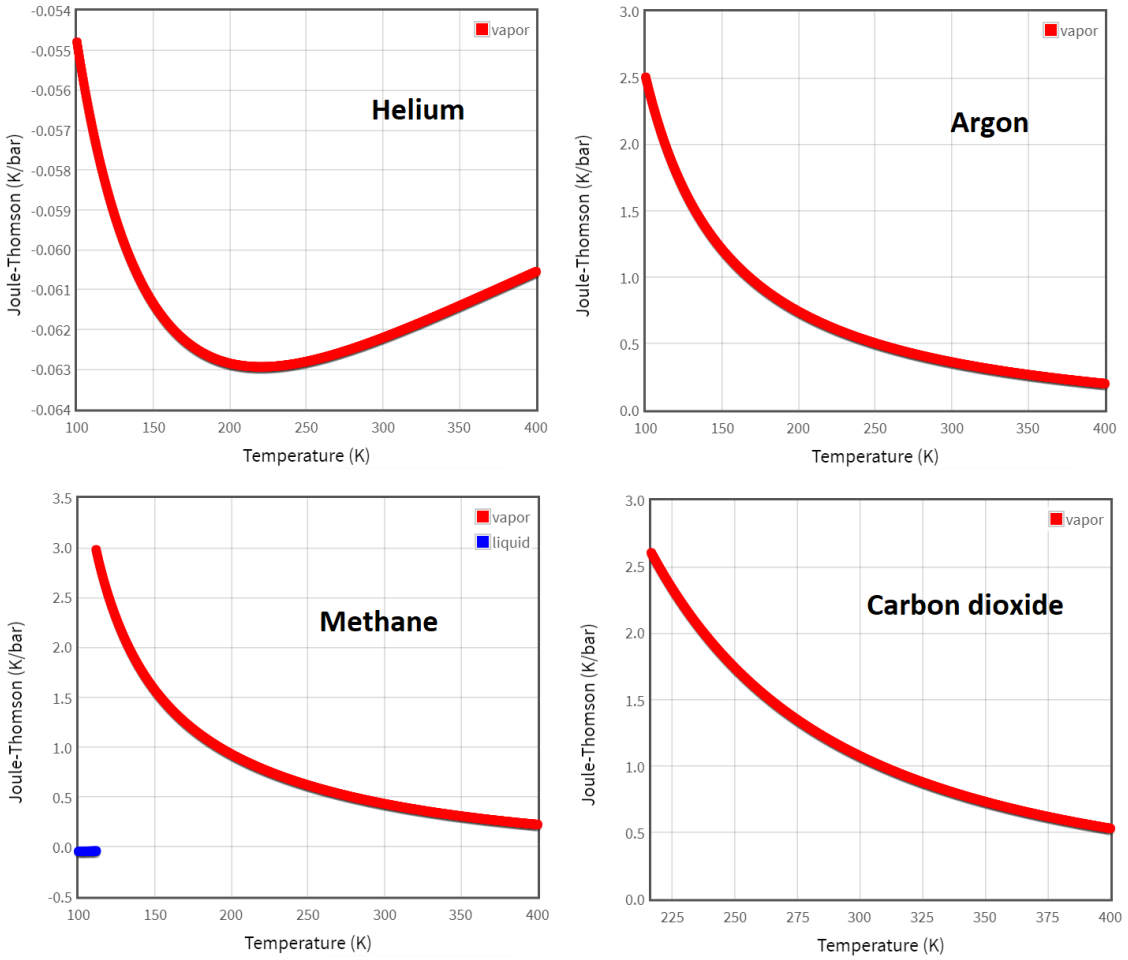

Figure 2.8: Joule–Thomson coefficients for various gases at atmospheric pressure (source: http://webbook.nist.gov/).

The rate of change of temperature T with respect to the pressure P at constant enthalpy H is the Joule–Thomson (Kelvin) coefficient $\mu = (\frac{\partial T}{\partial P})_H$. In a gas expansion the pressure reduces, hence the sign of ∂p is always negative. With that in mind, table 2-1 gives details about when the Joule-Thomson effect cools or warms a real gas.

Hydrogen and helium are, for example, two gases that will warm up during JT expansion at typical room temperatures, whereas on the other hand nitrogen and argon are cooled down by a JT expansion, see figure 2.8.

3

OVERVIEW OF PHYSICAL AND NUMERICAL MODELS

Most simulations in the present study are done using steady, compressible and three-dimensional (and also two-dimensional) conditions. The governing equations defining the physical behaviour are briefly discussed in the next few sections. Some relations will be used in this report. Furthermore an overview is given of the numerical approaches used to solve the system of unknowns. Here a control volume based technique is used to convert the governing equations to algebraic equations that can be solved numerically. This control volume technique consists of integrating the governing equations for each control volume. This yields discrete equations that conserve each quantity on a control volume basis. Both the mass, momentum, and energy conservation equations are solved sequentially.

3.1. INTEGRAL FORM OF THE CONSERVATION LAW

Consider a control volume with a volume V and surface $S = dV$, see figure 3.1. Let dV and dS be a small volume and surface element, respectively. Further let $\bar{n}$ be the outward unit vector normal to dS. The integral form of the conservation laws for mass, momentum and energy are determined as follows (and will be followed by some comments on the different laws):

- Mass conservation:

$$\underbrace{\frac{d}{dt}\int\int\int_V \rho dV}_{1.1} + \underbrace{\int\int_S \rho\bar{V}\cdot\bar{n}dS}_{1.2} = 0 \tag{3.1}$$

- Momentum conservation:

$$\begin{aligned}\underbrace{\frac{d}{dt}\int\int\int_V \rho\bar{V}dV}_{2.1} + \underbrace{\int\int_S \rho\bar{V}\bar{V}\cdot\bar{n}dS}_{2.2} + \underbrace{\int\int_S p\cdot\bar{n}dS}_{2.3} = \\ \underbrace{\int\int\int \rho\bar{f}dV}_{2.4} + \underbrace{\bar{F}_{visc}}_{2.5} + \underbrace{\bar{F}_{external}}_{2.6}\end{aligned} \tag{3.2}$$

- Energy conservation

$$\begin{aligned}\underbrace{\frac{d}{dt}\int\int\int \rho E dV}_{3.1} + \underbrace{\int\int_S \rho E\bar{V}\cdot\bar{n}dS}_{3.2} + \underbrace{\int\int p\bar{V}\cdot\bar{n}dS}_{3.3} = \\ \underbrace{\int\int\int \rho\bar{f}\cdot\bar{V}dV}_{3.4} + \underbrace{Q}_{3.5} + \underbrace{\dot{W}_{visc+ext}}_{3.6}\end{aligned} \tag{3.3}$$

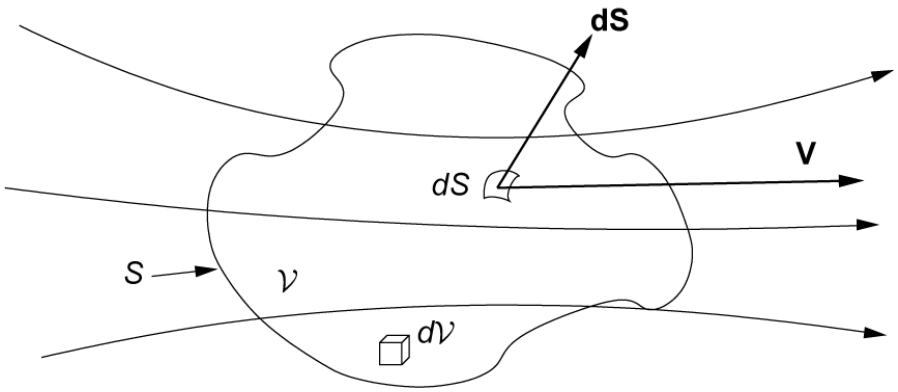

Figure 3.1: Control volume

Comments

1. Mass conservation:
   (a) time rate of change of mass inside volume V
   (b) net mass flow out of volume V through surface S
2. Momentum conservation:
   (a) time rate of change of momentum inside volume V
   (b) net flow of momentum across surface S
   (c) surface force due to pressure p force
   (d) body forces
   (e) viscous forces
   (f) external forces (strut force, enclosure force)
3. Energy conservation:
   (a) time rate of change of energy inside volume V
   (b) net flow of energy across surface S
   (c) work on fluid by pressure p force
   (d) work done by body forces
   (e) heat added to the fluid; radiation, conduction or condensation
   (f) work done by viscous and external forces

The only assumption that has been made is that the integrals are integrable in volume V and over dV. These integrands are allowed to have discontinuities. This makes that the integral forms of the conservation laws widely applicable.

3.1.1. DIFFERENTIAL FORM OF THE FLOW EQUATIONS

To derive the differential form of the flow equation the surface integrals in the integral form have to be transformed into a volume integral by using the divergence theorem and the gradient theorem.

Divergence theorem:

$$\int\int\int_V \nabla \cdot \bar{A} dV = \int\int \bar{A} \cdot n dS \tag{3.4}$$

Gradient Theorem:

$$\int\int\int_V \nabla p dV = \int\int p\tilde{n} dS \tag{3.5}$$

Assuming that V is fixed in space and arbitrarily chosen, the integrand has to be zero for all point in space. This results into:

Continuity equation

$$\frac{\partial \rho}{\partial t} + \nabla \cdot \rho \bar{V} = 0 \tag{3.6}$$

Momentum equation

$$\frac{\partial}{\partial t} \rho \bar{V} + \nabla \cdot \rho \bar{V} \bar{V} + \nabla p = p \bar{f} \tag{3.7}$$

Energy equation

$$\frac{\partial}{\partial t} \rho E + \nabla \cdot \rho \bar{V} E + \nabla \cdot p \bar{V} = p \bar{V} \cdot \bar{f} \tag{3.8}$$

With $H = E + \frac{P}{\rho}$, we have that $\nabla \cdot \bar{V} E + \nabla \cdot p \bar{V} = \nabla \cdot \rho H \bar{V}$.

3.1.2. EULER EQUATIONS

The above equations describe a mathematical model of compressible flows, where the effects of viscosity, heat conduction and external heating have been neglected. When also the the external force is neglected, the following so-called Euler equations are found:

$$\frac{\partial \rho}{\partial t} + \nabla \cdot \rho \bar{V} = 0 \tag{3.9}$$

$$\frac{\partial}{\partial t} \rho \bar{V} + \nabla \cdot \rho \bar{V} \bar{V} + \nabla p = 0 \tag{3.10}$$

$$\frac{\partial}{\partial t} \rho E + \nabla \cdot \rho \bar{V} E + \nabla \cdot p \bar{V} = 0 \tag{3.11}$$

3.2. DISCONTINUITIES IN COMPRESSIBLE FLOW

The Euler equations allow for the appearance of discontinuities or so-called weak solutions, where certain relations hold. Before these relations will be derived, the physical aspects of three different types of discontinuities will be discussed.

3.2.1. SHOCK WAVE

A shock wave [12] is a flow structure that is characterized by an abrupt, nearly discontinuous change in pressure, temperature and density. Shock waves mark a change from supersonic flow to subsonic flow. For steady shocks it is known that the tangential velocity component is constant over the shock while the normal velocity component decrease. A shock wave can be of one of the following types:

- Normal: at 90° (perpendicular) to the flow direction.
- Oblique: at an angle to the flow direction.
- Bow: occurs upstream of the front (bow) of a blunt object when the upstream flow velocity exceeds a Mach number of 1.

3.2.2. SHEAR WAVE

A shear wave moves with the velocity normal to its front. The fluid on either side of the discontinuity has a normal velocity that is equal to the wave velocity. The tangential velocity remains constant across the wave. The motion is perpendicular to the direction of the wave propagation.

3.2.3. CONTACT DISCONTINUITY

A contact discontinuity has a surface with a a jump in p, ρ and T jump, while there is no gas flow across it. Hereby the contact discontinuity is convected with the fluid velocity. An example of a contact discontinuity is the boundary between a supersonic jet and the ambient gas. Often a contact discontinuity and a shear wave are superimposed.

3.2.4. JUMP RELATIONS

Consider a shock discontinuity with the properties ρ_1, u_1, p_1, h_1 upstream of the shock and the properties ρ_2, u_2, p_2, h_2 downstream of the shock. The starting point is formed by the Euler equations and by considering the special case that the discontinuity is steady. The well-known Rankine-Hugoniot relations for steady normal shock waves are as follows:

$$\rho_1 u_1 = \rho_2 u_2 \tag{3.12}$$

$$\rho_1 u_1^2 + p_1 = \rho_2 u_2^2 + p_2 \tag{3.13}$$

$$h_1 + 0.5 u_1^2 = h_2 + 0.5 u_2^2 \tag{3.14}$$

The jump relations are invariant under exchange from 1 to 2. This means that the jump relations cannot tell which state is found upstream of the shock and which state downstream of the shock. Since viscous dissipation and heat conduction take place, the shock is an irreversible process. When it is assumed that there is no external heat addition to the shock, the shock process is adiabatic. For irreversible, adiabatic flow the entropy will increase across the shock, i.e. $ds > 0$. This is called the entropy condition, which determines the allowable direction of the flow through the shock (namely only supersonic upstream of the shock, and subsonic downstream of the shock is physically possible) . From formula 3.12-3.13 many useful relations can be derived:

$$\frac{p_2}{p_1} = 1 + \frac{2\gamma}{\gamma+1}(M_1^2 - 1) \tag{3.15}$$

$$\frac{\rho_2}{\rho_1} = \frac{\gamma+1}{2+(\gamma-1)}\frac{M_1^2}{M_2^2} \tag{3.16}$$

$$\frac{T_2}{T_1} = \{1 + \frac{2\gamma}{\gamma+1}(M_1^2 - 1)\}\frac{2+(\gamma-1)M_1^2}{(\gamma+1)M_1^2} \tag{3.17}$$

where $M_1 = u_1 / a_1$ is the Mach number upstream of the shock.

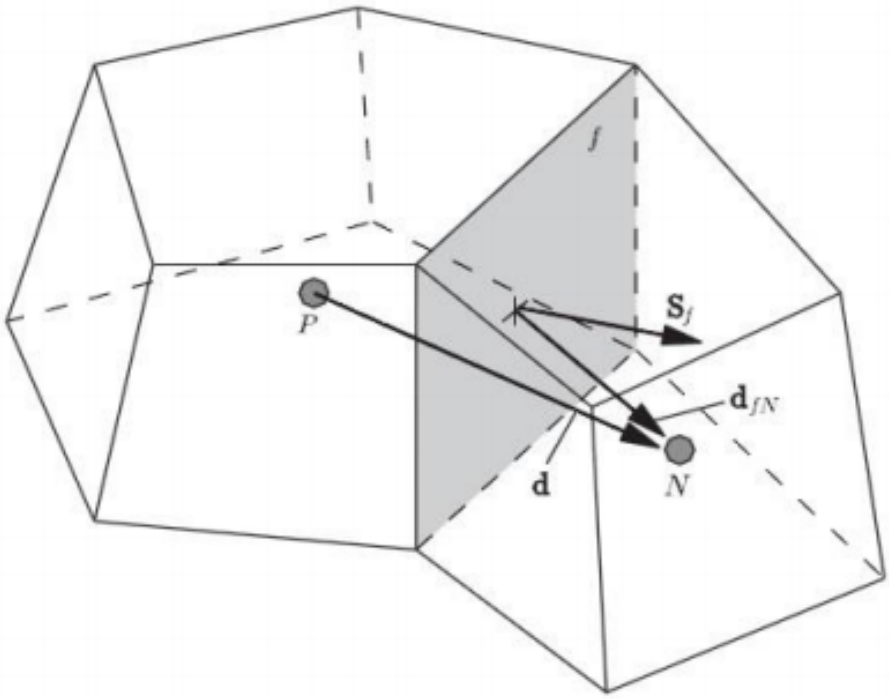

Figure 3.2: Finite volume discretization (Greenshield et al. 2009)

3.3. COMPUTATIONAL METHODS

In the finite volume method the computational domain is divided into several cells or control volumes. Figure 3.2 shows a typical control volume. Neighboring control volumes are connected to each other by a face f represented by the area vector S_f. The figure shows the unknowns P and N at the centres of two neighbouring cells. The partial differential equations (PDEs) are integrated over these control volumes.

The next step is discretization in which the volume and surface integrals are transformed in a set of linear algebraic equation involving values of the fluxes of the primary variable ψ_f. The values of the face of the control volumes are found through interpolation of the flux values at the centres ψ_P and ψ_N respectively. The detailed procedure of discretzation and interpolation will be explained in the next sub-sections.

3.3.1. DISCRETIZATION OF CONVECTIVE TERMS

The convective terms in the governing Euler equations are $\nabla\cdot[(\bar{u}\rho)]$,$\nabla\cdot[\bar{u}(\rho\bar{u})]$ and $\nabla\cdot[\bar{u}(\rho E)]$. Each convective term is integrated over the control volume and linearized in the following way.

$$\int_V \nabla\cdot(\bar{u}\psi)dV = \int_S dS\cdot(\bar{u}\psi) = \sum_f S_f\cdot u_f\psi_f = \sum_f \phi_f\psi_f \tag{3.18}$$

Where $\sum_f$ is a summation over all faces and $\phi_f = S_f\cdot u_f$ is the volume of fluid passing through the face per unit time, also known as the volumetric flux.

For obtaining the value of u_f, the central difference method is used which is the linear interpolation of u with respect to the neighbour cells. The value of ψ_f is obtained through spitting the flux in two directions (incoming and outcoming direction). The quantifies are represented as f_+ and f_-. The weighting function α is defined by:

$$\alpha = \frac{\phi_{f+}}{\phi_{f+}+\phi_{f-}} \tag{3.19}$$

The above discretization leads to:

$$\sum_f \phi_f\psi_f = \sum_f [\alpha\phi_{f+}\psi_{f+} + (1-\alpha)\phi_{f-}\psi_{f-}] \tag{3.20}$$

Volumetric fluxes associated with the local velocities can be calculated as follows:

$$\phi_{f+} = |S|\max[(\bar{u}_{f+}+a_{f+}),(\bar{u}_{f-}+a_{f-}),0] \tag{3.21}$$

$$\phi_{f-} = |S|\max[(\bar{u}_{f+}-a_{f+}),(\bar{u}_{f-}-a_{f-}),0] \tag{3.22}$$

Where $a_f\pm$ is the speed of sound at the face, both in outward and inward direction of the owner cell, which can be expressed as

$$a_f\pm = \sqrt{\gamma RT_{fpm}} \tag{3.23}$$

3.3.2. DISCRETIZATION OF GRADIENT TERMS

All the gradient terms of the governing equation are converted from a volume integral into a surface integral through:

$$\int_V \nabla\psi dV = \int_S dS\psi = \sum_f S_f\psi_f \tag{3.24}$$

By using the interpolation procedure of ψ_f with the split in the f_+ and f_- directions, the following discretisation results:

$$\sum_f S_f\psi_f = \sum_f [\alpha S_f\phi_+ + (1-\alpha)S_f\phi_{f-}] \tag{3.25}$$

3.3.3. DISCRITISATION OF LAPLACIAN TERMS

The Laplacian terms are discretised with the diffusion coefficient η for polyhedral meshes in the following way:

$$\int_V \nabla \cdot (\eta \nabla \psi) dV = \int_s dS \cdot (\eta \nabla \psi) = \sum_f \eta S_f \cdot (\nabla \phi)_f \tag{3.26}$$

The evaluation of the diffusion flux $S_f \cdot (\nabla \psi)_f$ is split into orthogonal and non-orthogonal components.

3.3.4. DISCRETIZATION OF TEMPORAL TERMS

The temporal terms in the Euler equations are discritized using the Euler explicit scheme (δt is the time step):

$$\int_V \frac{\partial \psi}{\partial t} = \frac{(\psi^{n+1} - \psi^n) dV}{\delta t} \tag{3.27}$$

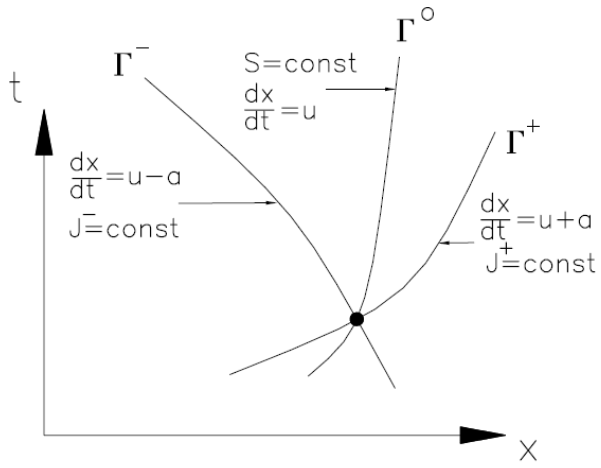

Figure 3.3: The three characteristics

3.4. CHARACTERICS OF THE FLOW

For the numerical discretization of a compressible flow problem an important aspect is the correct treatment of the boundary conditions. Due to the discontinuities in the Euler solution the solution of high velocity compressible flow problems has a wave-like behaviour. By obtaining the eigenvalues of the Jacobian matrix of the flow equations a local speed of propagation of the waves can be found. The eigenvalues for a 3-D compressible flow system obtained as a results of the procedure can be expressed as:

$$\lambda_1 = u - a \quad \text{obtained from the mass equation} \tag{3.28}$$

$$\lambda_1 = u \quad \text{obtained from the momentum equation} \tag{3.29}$$

$$\lambda_1 = u - a \quad \text{obtained from the energy equation} \tag{3.30}$$

3.5. SUPERSONIC JET FLOW

As mentioned before a supersonic jet can be formed by expanding a fluid from a high reservoir pressure reservoir, through a nozzle, into a low-pressure ambient. The distance between successive shocks is dependent on the overall jet pressure. The development of the jet can be calculated by using the method of characteristics. The method of characteristics applied to supersonic flow is described in various text books; details of the derivation are given in [2]. The derivation of the characteristic relations from the conservation equations of mass, momentum and energy is quite straightforward; the present section describes the results as far as relevant for jet flows. Both two-dimensional and axi-symmetric flows are considered, which show a substantial difference in the approach to solve the equations. The characteristic equations for potential flow are used throughout; viscosity is neglected and the entropy and total enthalpy are taken to be constant in the entire flow field.

3.5.1. TWO-DIMENSIONAL PLANAR FLOW

The characteristic equations for two-dimensional flow can be simply expressed in terms of the velocity components u and v, in the x and y directions, along two families of lines. Along the line belonging to the first family defined by

$$t_1 = \frac{dy}{dx}_1 = tan(\theta + \mu) \tag{3.31}$$

the equation

$$du + t_2 dv = 0 \tag{3.32}$$

applies, and along a line belonging to the second family, defined by

$$t_2 = \frac{dy}{dx}_2 = tan(\theta - \mu) \tag{3.33}$$

the corresponding relation is

$$du + t_1 dv = 0 \tag{3.34}$$

Here θ is the direction of the streamline with respect to the x-axis and μ is the Mach angle, $\mu = sin^{-1}(1/M)$. Transforming to polar coordinates q, θ in the hodograph plane defined by

$$\begin{aligned} &u = qcos\theta \quad v = qsin\theta \\ &du = dqcos\theta - qsin\theta d\theta \\ &dv = dqsin\theta + qcos\theta d\theta \end{aligned} \tag{3.35}$$

equations 3.32 and 3.34 can be written as:

$$\frac{dq}{d\theta}\sqrt{1 - \frac{1}{M^2}} = \pm\frac{q}{M} \tag{3.36}$$

or

$$\frac{dq}{q} = \pm tan\mu d\theta \tag{3.37}$$

Here the positive sign corresponds to equation 3.32 and the negative sign to equation 3.34. Replacing q in equation 3.37 by the Mach number with the relation

$$\frac{dM}{M} = \frac{dq}{q}(1 + \frac{\gamma - 1}{2}M^2) \tag{3.38}$$

gives

$$\pm d\theta = \frac{\sqrt{M^2 - 1}dM}{(1 + \frac{\gamma-1}{2}M^2)} \tag{3.39}$$

which can be integrated directly to

$$\pm d\theta = cos^{-1}\frac{1}{M} - \frac{\gamma + 1}{\gamma - 1}tan^{-1}\sqrt{(M^2 - 1)\frac{\gamma - 1}{\gamma + 1}} + \text{Constant} \tag{3.40}$$

ν is the Prandtl-Meyer angle defined as:

$$\pm d\theta = -\nu(M) + \text{Constant} \tag{3.41}$$

The positive sign in equations 3.40 and 3.41 corresponds to equation 3.34, the $(\theta - \mu)$ family, and the negative sign to equation 3.32, the $(\theta + \mu)$ family. Suppose that the flow conditions at two point A and B are known, where A is on a $(\theta + \mu)$ line B is on a $(\theta - \mu)$ line, see figure 3.4. The flow conditions at C where the two lines intersect can be found from equation 3.41. At A and B:

$$\text{Constant}_a = \nu(M_a) - \theta_a \tag{3.42}$$

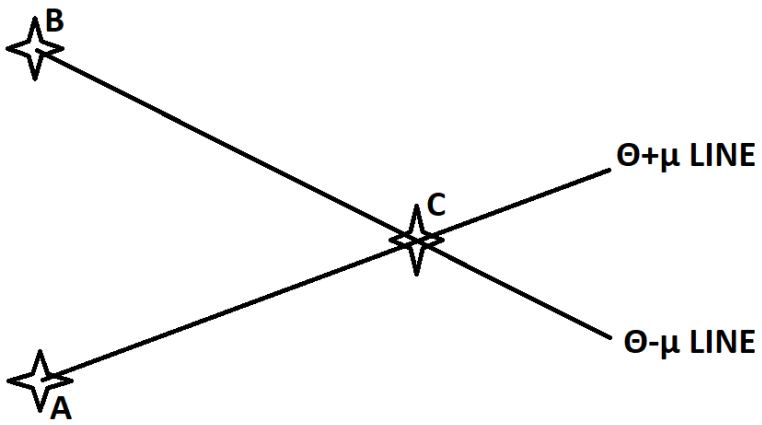

Figure 3.4: General field point intersection of characteristic lines.

$$\text{Constant}_b = \nu(M_b) + \theta_b \tag{3.43}$$

At C, the flow direction θ_c and the Prandtl-Meyer angle are:

$$\theta_c = \frac{\text{Constant}_b - \text{Constant}_a}{2} \tag{3.44}$$

$$\theta_c = \frac{\text{Constant}_a + \text{Constant}_b}{2} \tag{3.45}$$

The coordinates of C are found by using the equations for the characteristic line AC and BC by taking the mean of θ and μ at A and C, B and C:

$$\frac{y_c - y_b}{x_c - x_a} = tan(\frac{\theta_a + \mu_a + \theta_c + \mu_c}{2}) \tag{3.46}$$

$$\frac{y_c - y_b}{x_c - x_b} = tan(\frac{\theta_b - \mu_b + \theta_c - \mu_c}{2}) \tag{3.47}$$

Characteristic lines intersecting with a solid surface of specified shape can be dealt with in a similar manner. Consider a $(\theta - \mu)_b$ line passing through a point B where the flow conditions are known, figure 3.5. A first approximation to the position of C is made by calculating where a straight line of slope $(\theta - \mu)_b$ intersects the surface. As the surface is a streamline; θ_c is known and M_c can be found from equation 3.39. The mean slope of the line BC is then used to calculate a new intersection point C' and the calculation is repeated until the point of intersection does not change anymore.

The boundary that occurs in the calculation of jet flow is a constant (or specified) pressure boundary, 3.6. The Mach number at C is known from the pressure ratio and the streamline direction θ_c can be found from equation 3.39. The coordinates of C are determined from equation 3.40 except that the second equation is replaced by:

$$\frac{y_c - y_b}{x_c - x_b} = tan(\frac{\theta_b + \theta_c}{2}) \tag{3.48}$$

3.5.2. AXISYMMETRIC FLOW

The characteristic equations for supersonic axisymmetric flow are more complexd than the two-dimensional equations because the streamline direction and Mach number depend on the position of the coordinates. The equations corresponding to 3.32 and 3.34 are, along the line defined by

$$t_1 = \frac{dr}{dx}_1 = tan(\theta + \mu) \tag{3.49}$$

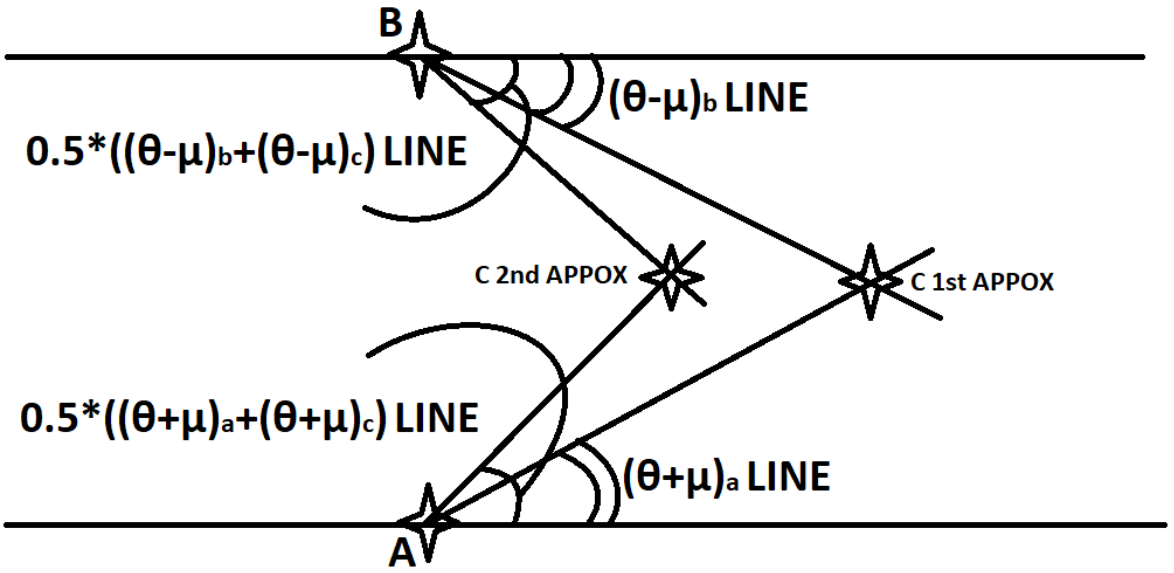

Figure 3.5: Intersection of characteristic lines for asymmetric flow

$$du + t_1 dv + \frac{v}{r(1-\frac{u^2}{a^2})} dx = 0 \tag{3.50}$$

and along the line

$$t_2 = \frac{dr}{dx_2} = tan(\theta - \mu) \tag{3.51}$$

$$du + t_2 dv + \frac{v}{r(1-\frac{u^2}{a^2})} dx = 0 \tag{3.52}$$

where r is the radial coordinate. Transforming to the variables q, θ as before and substituting into equations 3.51 and 3.52 gives:

$$cot\mu \frac{dq}{q} - d\theta - \frac{sin\mu sin\theta}{cos(\theta+\mu)} \frac{dx}{r} = 0 \tag{3.53}$$

$$cot\mu \frac{dq}{q} + d\theta - \frac{sin\mu sin\theta}{cos(\theta-\mu)} \frac{dx}{r} = 0 \tag{3.54}$$

These equations cannot be integrated directly into a Prandtl-Meyer type-like flow because of the presece of the radial coordinate in the last term. A solution for this can be obtained by writing equation 3.51 and 3.52 into a finite difference form and by iterating for the coordinates of the point where the lines intersect and provide the flow conditions at this point.

As before, assume that the flow conditions are known at two point A and B on a different family of lines, see figure 3.6. In finite difference form, equations 3.51 and 3.52 become

$$f_2(q_c - q_a) - (\theta_c - \theta_a) - f_3(x_c - x_a) = 0 \tag{3.55}$$

along the line

$$\frac{r_c - r_a}{x_c - x_a} = f_1 \tag{3.56}$$

and

$$f_5(q_c - q_b) + (\theta_c - \theta_b) - f_6(x_c - x_b) = 0 \tag{3.57}$$

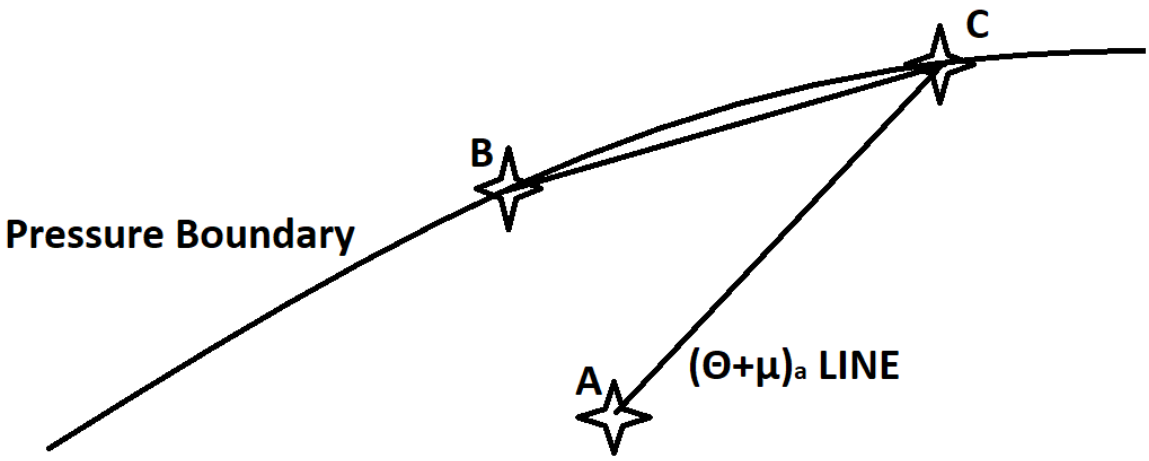

Figure 3.6: Pressure boundary point intersection of characteristic lines

along the line

$$\frac{r_c - r_b}{x_c - x_b} = f_4 \tag{3.58}$$

where, as a first approximation:

$$\begin{aligned} f_1 &= tan(\theta_a + \mu_a) \\ f_2 &= \frac{cot\mu_a}{q_a} \\ f_3 &= \frac{sin\theta_a sin\mu_b}{r_a cos(\theta_a+\mu_a)} \\ f_4 &= tan(\theta_b - \mu_b) \\ f_5 &= \frac{cot\mu_b}{q_b} \\ f_6 &= \frac{sin\theta_b sin\mu_b}{r_b cos(\theta_b-\mu_b)} \end{aligned} \tag{3.59}$$

The expressions for f_1 and f_4 substituted into equations 3.56 and 3.58 give a first approximation for the coordinates of C, and these are substituted into equation 3.55 and 3.57; it will give initial values of q_c and θ_c. The solution is improved by using the conditions calculated for C (similar to equations 3.46 and 3.47):

$$\begin{aligned} f_1 &= tan(\frac{\theta_a+\mu_a+\theta_c+\mu_c}{2}) \\ f_2 &= 0.5 * (\frac{cot\mu_a}{q_a} + \frac{cot\mu_c}{q_c}) \\ f_3 &= 0.5 * (\frac{sin\theta_a sin\mu_b}{r_a cos(\theta_a+\mu_a)} + \frac{sin\theta_c sin\mu_c}{r_c cos(\theta_c+\mu_c)}) \\ f_4 &= tan(\frac{\theta_b-\mu_b+\theta_c-\mu_c}{2}) \\ f_5 &= 0.5 * (\frac{cot\mu_b}{q_b} + \frac{cot\mu_c}{q_c}) \\ f_6 &= 0.5 * (\frac{sin\theta_b sin\mu_b}{r_b cos(\theta_b-\mu_b)} + \frac{sin\theta_c sin\mu_c}{r_c cos(\theta_c-\mu_c)}) \end{aligned} \tag{3.60}$$

The process is repeated by using the latest calculated values at C until convergence is reached. Normally only a few iterations are needed (5-8 iterations). Lines intersecting with a specified surface and points on the pressure boundary can be dealt with as in two-dimensional flow using the appropriate quantities f_i. If there is no inner boundary, the expressions for f_3 and f_6 above cannot be used since r and θ are both zero on the centreline. A limiting form of the expression is used instead, which reads

$$\lim_{\substack{x\to 0 \\ \theta\to 0}} \frac{sin\theta sin\mu}{r cos(\theta \pm \mu)} = \pm[\frac{1}{2} cot\mu \frac{dv}{dx}]_{r=0} \tag{3.61}$$

3.5.3. UNDER-EXPANDED JET

An under-expanded jet exits from the orifice. At the exit the flow is parallel ($\theta = 0$) and has a constant Mach number M_{jet}. For the choked flow configuration the Mach number is one, as was described in section 2.1.1.

The jet exits into quiescent fluid having an ambient pressure p_a. The pressure in the orifice is assumed to be $p_e > p_a$ causing a further expansion of the jet when flowing downstream.

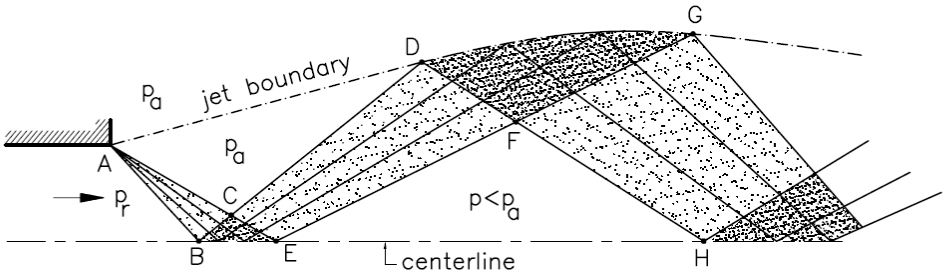

Figure 3.7: Under-expanded jet, $p_{exit} > p_{ambient}$.

The flow is symmetric with respect to the centerline and therefore the discussion can be restricted to the upper part only. Theere are various regions with different conditions. Region ABC contains a simple wave with straight Γ^--characteristics. In region BCE two simple waves intersect. Region ACD is uniform with a pressure that is equal to p_a. Region CDEF contains a simple wave with straight Γ^+-characteristics. Regiion DFG covers both the invariants V^+ and V^-. Region EFH is uniform with a pressure lower than p_a. Region FGHI contains a simple wave V^+ which is uniform; the Γ^--characteristics are straight. Region GIJ is uniform with a pressure equal to p_a. In region HIK two simple waves intersect. The boundary of the exhausting jet is a line of constant pressure p_a. There appears to be a repeated pattern of divergence and convergence of the total jet area.

Figure 3.7 provides a sketch of this flow. The method of characteristics may now be used to find the development of the jet outside the nozzle. At the outer lip of the nozzle exit (point A) a centered expansion appears which reflects on the opposite jet boundary as a compression wave. In the expansion regime the characteristics diverge, and in the compression part they converge to each other. When converging characteristics start to intersect a shock wave will appear and the method of characteristics method breaks down. When continuous waves intersect, the resulting wave pattern depends on the type of waves involved and on the direction of propagation of the incident waves.

$$\sigma_{shock} = tan\frac{(\theta_1 - \mu_1) + (\theta_2 - \mu_2)}{2} \tag{3.62}$$

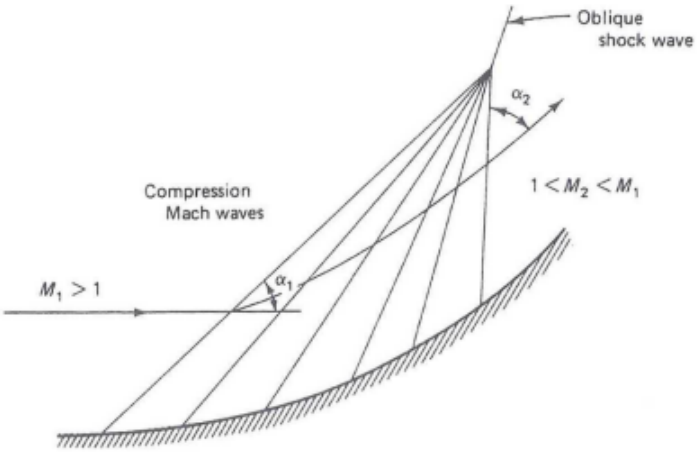

Figure 3.8: Compression waves of the same family converge and ultimately coalesce to form a shock wave.

Compression waves of the same family converge as in 3.8 and ultimately coalesce to form an oblique

shock wave. The initiation of the oblique shock wave has the direction of the first two colliding characteristics. Any shock wave causes a change in the pressure of the flow, an increase in this case. An oblique shock wave is named after the fact that it is inclined at an angle to the direction of the flow passing through it.

On the other hand, a shock wave that is perpendicular to the direction of the flow is called a normal shock wave. A normal shock can be seen in the above diagram when the flow again turns parallel to the centreline. This normal shock creates a Mach disk in the exhaust flow. Passing through this normal shock wave causes the temperature of the flow to increase. The calculation of the shock waves agrees with the shock wave relation explained in chapter 2. Eventually, figure 3.9 gives an overview of the complete flow field (similar to the figures given in chapter 2).

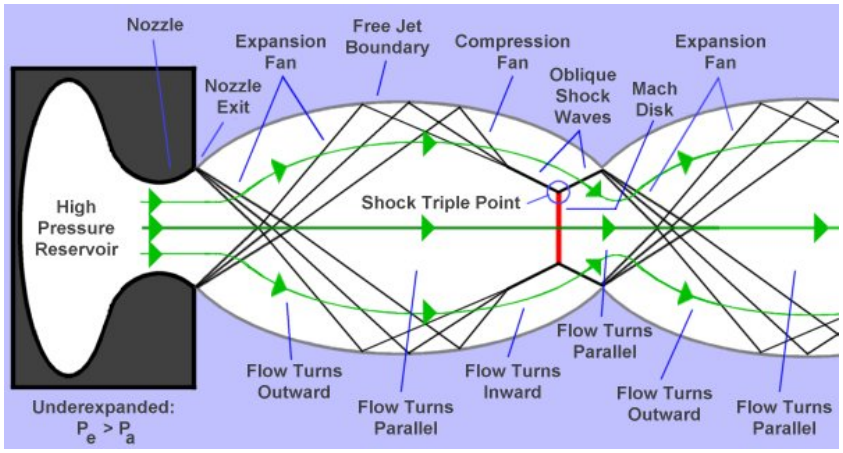

Figure 3.9: Wave structures that create shock diamonds in an under-expanded flow

4

APPLIED COMPUTATIONAL FLUID DYNAMICS METHOD

A numerical algorithm is used in Computational Fluid Dynamics (CFD) to solve fluid flow and heat transfer problems. There are different commercial CFD packages available, among which ANSYS Fluent is considered to be a major tool which is widely used by various industries. The ANSYS Fluent software (from this point referred as Fluent) incorporates the modeling capabilities to describe flow with several features, such as heat transfer, chemical reactions and multiphase flows. The website of fluent [1] was a good helping hand.

To solve the problems the computational domain needs to be divided into cells. The collection of cells is commonly referred to as the 'grid'. Fluent covers the entire flow domain with cells. This allows to resolve boundary layers and any turbulent fluid structures everywhere in detail, and it includes the determination of the local gradients of the velocity and temperature near a wall. These gradients determine the wall shear stress and the convective wall heat transfer. The simulations are based on the finite volume method, which means that for each finite volume (i.e. each grid cell) the conservation equations for mass, momentum (the Navier-Stokes equations) are solved. For specific flows, such as flows with heat transfer or with compressibility, an additional conservation equation is solved, which is the energy equation 3.3.

An important feature in fluid flow was first observed by Osborne Reynolds [14], who characterized pipe flow by a single non-dimensional parameter, known as the Reynolds number Re:

$$Re = \frac{UL}{\nu} \tag{4.1}$$

Here U and L are characteristic velocity and length scales of the flow and ν is the kinematic viscosity of the fluid. The gas flow considered in the present study has a high Reynolds number, which results in a fully turbulent flow.

4.1. FLOW SOLVERS

Fluent allows the user to to choose one of the two numerical solvers:

- Pressure-based solver
- Density-based solver

Historically speaking, the pressure-based approach was developed for low-speed incompressible flows, while the density-based approach was mainly used for high-speed compressible flows. However, recently both methods have been extended and reformulated to enable solving a wide range of flow conditions beyond their original intent. In both methods the velocity field is obtained from the momentum equations. In the density-based approach, the continuity equation is used to obtain the density field while the pressure field is determined from the thermodynamic equation of state.

On the other hand, in the pressure-based approach, the pressure field is extracted by solving a pressure or pressure correction equation which is obtained by manipulating the continuity and momentum equations.

4.1.1. DENSITY-BASED SOLVER

The density-based solver solves the governing equations of continuity, momentum, and (where appropriate) energy simultaneously (i.e. in coupled). Because the governing equations are non-linear (and coupled), several iterations of the solution loop must be performed before a converged solution is obtained. Each iteration consists of the steps illustrated in figure 4.1 and outlined below:

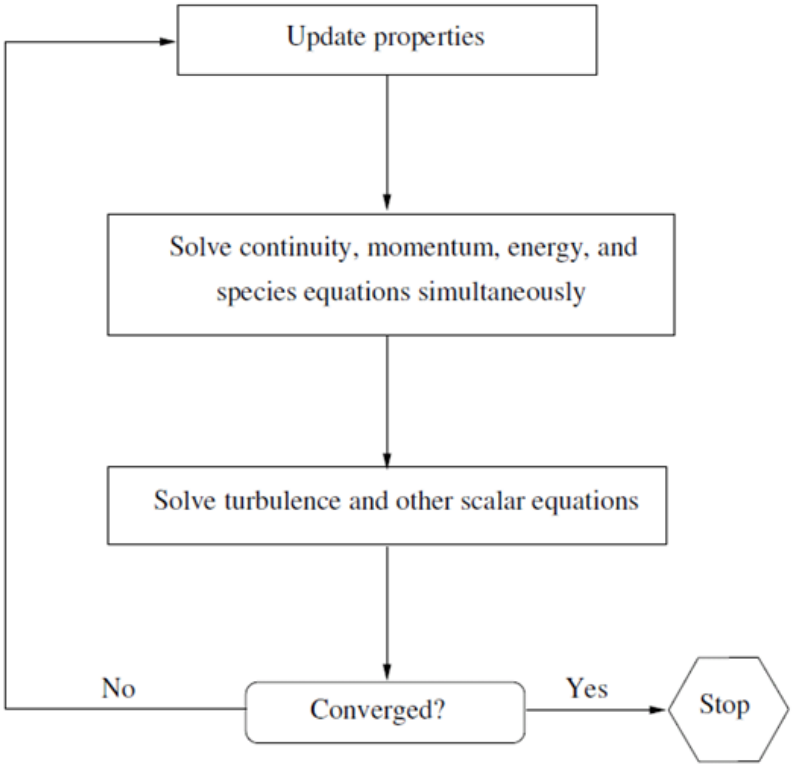

Figure 4.1: Overview of the density-based solution method.

1. Update the fluid properties based on the current solution; if the calculation has just started, the fluid properties will be updated based on the initialized solution.

2. Solve the continuity, momentum, and (where appropriate) energy equations simultaneously.

3. Where appropriate, solve equations for scalars such as for the turbulence properties using the previously updated values of the other variables.

4. Check for convergence of the equation set.

These steps are continued until the convergence criteria are met.

In the density-based solution method one can solve the coupled system of equations (continuity, momentum, energy) by using either the coupled-explicit formulation or the coupled-implicit formulation. The main distinction between the density-based explicit and implicit formulations is described below. In the density-based solution methods the discrete, non-linear governing equations are linearized to produce a system of equations for the dependent variables in every computational cell. The resulting linear system is then solved to yield an updated flow-field solution.

4.1.2. PRESSURE-BASED SOLVER

The pressure-based solver applies an algorithm which belongs to a general class of methods called the projection methods. In a projection method, the mass conservation (continuity) is achieved by solving a pressure (or pressure correction) equation. The pressure equation is derived from the continuity and the momentum equations in such a way that the velocity field, corrected by the pressure, satisfies the continuity. Since the governing equations are nonlinear and coupled, the solution process involves iterations wherein the entire set of governing equations is solved repeatedly until the solution has converged. Two pressure-based solver algorithms are available in Fluent: a segregated algorithm and a coupled algorithm.

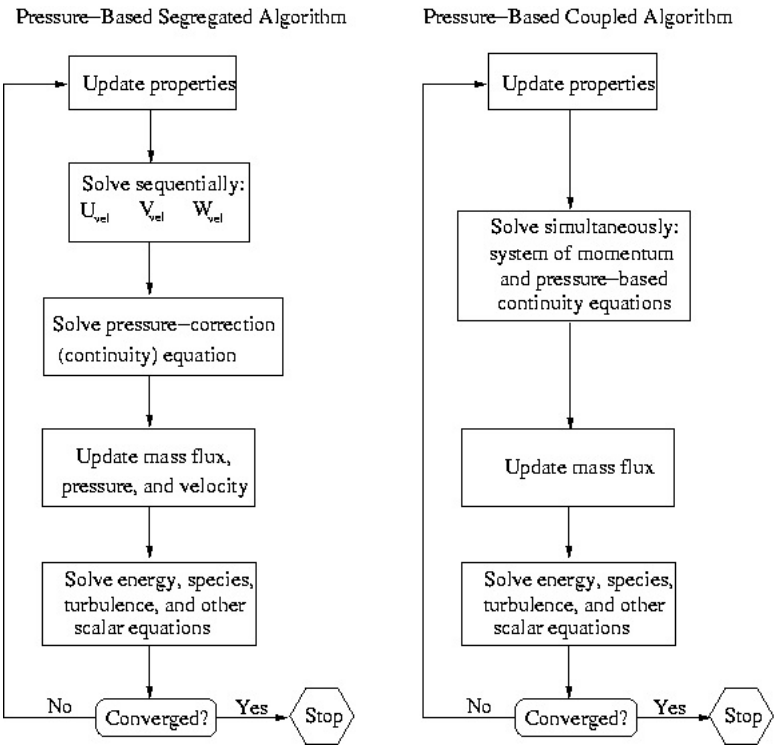

Figure 4.2: Overview of the pressure-based solution method.

With the segregated algorithm, each iteration consists of the steps illustrated in Figure 4.2 and outlined below:

1. Update fluid properties (such as density, viscosity, specific heat capacity, and also including the turbulent viscosity), based on the current solution.

2. Solve the momentum equations, one after another, using the recently updated values of the pressure and face mass fluxes.

3. Solve the pressure correction equation using the recently obtained velocity field and the mass fluxes.

4. Correct the face mass fluxes, pressure, and the velocity field using the pressure correction obtained from Step 3.

5. Solve the equations for additional scalars, if any, such as the turbulent quantities and temperature, using the current values of the solution variables.

6. Check for the convergence of the equations.

Two pressure-based solver algorithms are available in ANSYS Fluent: a segregated algorithm and a coupled algorithm.

Unlike the segregated algorithm described above, the pressure-based coupled algorithm solves a coupled system of equations comprising the momentum equations and the pressure-based continuity equation. Thus, in the coupled algorithm, steps 2 and 3 in the segregated solution algorithm are replaced by a single step in which the coupled system of equations is solved. The remaining equations are solved in a decoupled way as is done in the segregated algorithm.

4.2. TURBULENT MODELLING IN CFD

A brief introduction on different commonly used turbulence models is given below.

4.2.1. STANDARD $k-\epsilon$ MODEL

The $k-\epsilon$ turbulence model is a two-equation model in which the transport equations are solved for the turbulent kinetic energy k and the dissipation rate ϵ.

The equation for the turbulent kinetic energy k is:

$$\frac{\partial(\rho k)}{\partial t}+\frac{\partial(\rho k u_i)}{\partial x_i}=\frac{\partial}{\partial x_j}[\frac{\mu_t}{\sigma_k}\frac{\partial k}{\partial x_j}]+2\mu_t E_{ij}E_{ij}-\rho\epsilon \tag{4.2}$$

The equation for the the dissipation rate ϵ is:

$$\frac{\partial(\rho\epsilon)}{\partial t}+\frac{\partial(\rho\epsilon u_i)}{\partial x_i}=\frac{\partial}{\partial x_j}[\frac{\mu_t}{\sigma_k\epsilon}\frac{\partial\epsilon}{\partial x_j}]+C_{1\epsilon}\frac{\epsilon}{k}2\mu_t E_{ij}E_{ij}-C_{2\epsilon}\rho\frac{\epsilon^2}{k} \tag{4.3}$$

These two equations contain the following contributions: rate of change of k or ϵ + Transport of k or ϵ by convection = Transport of k or ϵ by diffusion + Rate of production of k or ϵ - Rate of destruction of k or ϵ.

In these equations μ_t represents the eddy viscosity:

$$\mu_t=\rho C_\mu\frac{k^2}{\epsilon} \tag{4.4}$$

The equations contain some constants: σ_k, σ_k , σ_ϵ σ_ϵ , $C_{1\epsilon}$, $C_{1\epsilon}$ and $C_{2\epsilon}$, $C_{2\epsilon}$.
The $k-\epsilon$ model uses the gradient diffusion hypothesis to relate the Reynolds stresses to the mean velocity gradients and the turbulent viscosity.

The performance of the $k-\epsilon$ model can be summarized as follows. It is the most robust, widely used two-equation turbulence model when solving the Reynolds-Averaged Navier-Stokes equations (RANS), despite the known limitations of the model. The model is very easy to implement and it is computationally cheap. The $k-\epsilon$ model, however, performs poorly for complex flows involving large pressure gradients, separation, or strong streamline curvature. All these effects are present in the highly under-expanded jet flow. Another shortcoming is the numerical stiffness when the equations are integrated through the viscous sublayer which is treated with damping functions that can cause numerical stability issues. But the most disturbing weakness is lack of sensitivity to adverse pressure gradients, which is assumed to be present near the wall of the configuration considered in this study.

4.2.2. STANDARD $k-\omega$ MODEL

Another two-equation turbulence model is $k-\omega$ model. This model solves (again) the kinetic energy k, but also the specific and turbulent dissipation rate ω. The equation for the kinetic energy reads:

$$\frac{\partial(\rho k)}{\partial t}+\frac{\partial(\rho k u_i)}{\partial x_j}=\rho P-\beta^*\rho\omega k+\frac{\partial}{\partial x_j}[(\mu+\sigma_k\frac{\rho k}{\omega})\frac{\partial k}{\partial x_j}] \tag{4.5}$$

with $P=\tau_{ij}\frac{\partial u_i}{\partial x_j}$. The equation for the specific dissipation rate ω reads:

$$\frac{\partial(\rho\omega)}{\partial t}+\frac{\partial(\rho\omega u_i)}{\partial x_j}=\frac{\gamma\omega}{k}P-\beta\rho\omega^2+\frac{\partial}{\partial x_j}[(\mu+\sigma_\omega\frac{\rho k}{\omega})\frac{\partial k}{\partial x_j}]+\frac{\rho\sigma_d}{\omega}\frac{\partial k}{\partial x_j}\frac{\partial\omega}{\partial x_j} \tag{4.6}$$

The performance of the $k-\omega$ model can be summarized as follows. This model can easily be extended with low-Reynolds number terms to describe the turbulent boundary layer very close to a wall. These terms also have the potential to predict the transition between laminar and turbulent flows. Compared to the $k-\epsilon$ model, the $k-\omega$ model performs significantly better under adverse pressure gradient conditions. The model also has good numerical stability properties.

4.2.3. SST $k-\omega$ MODEL

The Shear Stress Transport (SST) model is a variant of the standard k-ω model. It combines the standard $k-\omega$ model for use near walls and the standard $k-\epsilon$ model away from the wall using a blending function.

The SST $k-\omega$ model offers similar benefits as the standard $k-\omega$ model. The SST model accounts for the transport of turbulent shear stress and gives quite accurate predictions of the onset and the amount of flow separation under adverse pressure gradients. SST is recommended for high accuracy boundary layer simulations. The dependency of the model on the wall distance makes this model less suitable for free shear flows compared to standard $k-\omega$.

4.3. WALL DISTANCE y^+

The wall distance y^+ is an important parameter in turbulence modeling in CFD. This is because it is important to know how the flow behaves near the wall, to consider the effects near to a wall. This also determines how the grid should be refined when approaching the wall. The wall distance y^+ is a non-dimensional number similar to the local Reynolds number. It determines the region in the wall boundary layer: the viscous sublayer very close to the wall (typically below $y^+ = 5$, the log layer between the viscous sublayer and a location with about $y^+ = 300$, and the free stream core layer for larger y^+ values.

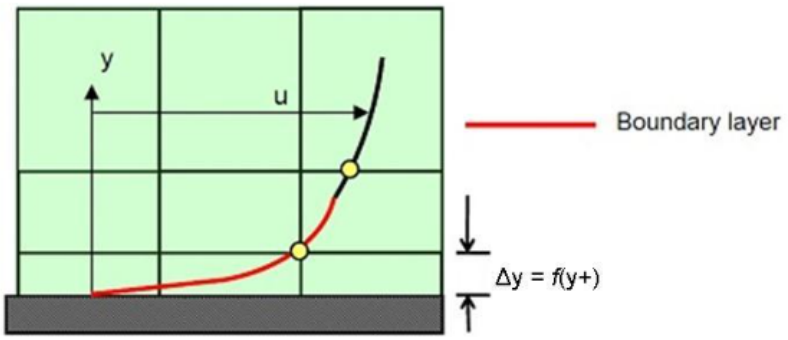

Figure 4.3: Illustration of y^+ framed in a numerical grid

Referring to figure 4.3 we need to be careful to ensure that the grid distribution is not so coarse that the first node falls outside the viscous sublayer if a low-Reynolds number model is used, or outside the log layer if a wall function is used. If the grid is too coarse, the turbulence model may incorrectly calculate the flow properties at this first calculation point which will introduce errors in the results for the wall shear stress and for the pressure drop.

The definition of y^+ at the first grid cell away from the wall is:

$$y^+ = \frac{\rho U_\tau \delta y}{\mu} \tag{4.7}$$

where U_τ is shear velocity defined as $U_\tau = \sqrt{\tau_w/\rho}$ and $\tau_w = C_f \frac{1}{2} \rho U^2_{Freestream}$. Figure 4.4 shows how the boundary layer can split-up in various regions, which are also listed below:

- $y^+ < 5$: Viscous sublayer region (velocity profile is assumed to be laminar-like and the viscous stress dominates the wall shear stress)

- $5 < y^+ < 30$: Buffer region (both viscous and turbulent shear dominate)
- $30 < y^+ < 300$: Fully turbulent log-law region (corresponds to the region where turbulent shear dominates)

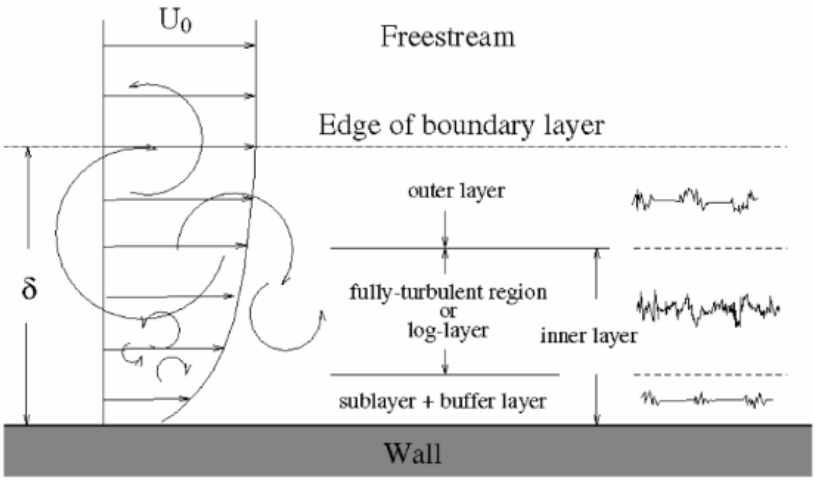

Figure 4.4: Various in turbulent wall boundary layer

As explained, y^+ is the near wall grid coordinate that has been non-dimensionalised using the so-called shear stress velocity. It is effectively a local Reynolds number. In order to resolve the viscous sublayer one needs to have a first grid cell with a y^+ value of less than 5. Normally it has been found that an average value along the surface of $y^+ = 1$ is adequate. But the best approach is to run two simulation with a different y^+ choice, one for a coarse grid and one for a refined grid. If the solution on the refined grid does not change significantly, then the coarse grid is adequate.

4.4. INITIALIZATION

For many complex flow problems such as those found in rotating machinery, or flows in expanding or spiral ducts, the convergence of the numerical solution can be accelerated if a better initial solution is used at the start of the calculation. The Full Multigrid initialization (FMG initialization) can provide this initial and approximate solution at a minimum cost to the overall computational effort.

This initialization procedure is computationally inexpensive; even for large problems, a good initial solution can be obtained in a fraction of the time spent to converge to a final solution. When the FMG initialization is started, the algorithm will perform the following steps:

1. Recording of the current solver selection and of all current solver parameters.
2. Switching from the selected solver to the density-based explicit formulation.
3. Performing one FMG iteration using the FMG parameters given in the text command interface (see below).
4. Switching back to the initially selected solver and resetting all solver parameters back to the original solver values.

In the FMG iteration, the inviscid Euler equations are solved using a first order-discretization to obtain the approximate solution. However, the turbulence equations or the equation for any other transport scalar are not solved in the FMG initialization.

5

SIMULATION SET-UP AND SIMULATION RESULTS

As mentioned before the benchmark for this study is the experiment carried out at Imperial College in London for Shell, but to this date the results from imperial college haven't been analyzed. So they aren't taken into this report. The same geometry is used in this study and the setup is explained in this chapter. In addition some simplifications are made to translate the 3D model to a much simpler 2D model.

5.1. GEOMETRY

The configuration used in the simulation model is matched to the one used in the lab experiments at Imperial College. The fluid domain along the orientation of the three coordinate system is shown in figure 5.1. The bulk flow occurs along the $+X$-direction. As shown figure 5.1 it includes (1) an upstream section that feeds the nozzle, (2) the nozzle tube, and (3) the downstream "test section". The upstream section has a 25 mm × 25 mm square size with a length of 25 mm. The cylindrical nozzle tube has a diameter of 1.55 mm, and a length of 5 mm. The test section has a 50 mm × 50 mm square cross section that extends over a length of 500 mm.

The sizes of the geometry are also summarized in table 5.1.

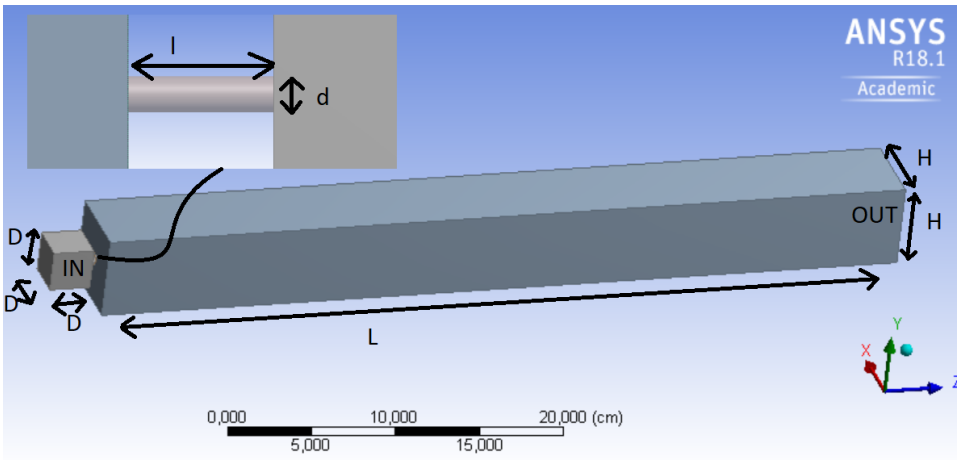

Figure 5.1: Flow domain and geometry used for the CFD as matched with the experimental set-up.

5.2. MESHING

When creating a mesh there are some aspects that need to be considered since the simulation results will be largely dependent on the quality of the grid. Both the numerical stability and accuracy could be affected by a

Table 5.1: Sizes in the geometry.

Symbol	Quantity	Size [mm]
D	Inlet height, width and length	25
d	Nozzle diameter	1.55
l	Nozzle length	5
L	Outlet length	500
H	Outlet height or width	50

poor quality of the grid. Obviously, for the best accuracy the grid resolution should be as high as possible, but a higher resolution requires more computing resources and generates longer turnaround times.

Primarily there should be no gaps in the grid or overlap of elements. Furthermore the grid points should be clustered around areas of interest such as regions of large gradient, for example: boundary layers, separation points, shocks, around sharp corners or curves.

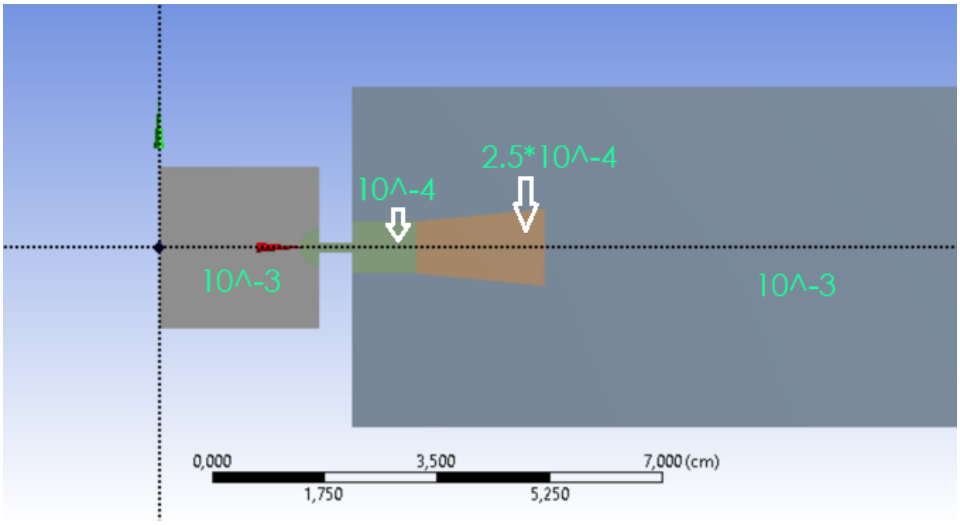

Figure 5.2: Computational domain with areas where mesh refinement is applied.

Two types of meshing methodologies are used and compared against each other in this study: the quad mesher and the triangle mesher, in which the former is the favorite one. The reason for the choice of the quad mesh is the fact that this mesh is more aligned with the flow. In figure 5.2 the regions with mesh refinement are depicted. A reference length size of 1 mm is used with local refinement near the nozzle region (up to 10 times finer, indicated in orange) to improve the resolution in the region where the flow expands creating a shock and discontinuities. There is a total of approximately 8.4 million cells. After the nozzle region, a uniform prism layer is generated at the walls to capture the boundary layer flow. 12 layers of prismatic cells extending to the reference length size with a growth factor of 2.5 are used. Figure 5.3 shows that the area after the throat is refined to make sure that the shock diamonds are capture properly. After this refined area there is another less denser downstream area to capture the (high) velocities after the shock diamond (refinement of $2.5 \cdot 10^{-4}$) orange area in figure 5.2.

5.3. INITIAL CONDITIONS

In the experiments, the inlet to the test section is fed from a temperature regulated stagnation reservoir. The measured values of the static pressure and temperature at the inlet are 120 bara and -17 °C, respectively. It should be noted that the stagnation quantities are different from the static quantities. But at such low inlet and outlet velocities, the static quantities are considered to be similar to the stagnation quantities.

The outlet of the test section on the far downstream end is modeled with a pressure boundary condition,

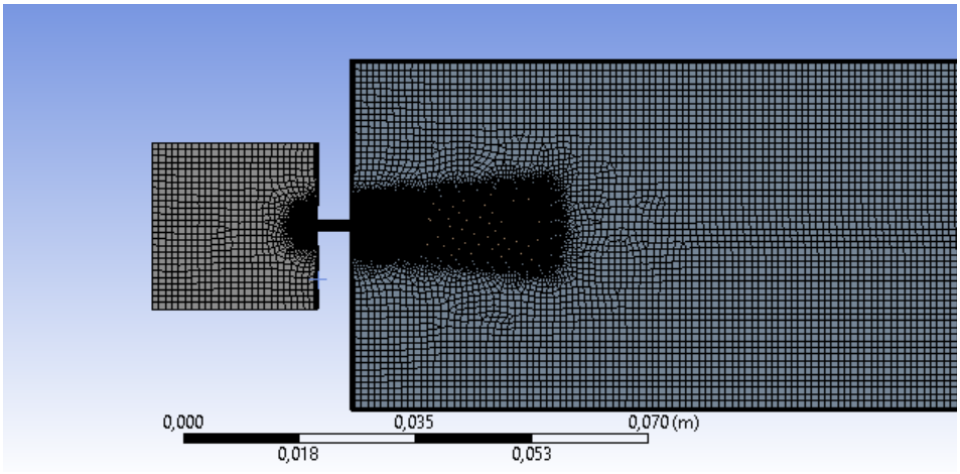

Figure 5.3: Area with mesh refinement.

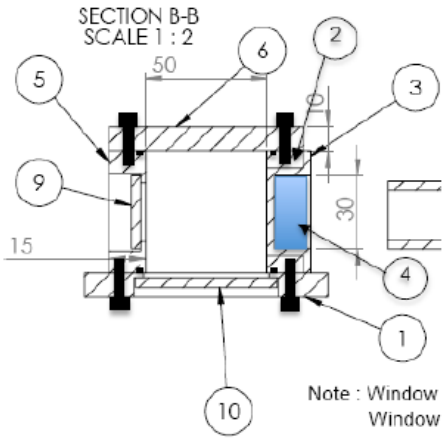

1	Wall A	Al
2	Wall B	Al
3	Insert	PMMA
4	Insulator	Polyur.
5	Wall C	Al
6	Wall D	Al
9	Window (30x300)	Fused silica
10	Window (60x300)	Fused silica

Figure 5.4: Wall materials and thickness specifications as used in the experimental set-up.

which is set to 1 bara. The walls of upstream feed section and of the nozzle are modeled as adiabatic walls, which thus prevent any heat loss/gain through the walls. The walls of the test section are firstly modeled as adiabatic walls to have a reference. Later on the walls were allowed to transport heat (i.e. non-adiabatic walls were applied).

The location and material type of the walls as used in the experimental set-up are shown in Figure 5.4. These thermal properties were also used in the simulations with the non-adiabatic walls. In these simulations, the heat conduction along the plane of the wall is assumed to be negligible. A "shell" region approach can be used in the CFD simulations to model the heat flux normal though the walls. This approach assumes that the heat conduction is only one-dimensional. The model requires the wall thickness and wall material as input. Furthermore, the walls of the test section are modeled to be uniform with no changes in material properties. The thickness and material type of the walls (present in the experimental set-up and as used in the simulations) are shown in figure 5.5 and in table 5.2. The wall that connects the downstream end of the orifice to the side walls of the outlet section is modelled as fully adiabatic.

The thermal conditions at the outer side of the wall should be specified as well. Next to conductivity through the wall the convective heat transfer should be taken into account. The ambient temperature (i.e. the room temperature) is 20 °C and the heat transfer coefficient between the outer side and the wall to the ambient air is set to 20 W/(m^{2}K), a proven convective heat transfer for ΔT around 60-80 ^{o}C.

Table 5.2: Thickness and thermal conductivity of the walls.

Wall	Thickness [mm]	Thermal conductivity [W/(m-K)]
Aluminum	10	202.3
Fused-Silica	5	1.38
Polyurethane	18	0.002

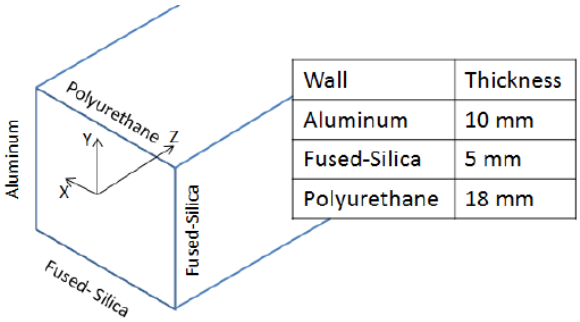

Figure 5.5: Test section wall material and thickness used in the CFD simulations.

5.3.1. GAS PROPERTIES

To ensure the occurrence of the Joule-Thomson cooling in the test section a proper fluid has to be chosen. As was already described in section 2.8 argon is a suitable gas for use in the experiments, and it was thus also used in the simulations of the JT-cooling. The thermodynamic properties of argon are modeled as a temperature dependent polynomial, for which the weak pressure dependence of the properties is neglected. The details are given in Appendix A.

The phase diagram of argon is shown in figure 5.6. According to this phase diagram, a phase change of argon (from gas to liquid) could occur in the flow system. At a pressure of 1 bara, argon gas will condense to liquid at a temperature of 88 K. In such a case when the temperatures of the flow drops below 88 K due to JT-cooling, the formation of argon liquid droplets will occur. However, the phase change models available in ANSYS Fluent are not compatible with the real gas model which is needed to capture the JT-effect. Furthermore, the numerical stability of the phase change model within the coupled flow solver in a multiphase flow regime is also highly doubtful. Due to these limitations, the formation of liquid droplets is neglected in the present study.

5.3.2. TURBULENCE MODEL

The effect of turbulence modeling on thermal behaviour with the JT cooling is one of the areas of interest in the present study. Different turbulence models were explained in the chapter 4. To obtain the best accuracy, we have selected the $k-\omega$ model coupled with the SST (Shear Transport) correction. This approach uses the $k-\omega$ type of modeling in the region close to a wall and switches to a $k-\epsilon$ type of treatment for the bulk flow. The SST $k-\omega$ model is used together with the density-based solver.

5.3.3. EQUATION OF STATE

Different equations of state for argon gas were used to model the pressure density coupling in the compressible flow system. In section 2.8 is was noted that the ideal-gas model equation of state will not predict JT-cooling, which is a real-gas effect. In the CFD calculations carried out by Shell with the Star-CCM+ CFD tool the Peng-Robinson model is used as the Equation of State for real-gas argon. Other Equations-of-State were also considered, but these and gave similar results as the Peng-Robinson model.

5.3.4. VISCOUS EFFECTS

To evaluate the effect of wall friction on the cooling when the fluid was passing through the nozzle, the flow was described by using the steady-state Reynolds-Averaged Navier-stokes (RANS) equations with the Boussinesq hypothesis for the closure the Reynolds stresses. The additional settings of compressible flow and vis-

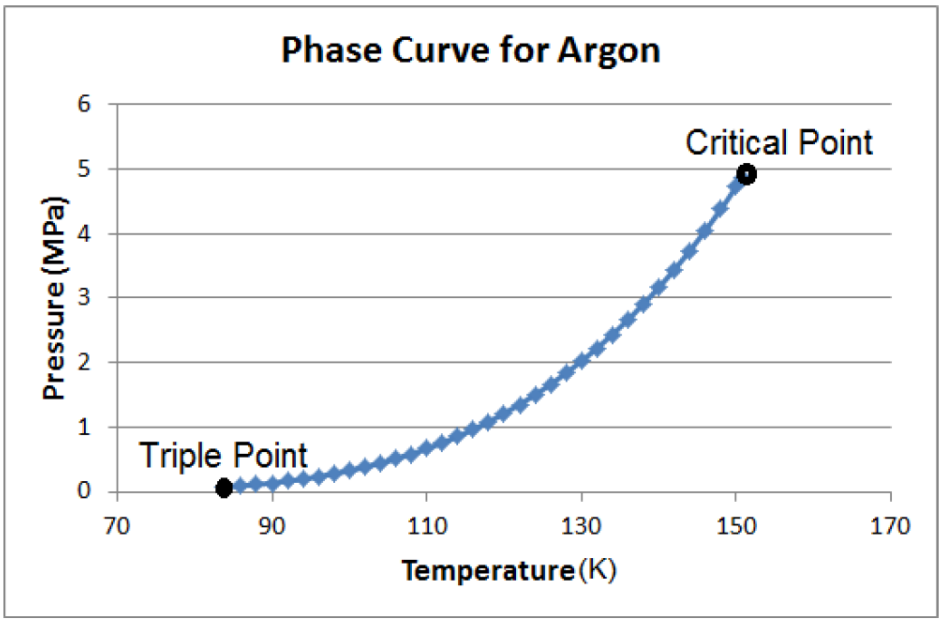

Figure 5.6: Thermodynamic phase boundary of argon indicating the triple point and the critical point. At a pressure of 1 bara, argon gas will condense to liquid at a temperature of 88 K.

cous heating were enabled to obtain faster computational times.

To make sure that the mesh resolution was fine enough, the dimensionless wall distance (y^+) is considered (see section 4.2); the first grid cell along the wall should be in the viscous sublayer and it should thus have a y^+ value smaller than 5.

It was also found to be necessary to increase the length of the computational domain to prevent backflow at the outlet. Due to the flow separation downstream of the shock there is backflow in that region. To prevent fluid intake from the outlet (carrying the ambient temperature), the longer domain is used. In this way the full region with backflow and recirculation remains within the computational domain.

The equations were solved using the Fluent density-based implicit solver with the Roe-FDS flux type. In order to accelerate the convergence of the solution, the FMG-initialization is applied, see section 4.4. A proper convergence of the solution downstream of the shock could not be achieved with the pressure-based coupled solver. Furthermore, to obtain convergence, it was necessary to discretize the equation with only the first-order upwind scheme rather than the second-order upwind scheme. Simulations were done, as mentioned earlier, with argon gas both as an ideal gas and as real gas where the walls are considered to be adiabatic.

5.4. THREE-DIMENSIONAL, ADIABATIC SIMULATIONS

The most important settings are summarized as:

- Solver type: density-based solver
- Steady state formulation
- Model: SST $k-\omega$ (2 eqn) with low-Reynolds number corrections, viscous heating and compressibility effects
- Fluid: argon with properties described with ideal gas or with Peng-Robinson equation of state
- Formulation: implicit

Table 5.3: Inlet conditions.

Property	Value and unit
Stagnation pressure	120 bara
Stagnation temperature	256 K
Gas specific heat ratio	1.667
Gas constant	207.9 J/kg/K

- Flux type: Roe-FDS
- Gradient spatial discretization: least squared cell based
- Flow: Second order upwind
- Turbulent kinetric energy: Second order upwind
- Courant number: 0.1
- Under-relaxations factors: all set to 0.1
- Limit for positivity rate limit: 0.02

As mentioned in section 2.2, the mass flow rate across a choked nozzle is only dependent on the stagnation temperature and pressure, which reads (assuming a particular ideal gas):

$$m^*_{nozzle} = m^*_c = A_c \sqrt{\frac{\gamma}{R_g}} \frac{P_0}{\sqrt{T_0}} \left(\frac{2}{\gamma+1}\right)^{\frac{\gamma+1}{2(\gamma-1)}} \tag{5.1}$$

For the flow conditions in the present study (as summarized Table 5.3) the mass flow rate through the nozzle is calculated to be 0.0721 kg/s.

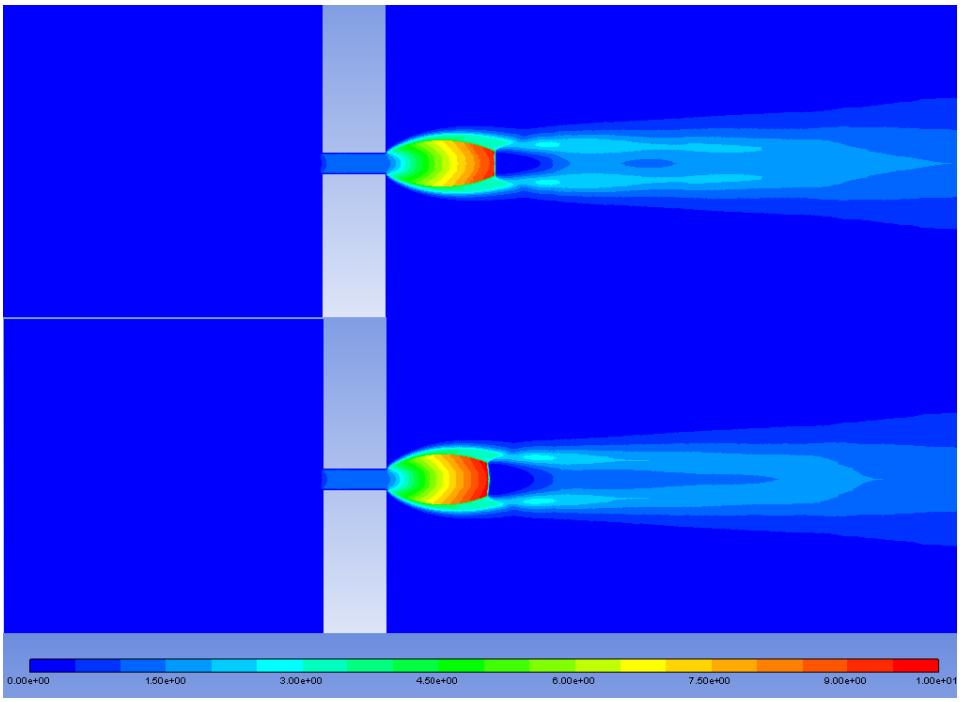

Figure 5.7: Contour plot of the Mach number for both ideal (above) and real gas (below).

The flow rates obtained in the CFD simulations for the ideal and real gas cases are 0.0708 kg/s and 0.0686 kg/s, respectively which is close to the mentioned theoretical value of 0.0721 kg/s. The reason why this CFD calculations have a lower mass rate flows due to the viscous boundary layer in the orifice, where tt contracts

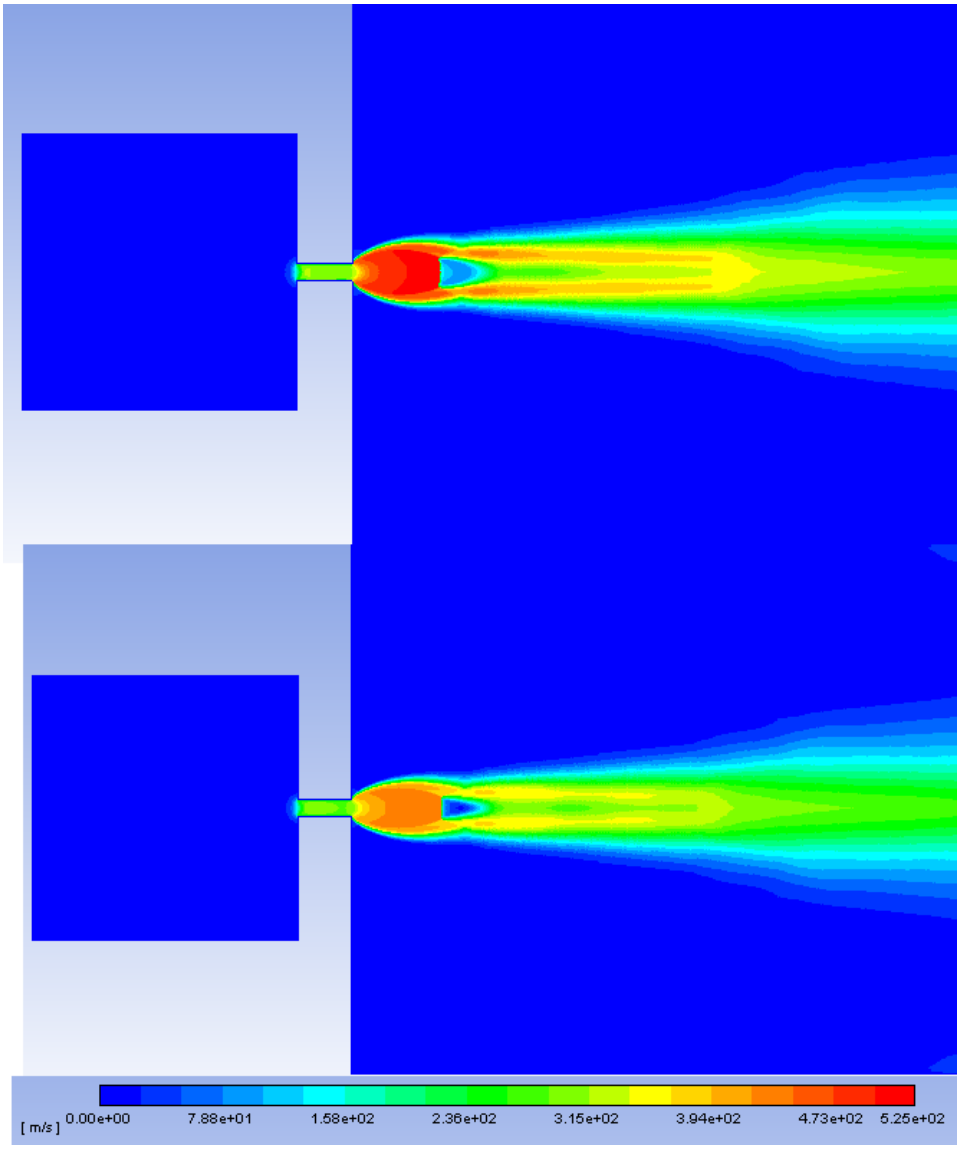

Figure 5.8: Contour plot of the velocity for both ideal (above) and real gas (below).

the area of the nozzle. The resulting Mach contour plots are shown in figure 5.7 and the velocity plots are shown in figure 5.8. Furthermore the contours for the static temperature are shown in figure 5.9.

Flow separation occurs at the boundary of the shock diamond. The shock front has a shape that is similar to what is described in the literature. The gradients of the shock are largest at the centreline; this is also clear from the change in the velocity and in the Mach number along the centre line, as is shown in figures 5.10 and 5.11, respectively. For reference, x = 0 corresponds to the location where the choke expands from the minimal cross-sectional area to the outlet area.

The shock occurs at almost the same distance for both the real gas and the ideal gas. The shock characteristics were described in chapter 2. In table 5.4 the CFD predictions for the location of the Mach disk are given; the values for the real gas case and for the ideal gas case are very close to the value in the empirical relation of Love et al. [10].

As shown in figure 5.13, for a given initial pressure and temperature, the predicted initial density with the two different EOS models differs by about 15%.

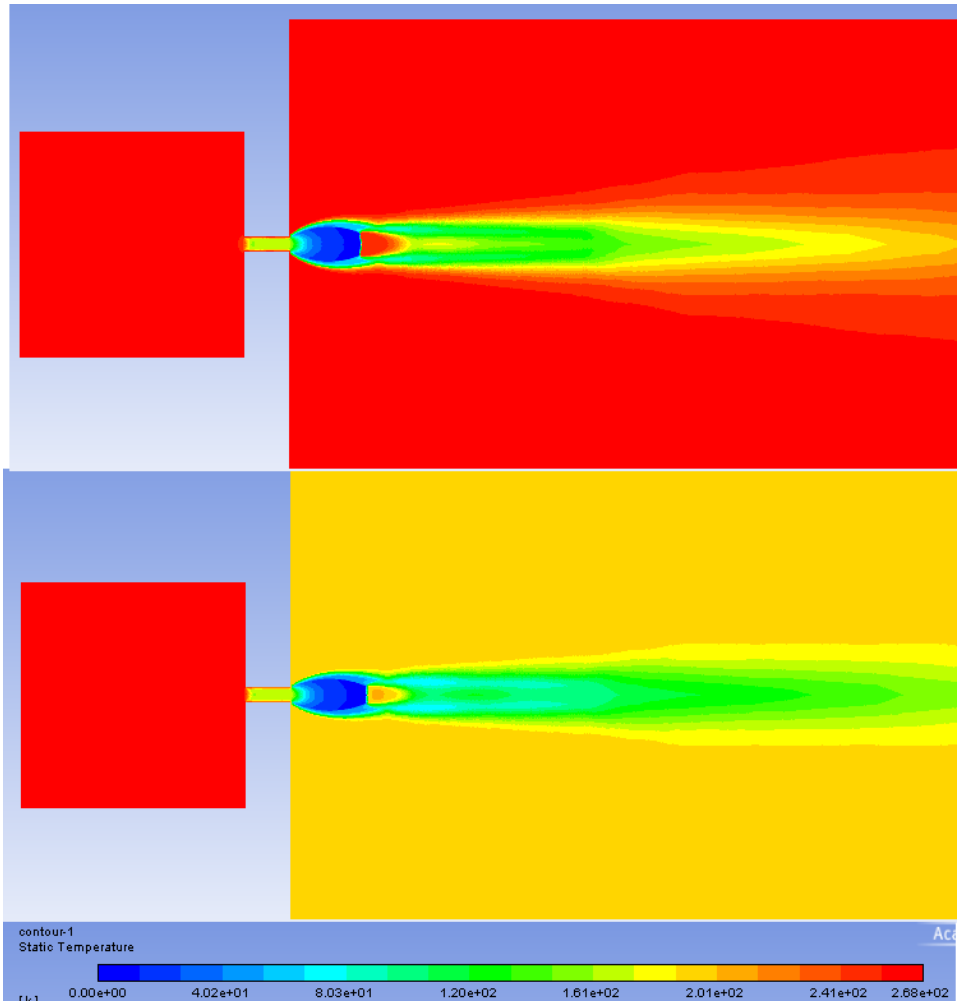

Figure 5.9: Contour plot of the static temperature for both ideal (above) and real gas (below).

The contours of the static temperature for the real gas and for the ideal gas are compared in figure 5.9. The minimum temperature is quite low, as can also be seen in table 5.5. At these low temperatures a phase change will occur which is not incorporated in the Fluent model.

The temperature profile along the centreline is depicted in figure 5.12. The outlet temperature for a real gas (196 K) is about 60 °C lower than for an ideal gas (256 K). A thermodynamic tool can be used to predict the Joule-Thomson cooling. Those predictions are obtained with the Shell Flashmate tool or with Refprop. The assumption was made that the inlet and outlet velocities are negligible in the isenthalpic equation ($H_1 + u_1^2/2 = H_2 + u_2^2/2$ -> $H_1 = H_2$). The isenthalpic flash predicts that the temperature will decrease to 196 K, which is the same as the CFD result for the outlet temperature for the real gas case. The total temperature and pressure, as shown in Figure 5.15, remain constant at the inlet section up to the nozzle (< 0 m), after which is drops steeply across the shock; note that the shock is a non-isentropic compression wave that causes a decrease in the total pressure).

Table 5.4: Shock distance characteristic

Approach	Shock distance (mm)
Real gas CFD	88.2
Ideal gas CFD	85.3
Relation (Love et al.)	86.5

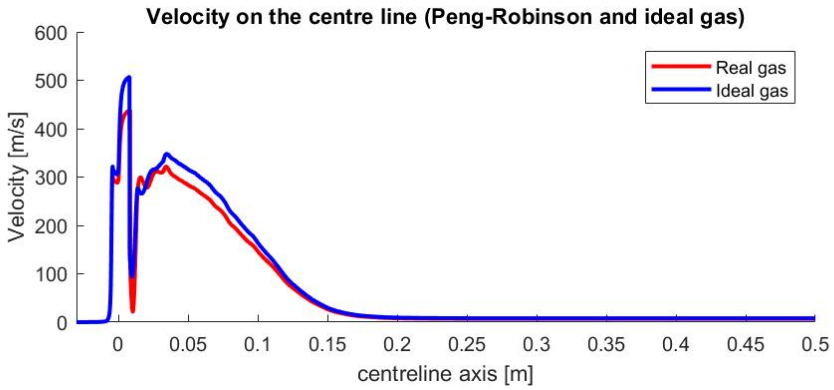

Figure 5.10: Predicted flow velocity along the centreline of the domain.

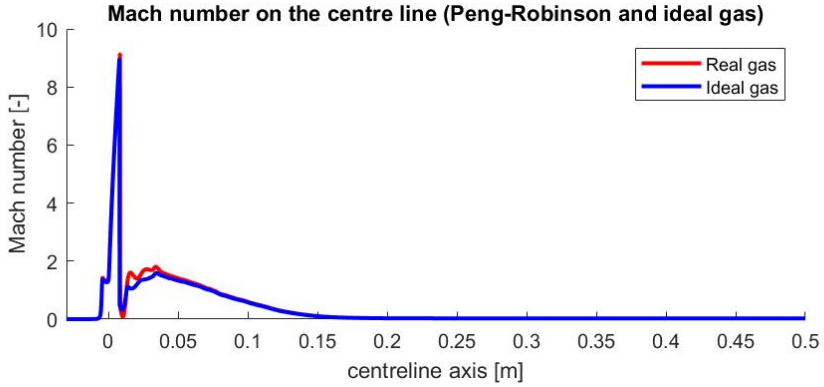

Figure 5.11: Predicted Mach number along the centreline of the domain.

5.5. THREE-DIMENSIONAL, NON-ADIABATIC SIMULATIONS

Three-dimensional CFD simulations with non-adiabatic walls were carried out. Figure 5.16 compares the static temperature at the centreline, as obtained for both adiabatic and non-adiabatic walls. As expected, the temperature at the outlet is slightly higher with non-adiabatic walls than with adiabatic walls, due to the heat flow from the warmer ambient to the colder jet fluid in case of non-adiabatic walls.

The wall temperatures are compared at the four walls enclosing the test section. Figure 5.17 shows the temperature distribution on the aluminum wall. Due to the high conductivity in aluminum, the wall is seen to be at a higher temperature since heat can quickly flow from the warmer surrounding into the colder test section. Both the walls show a similar temperature distribution. This is, however, not the case with the poly-urethane and fused-silica walls. Especially for the poly-urethane (which has a thermal conductivity of 0.03 W/m/K), figure 5.18 shows that this wall has the tendency to behave more like an adiabatic wall. For the fused-silica case, as shown in figure 5.19 and in figure 5.20, there is more heat exchange through the wall. The legend of all the contour plots is given in figure 5.21.

Next to these contour plots, which are less suitable to see the actual quantitative temperature values, figure 5.23 shows the temperature at the midline of the wall along the section. Furthermore, figure 5.24 shows the heat transfer through the walls. The cause of the first little bump in the temperature plot can be found by considering the contours of the angle of the velocity vectors in figure 5.22; angles between -90 and 90 deg denote positive flow and the other angles denote flow reversal. This shows that the jet touches the side walls

Table 5.5: Comparison of minimum static temperature (ideal gas and real gas).

Quantity	Ideal gas	Real gas
Minimum static temperature (K)	8.85	7.63

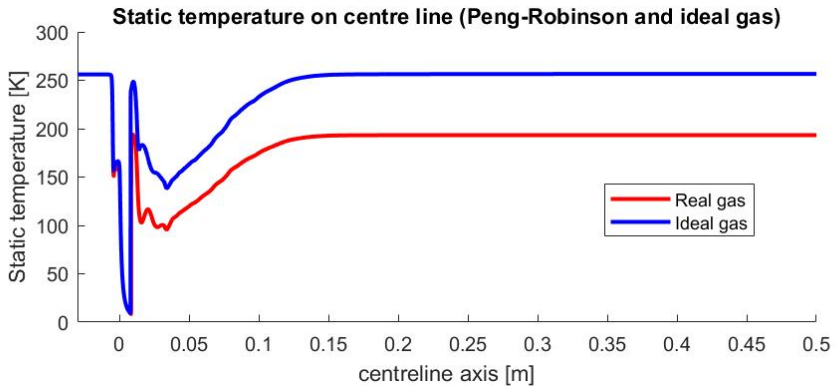

Figure 5.12: Predicted static temperature along the centreline of the domain.

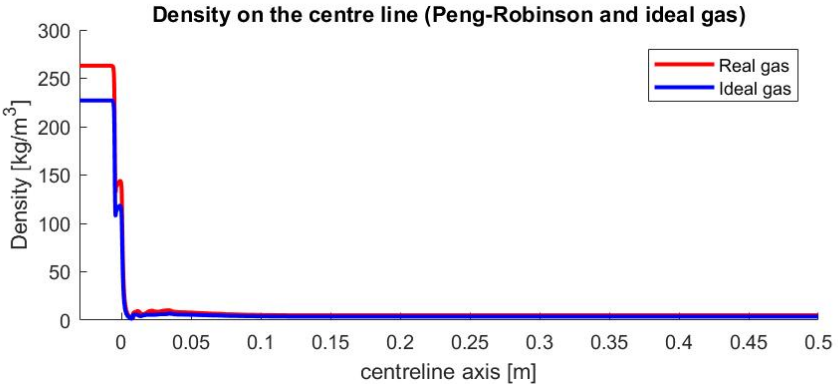

Figure 5.13: Predicted density along the centreline of the domain.

at a distance of about 0.1 m. To have a clear overview of the whole domain (with non-adiabatic walls) the contours of the Mach number and of the temperature are shown in figure 5.27 and in figure 5.28, respectively.

5.5.1. MESH DEPENDENCE

To ensure that a proper mesh is used for the modeling of the structure of the shock wave, a mesh dependence study is performed. In order to do this, various meshes have been constructed with a different number of cells. Each mesh is used in a simulation with the same discretization scheme, turbulence model, and solution method.

One of the parameters monitored in the mesh dependence study is the minimum static temperature in the domain. Another parameter that is considered is the maximum Mach number, which occurs just upstream of the shock. The results for the temperature and Mach number are shown in figure 5.25 and in figure 5.26, respectively. It can be concluded that almost mesh-independent results are obtained when using about 8 million grid cells or more.

5.5.2. COMPARISON OF FLUENT AND STAR-CCM+ RESULTS

As mentioned before, Shell has carried out similar CFD simulations, using Star-CCM+ instead of Fluent; see [17]. The results described in that report are compared with the results obtained in the present studies. Two main differences in the results obtained in the two simulation studies are found:

1. First, the temperature on the poly-urethane wall differs a lot. This is most likely due to the wall conditions applied at the wall. The thermal conductivity used for the poly-urethane in the present study was 0.03 W/m/K. Due to this low conductivity, the wall will behave like a adiabatic wall. Here the temperature at the wall should be almost similar to the temperature of the flow, as only little heat is added from the outside to the jet. The wall temperatures a obtained with STAR-CCM+ in [17] are shown in

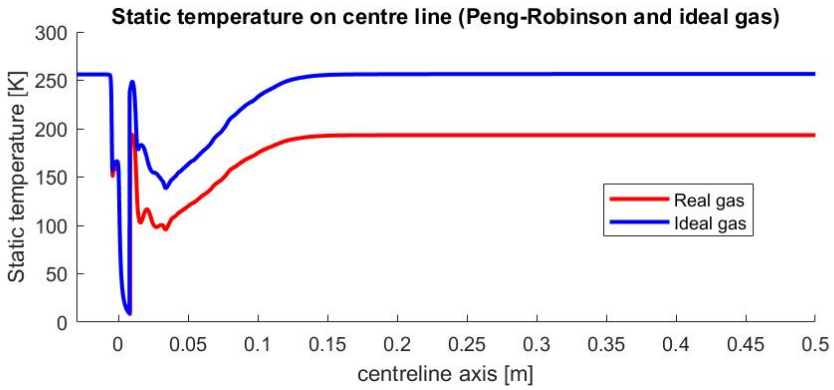

Figure 5.14: Predicted static pressure along the centreline of the domain.

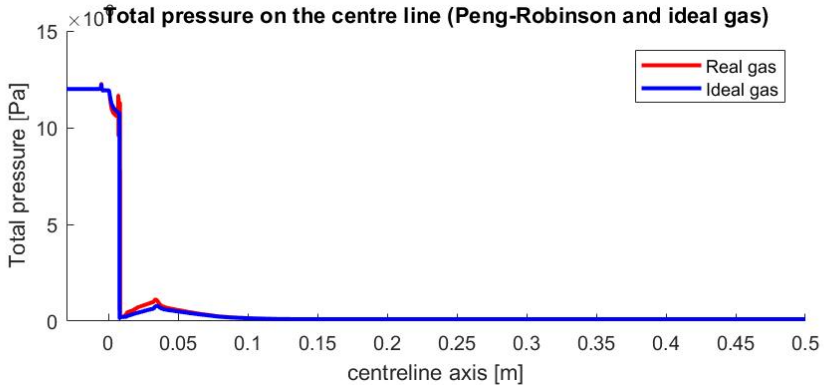

Figure 5.15: Predicted total pressure along the centreline of the domain.

Appendix C.

2. Second, the maximum Mach number between the calculations differs significantly. In the STAR-CCM+ results, the maximum Mach number is about 6, while the present results obtained with Fluent give a value of about 9. To further verify this, in the next section results are described that we have obtained by developing a MATLAB programme that calculates the inviscid, supersonic axisymmetric flow. Figure 5.29 compares the Mach numnber at the centre line as obtained with Fluent in the current study (maximum about 9) and with STAR-CCM+ obtained in [17] (maximum about 6).

5.6. SUPERSONIC AXISYMMETRIC FLOW IN MATLAB

In chapter 3, the theory for the inviscid gas dynamics of an under-expanded jet was described. The solution of the inviscid, compressible equations was programmed in MATLAB, and the results for iso-contours of the Mach number, which includes the shock, are depicted in figure 5.30. The corresponding MATLAB code is described in Appendix B.

The flow field that MATLAB has predicted is very similar to the Fluent results. As mentioned already, MATLAB solves the inviscid equations whereas Fluent solves the viscous equations, using a model for the turbulence. The predictions of the Mach number at the centreline as obtained with MATLAB and Fluent are compared in figure 5.31. The agreement is very good; both the location of the shock and the maximum Mach number have about the same value with the two methods. This shows that the shock behaviour is almost not affected by viscous effects and by turbulence.

A comparison can be made between the Mach number, the static temperature and the velocity along the centreline. The Mach number is coupled to the pressure through the function

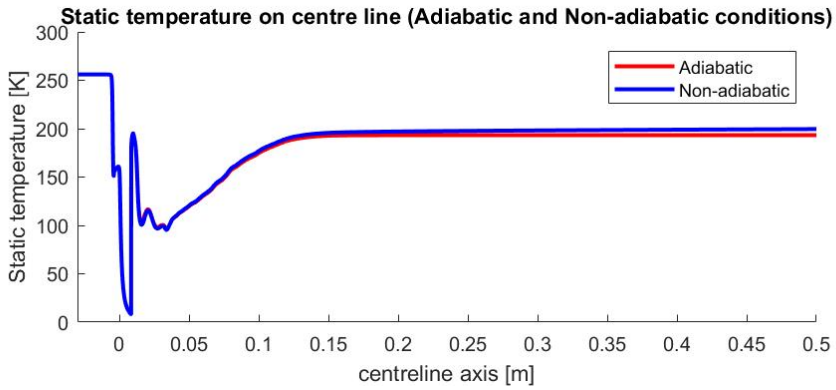

Figure 5.16: Predicted static temperature along the centreline for both adiabatic and non-adiabatic wall conditions.

Figure 5.17: Predicted temperature on the aluminum wall; Results obtained from CFD using PR EOS.

Figure 5.18: Predicted temperature on the poly-urethane wall. Results obtained from CFD using PR EOS.

Figure 5.19: Predicted temperature on the fused-Silica wall at the negative X end. Results obtained from CFD using PR EOS.

Figure 5.20: Predicted temperature on the fused-silica wall at the positive Y end. Results obtained from CFD using PR EOS.

Figure 5.21: Legends of figure 5.17,5.18,5.19 and 5.20.

$$P = P_0(1 + \frac{\gamma - 1}{2} M^2)^{\frac{-\gamma}{\gamma - 1}} \tag{5.2}$$

The pressure and the temperature are coupled through the isenthalpic flash (with inclusion of the kinetic energy contribution), as shown for argon in figure 5.32. As expected, the temperature decreases if the pressure is decreased. In this way the Mach number can be transformed to a temperature. The results for the temperature along the centreline are compared in figure 5.33.

Assuming that γ and R are constant in the domain, the velocity can be calculated from the following relation:

$$M = \frac{V}{a} = \frac{V}{\sqrt{\gamma RT}} \tag{5.3}$$

The resulting velocity along the centreline is shown in figure 5.34.

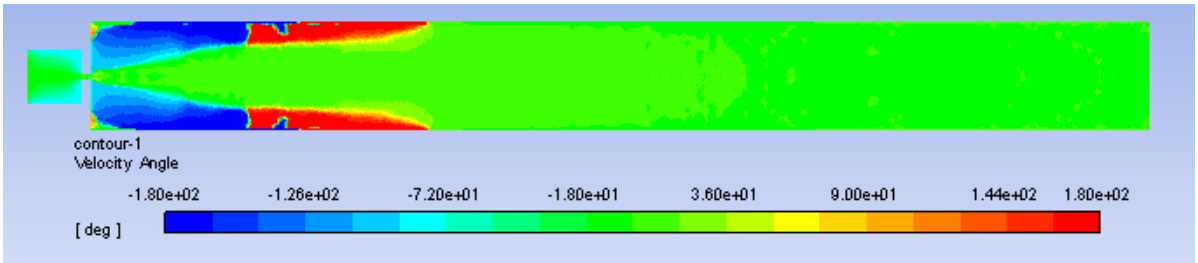

Figure 5.22: Contour plot of the velocity angle; blue and red denote flow reversal.

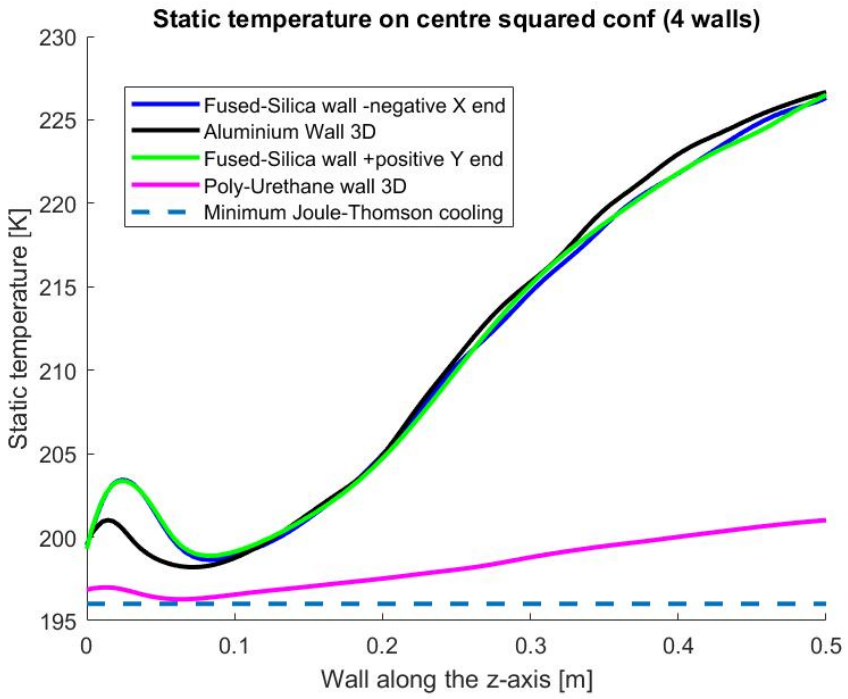

Figure 5.23: Static temperature on all four walls of the three-dimensional domain.

5.6.1. DEPENDENCE ON THE NUMBER OF CHARACTERISTICS

To obtain accurate results with the MATLAB code, a sufficient number of characteristics needs to be applied. The parameter used to verify the dependence on the number of characteristics is the location of the shock wave. The results of the analysis are shown in figure 5.35. It can be concluded that above a number of 500,000 characteristics the solution does hardly change anymore.

The very good agreement between the results obtained with the MATLAB code and with the Fluent code confirms that the Fluent results are reliable. In particular both methods find a maximum Mach number of about 9 just before the shock. This is in contrast to the prediction with Star-CCM+ with which a lower value of about 6 was found. Most likely the too low value with Star-CCM+ is due to insufficient grid resolution.

5.7. THREE-DIMENSIONAL VERSUS TWO-DIMENSIONAL SIMULATIONS

Although a large number of CPUs could be used for the 3D Fluent simulations, the computational time for a typical single simulation is quite large (5-10 days). To reduce the computer time, an effort was made to map the three-dimensional configuration to a two-dimensional configuration (which will allow to use a 2D instead of a 3D solver). In order to translate the three-dimensional square configuration to a two-dimensional axisymmetric configuration an intermediate step has to be made. First from the three-dimensional square structure a three dimensional round structure is made, as is illustrated in figure 5.36. Here the small reservoir on the right of both configurations forms the inlet section where a pressure of 120 bara is imposed. At the

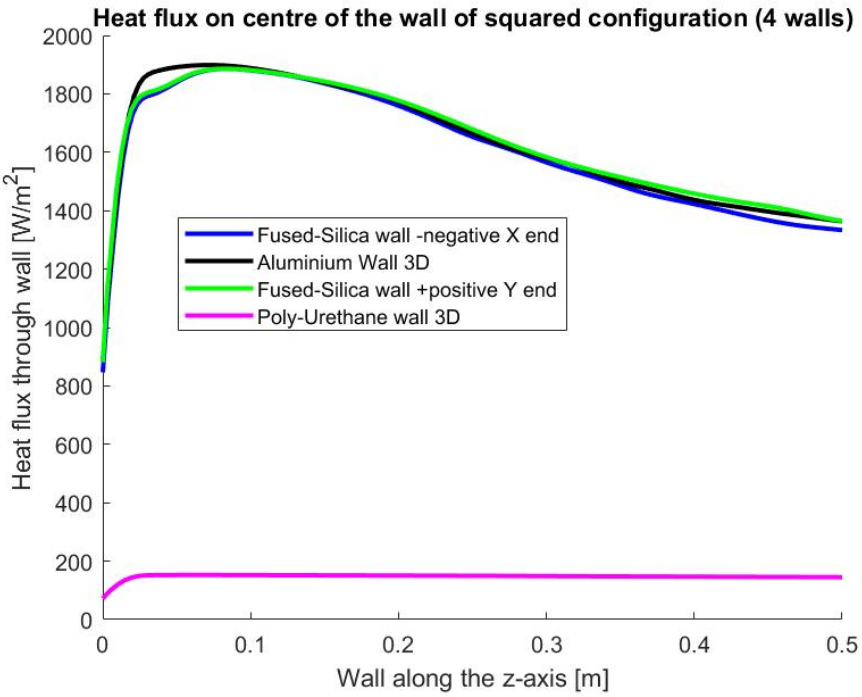

Figure 5.24: Heat transfer through all four walls of the three-dimensional domain.

Table 5.6: Number of cells used in each configuration.

Configuration	Cells
2D axisymmetric	80 755
3D Round	6 979 551
3D squared	8 347 936

outlet a pressure of 1 bara is imposed. The square test sectionis converted to a cylindrical section by using the hydraulic diameter, which is equal to 50 mm for a pipe (when starting from a square with 50 mm sides).

In the second mapping step, the three dimensional round configuration is converted to a two dimensional axisymmetric configuration, which is shown in figure 5.37. Here axisymmetry is assumed, which gives a 2D simulation with two coordinates, namely the streamwise coordinate and the radius r (with r=0 at the centreline). The same zones of refinement are used in the 2D domain as were used in the 3D domain. The number of grid cells is summarized in table 5.6. Note that only about 1% of the grid cells is needed in the 2D case compared to the 3D case. This also leads to a significant reduction is computer time.

5.7.1. RESULTS

The results obtained with the three configurations are compared. Figure 5.38 shows the Mach number along the centreline for the ideal gas (left) and for the real gas (right). The agreement for the three configurations is very good. Furthermore, the static temperature along the centreline is shown in (5.39); also here the agreement is very good. The good agreement for the flow behaviour can be explained by the fact that the walls are sufficiently far from the expanding jet to have a significant effect.

5.8. TWO-DIMENSIONAL NON-ADIABATIC CONFIGURATION

In order to map the 3D square case with non-adiabatic walls to the 2D axsymmetric case a proper transformation of the wall distance and thermal conductivity should be made. Therefore the total wall heat transfer Q should be the same:

$$Q_{Square} = Q_{Round} \tag{5.4}$$

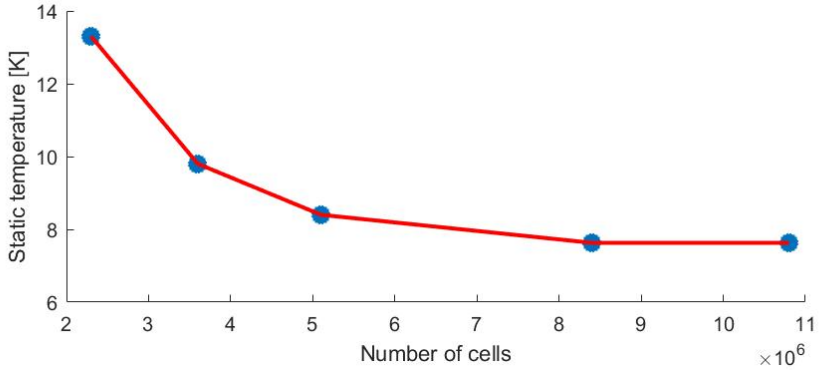

Figure 5.25: Mesh dependence of the value of the minimum static temperature in the domain.

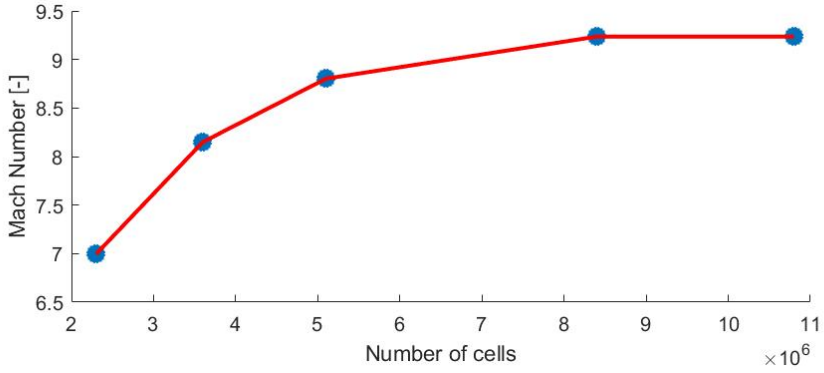

Figure 5.26: Mesh dependence of the maximum Mach number (i.e. just upstream of the shock).

$$Q_{AL} + Q_{Sili1} + Q_{sili2} + Q_{Urheen} = Q_{Round} \tag{5.5}$$

$$\begin{aligned} k_{AL} * S_{AL} \frac{\Delta T}{L_{AL}} + k_{Sili1} * S_{Sili1} \frac{\Delta T}{L_{Sili1}} + k_{Sili2} * S_{Sili2} \frac{\Delta T}{L_{Sili2}} + .. \\ .. + k_{Urheen} * S_{Urheen} \frac{\Delta T}{L_{Ureen}} = k_{Round} * S_{Round} \frac{\Delta T}{L_{Round}} \end{aligned} \tag{5.6}$$

Here k is the material conductivity, S is the wall length, and L is the wall thickness. Although ΔT will be different for each wall, it is assumed to have the same order of magnitude to obtain the following estimate:

$$\frac{k_{Round}}{L_{Round}} = 6619 \quad W/(m^2 K) \tag{5.7}$$

For the two dimensional Fluent calculations an aluminum wall was used (with k = 202 W/m/K). This corresponds to a thickness of 30.6 mm. This was applied in the two-dimensional axisymmetric Fluent calculations. Figure 5.40 compares the wall temperatures as obtained in the three-dimensional and in the two-dimensional configurations. In addition the wall heat transfer is compared in 5.41. There is a very good agreement between the results obtained in the three-dimensional and two-dimensional configurations. The reason for the different temperature at the beginning of the wall is the difference in geometry: in the square configuration the presence of the corner points form locally "dead zones" which are absent in the round configuration.

5.9. EXTENDED 2D ANALYSIS

So far Fluent simulations were performed with an outlet section (which is the section downstream of the orifice) of 0.5 m length. This is long enough the cover the jet with its Mach disk, as the jet is was found to reattach at the sides of the outlet section at a distance of 0.1 m. It was also found that taking a round outlet section (with a diameter of 0.05 m) instead of a rectangular section (with sides 0.05 m) has a negligible effect on the jet structure. Therefore to study the interaction between the jet and the wall heat transfer, it is sufficient to

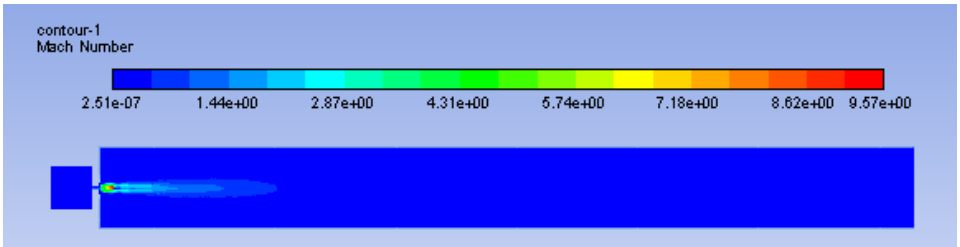

Figure 5.27: Mach contours for the case with non-adiabatic walls.

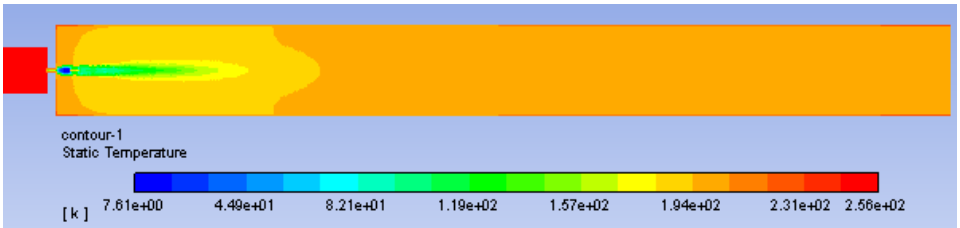

Figure 5.28: Temperature contours for the case with non-adiabatic walls.

carry out 2D axi-symmetric simulations with a cylindrical outlet section with 0.05 m diameter. For the case with a non-adiabatic wall, aluminum with a thickness of 30.6 mm was used.

To save computer time, 2D Fluent simulations with a non-adiabatic wall were carried out for a pipe without orifice. First a length of 0.5 was used, which was later increased to 5 m. The pipe configuration and boundary conditions is shown in figure 5.42. At the inlet a uniform velocity profile is described, with a total mass flow rate of 0.07 kg/s (being the critical rate through the orifice, when expanding from 120 bara to 1 bara). The inlet temperature is 196 K (which is the temperature found after insenthalpic expansion though the orifice). At pipe outlet the ambient pressure of 1 bara is prescribed. At the outer wall a heat transfer coefficient of 20 W/(m^{2}K) is prescribed with an ambient temperature of 20 ^{o}C. The following simulation results are obtained:

- The centreline velocity is shown in figure 5.43
- The centreline temperature is shown in figure 5.44
- The (inner) wall temperature is shown in figure 5.45
- The wall heat flux is shown in figure 5.46
- The Overall Heat Transfer Coefficient (OHTC) is shown in figure 5.47

All figures show the horizontal distance along the horizontal axis (starting at the inlet of the pipe, or at the outlet of the orifice in case an orifice is present). From the results for the centre velocity and for the centre temperature it is clear that it takes a distance of about 1.5 m before fully developed pipe flow is obtained. This means that thermal boundary layers develop along the wall, with an inner pipe temperature of (about) the isenthalpic expansion temperature of 196 K. The thermal boundary layer grows in streamwise direction, until the centre of the pipe is reached at about 1.5 m distance. From here on the centre temperature increases above the isenthalpic temperature due to heat inflow from the ambient. To verify the heat transfer results from the Fluent simulations, a simple analytical model can be used. The heat transfer through the boundary layer along the inner wall, through the pipe solid thickness, and between the outer wall and the ambient is given by the following formula:

$$OHTC = \frac{Q_W}{\pi D \Delta T} = \frac{2/D}{\frac{1}{\lambda_f}\frac{2}{Nu} + \frac{1}{\lambda_{AL}} ln\frac{D_{out}}{D} + \frac{2}{D_{out}\alpha_{amb}}} \tag{5.8}$$

Here:
OHTC is the overall heat transfer coefficient, with unit W/(m^{2}K)

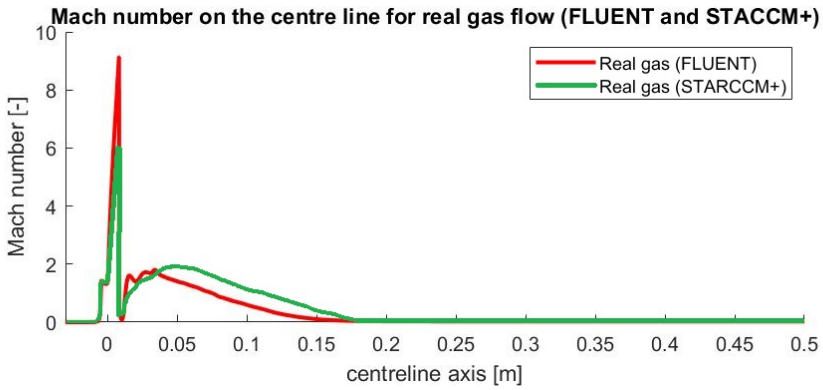

Figure 5.29: Comparison of Mach number at the centreline as obtained with Fluent in the current study and with STAR-CCM+ from [17].

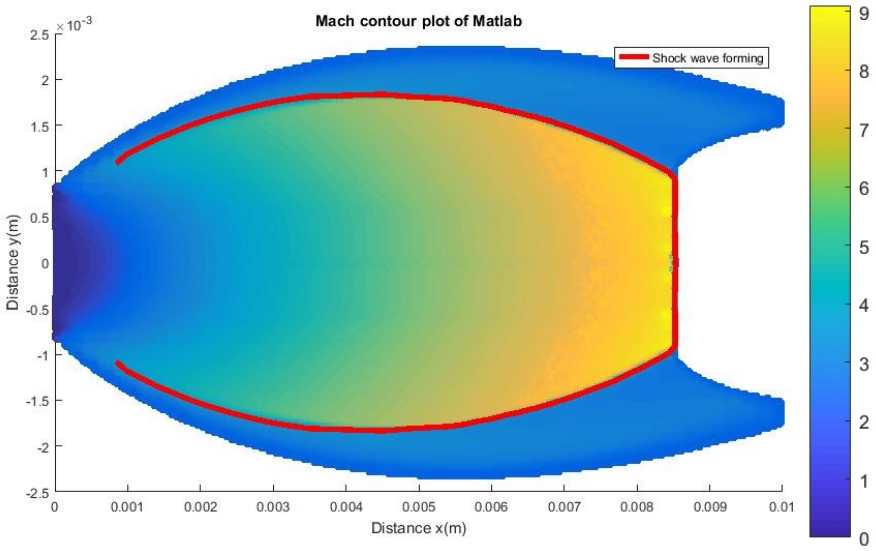

Figure 5.30: Mach number in the domain (MATLAB).

D is the inner pipe diameter, which is 0.05 m
D_{out} is the outer pipe diameter, which is 0.05+2*0.0306=0.1112 m
λ_f is the fluid conductivity, which is 0.0132 W/m/K
λ_{AL} is the conductivity of aluminum, which is 202 W/m/K
α_{amb} is the external heat transfer coefficient, is 20 W/m^2/K
ΔT is the characteristic temperature difference, taken as the difference between the ambient temperature (set to 20 ^{o}C) and the centre temperature
Nu is the Nusselt number, which is the dimensionless convective heat transfer in the thermal boundary layer, i.e. between the centre of the pipe and the inner wall surface.

The Nusselt number of fully turbulent pipe flow can be approximated with the the Dittus-Boelter correlation which reads

$$Nu = 0.023 Re^{0.8} Pr^{0.4} \tag{5.9}$$

Where Re is the Reynolds number (based on the inner pipe diameter, and the average velocity), which is about Re=1.08*10^5 for atmospheric pipe flow conditions, and Pr is the Prandtl number, which is 0.68 for those conditions. Taking a centre temperature of 196 K (which is the isenthalpic expansion temperarture), and using the values given above in the expression for the OHTC gives that the OHTC is 24 W/m^2/K. This is higher than the value of about 14 W/m^2/K found from the Fluent simulations, as shown in figure 5.47. The cause of the difference was not yet fully analysed, but can be due to the way in which the turbulence model in

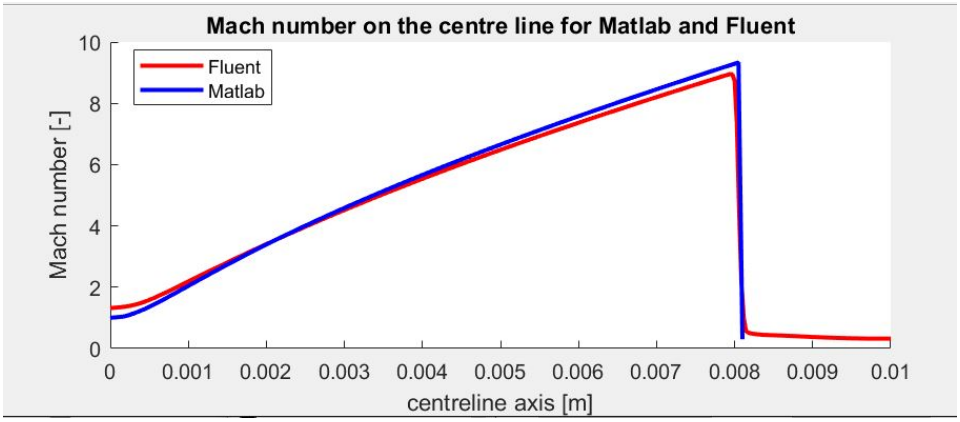

Figure 5.31: Mach number on the centreline; comparison of Fluent and MATLAB predictions.

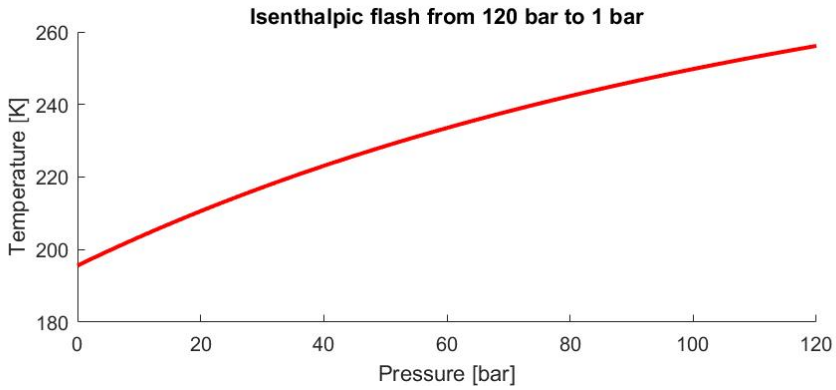

Figure 5.32: Isenthalpic flash of argon from 120 bara to 1 bara.

Fluent represents the thermal boundary layer which can give a convective heat transfer that is different from the Dittus-Boelter correlation. The OHTC is also quite dependent on the choice for the external heat transfer coefficient.

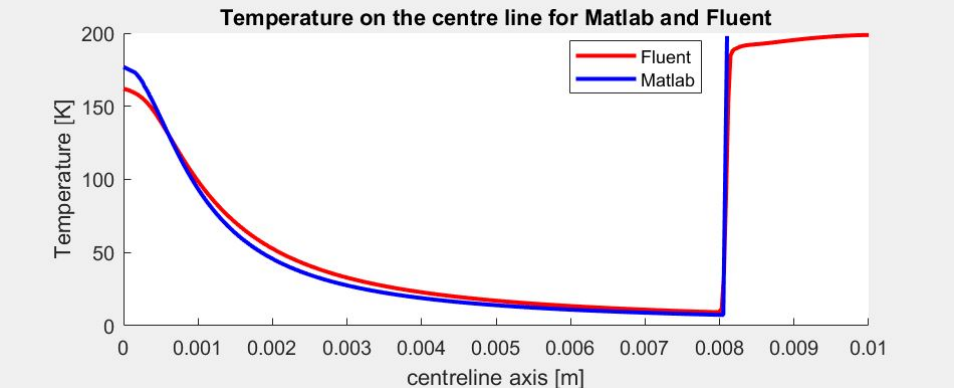

Figure 5.33: Static temperature on the centreline.

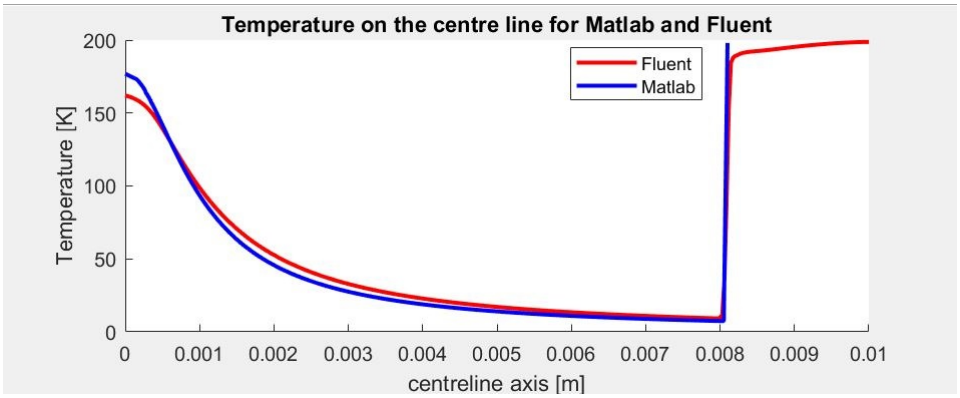

Figure 5.34: Velocity on the centreline.

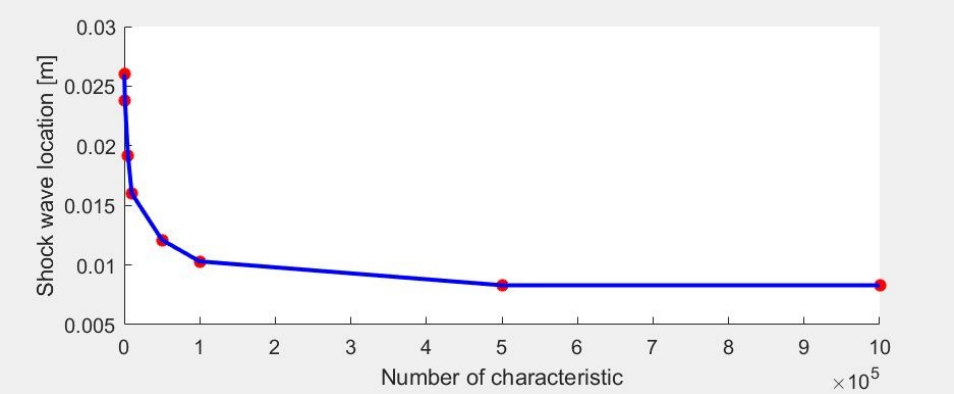

Figure 5.35: Location of the shock; dependence on the number of applied characteristics.

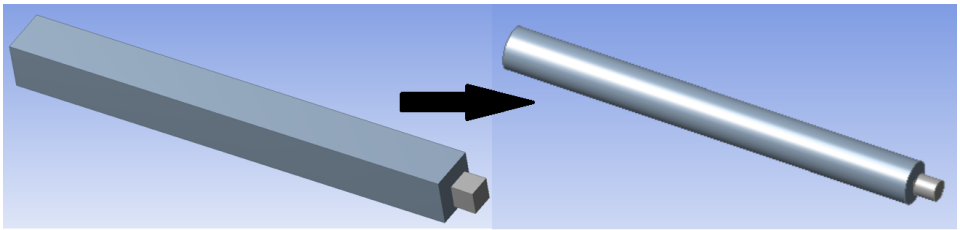

Figure 5.36: Conversion of square configuration to round configuration.

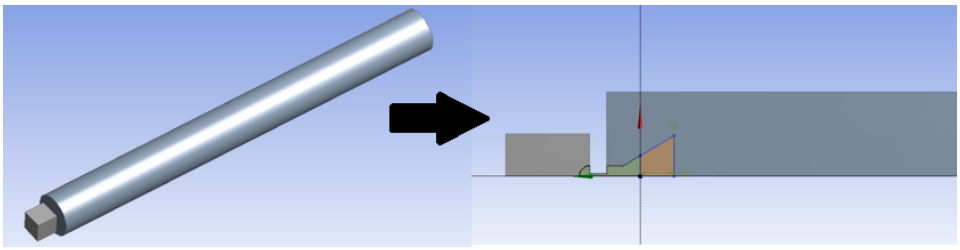

Figure 5.37: Conversion of three dimensional round configuration to the two dimensional axisymmetric configuration.

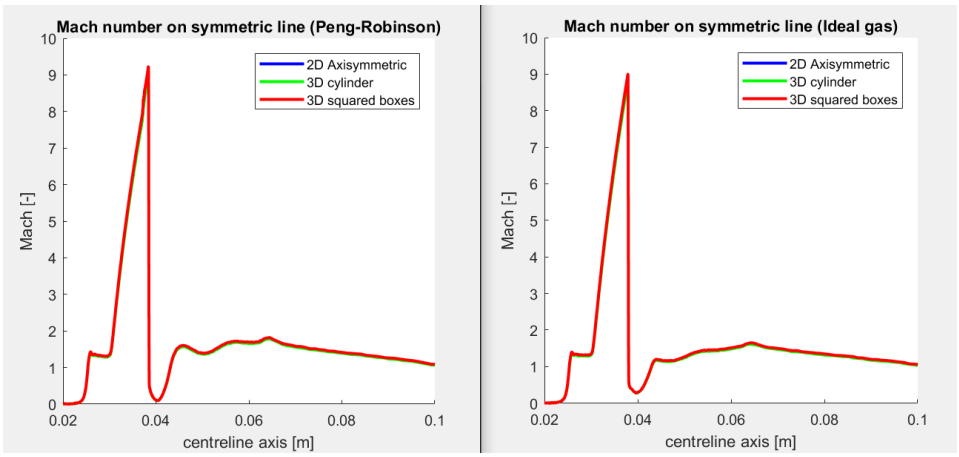

Figure 5.38: Comparison of the Mach number on the centreline as obtained for the three configurations.

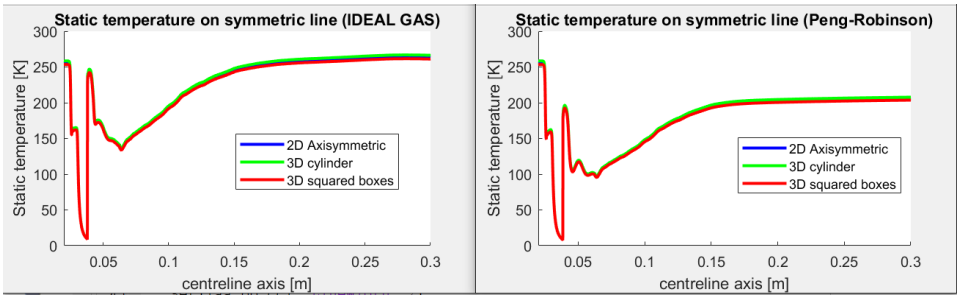

Figure 5.39: Comparison of the static temperature on the centreline as obtained for the three configurations.

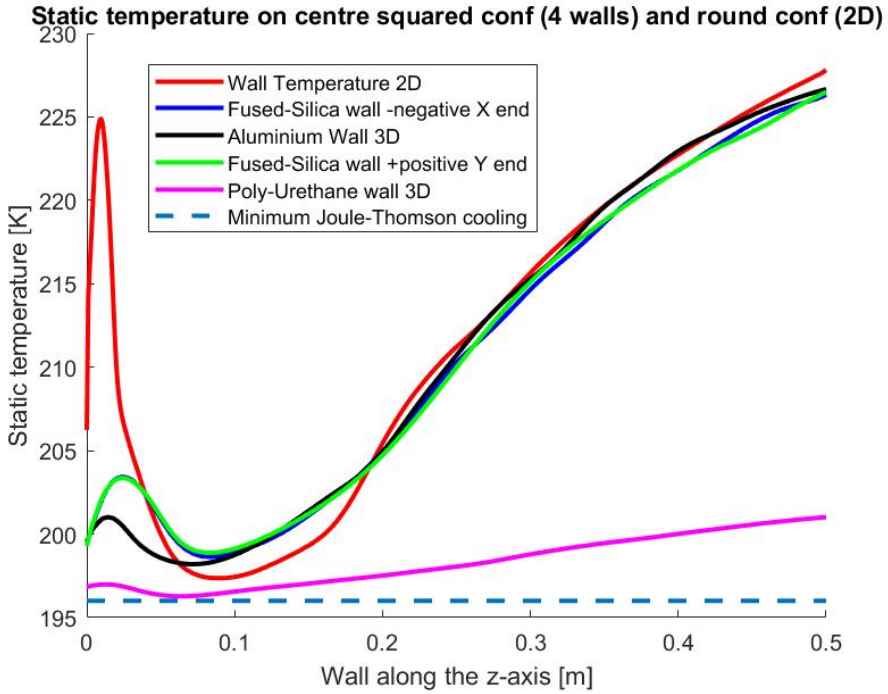

Figure 5.40: Static wall temperature for the three dimensional configuration (on all four walls) and for the two dimensional configuration (using the derived wall condition).

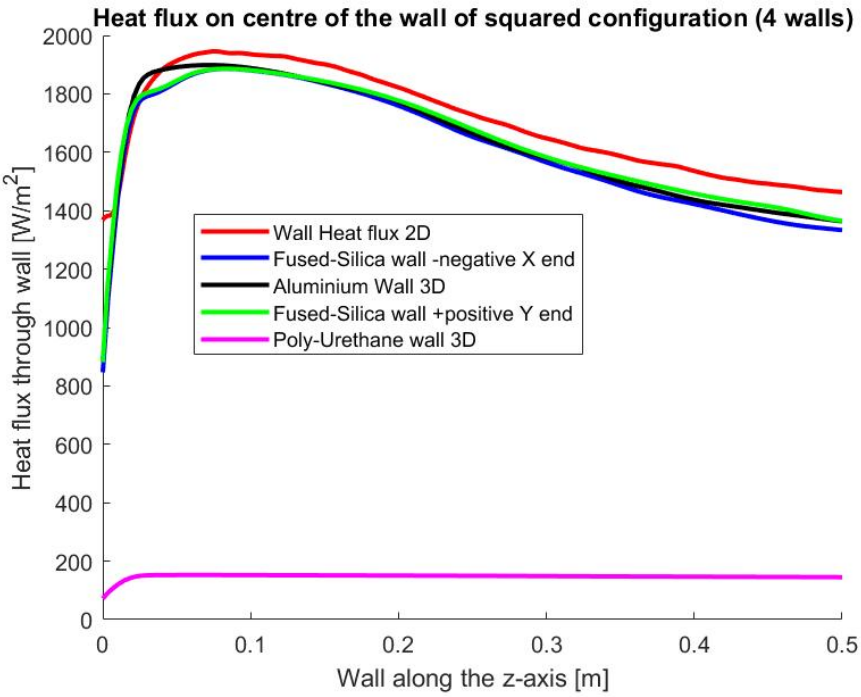

Figure 5.41: Wall heat transfer for the three dimensional configuration (through all four walls) and for the two dimensional configuration (using the derived wall condition).

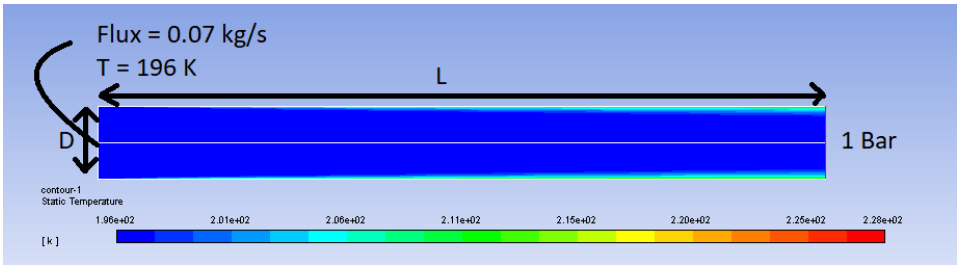

Figure 5.42: The model without the orifice.

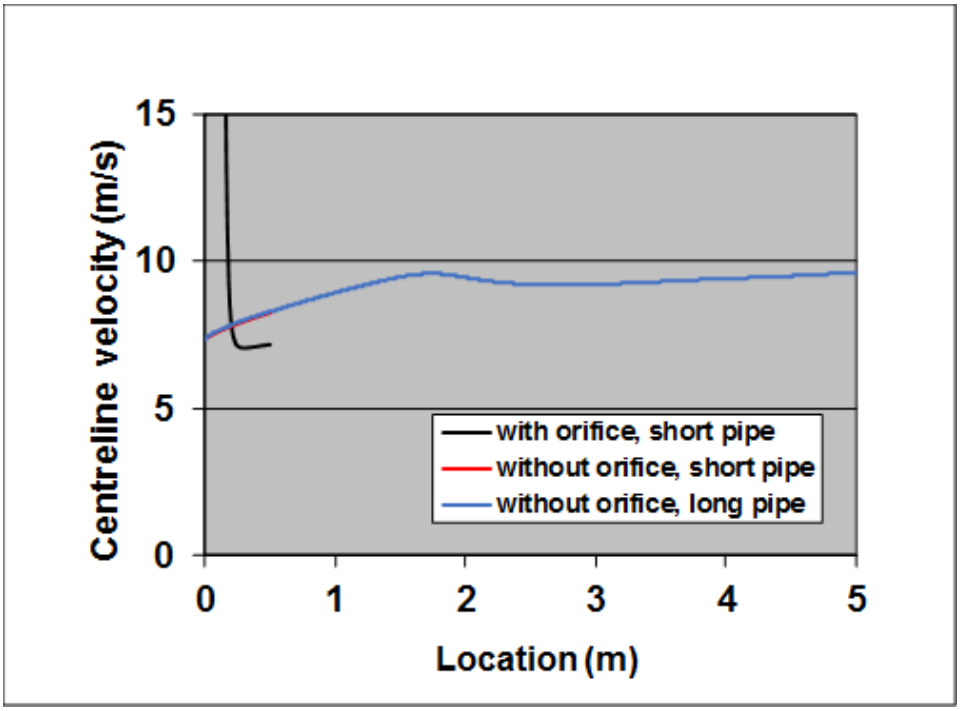

Figure 5.43: Velocity at the centreline in 2D Fluent simulation with non-adiabatic wall.

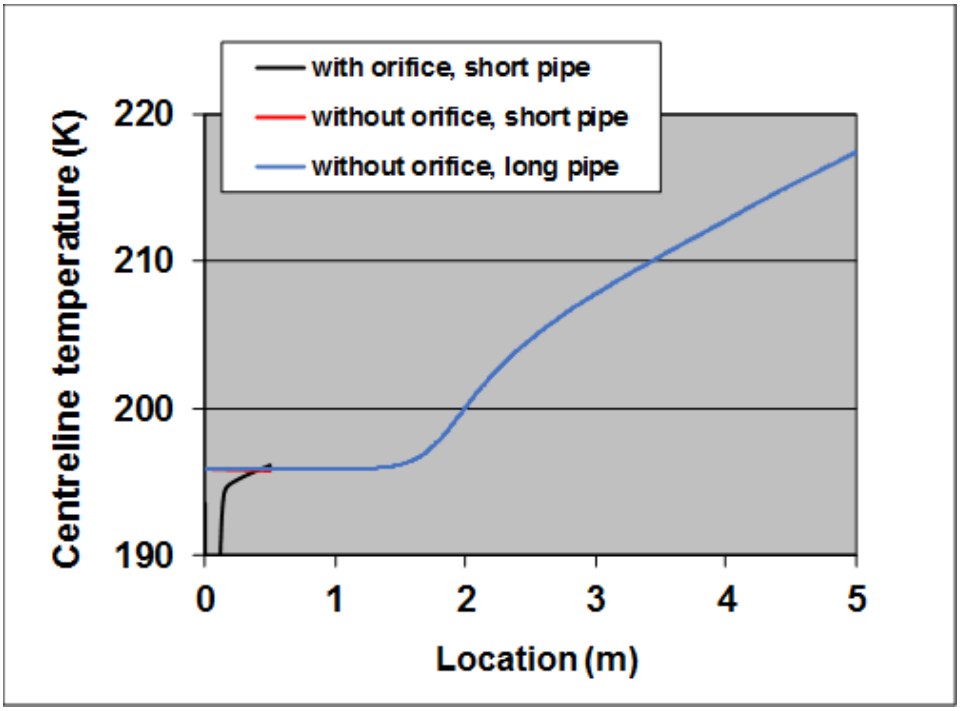

Figure 5.44: Temperature at the centreline in 2D Fluent simulation with non-adiabatic wall.

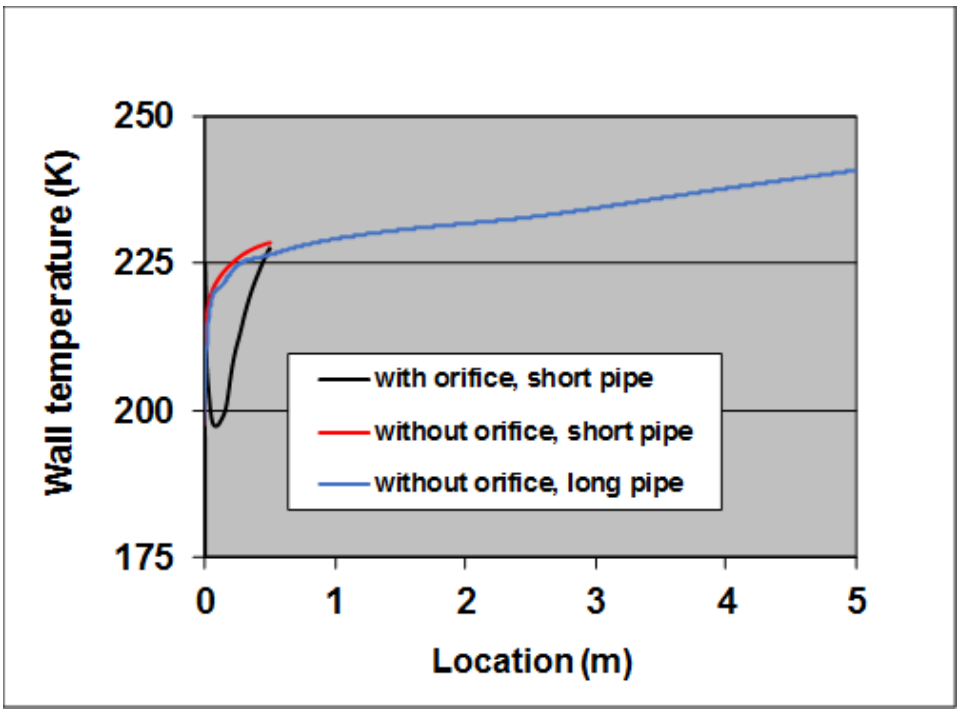

Figure 5.45: Wall temperature in 2D Fluent simulation with non-adiabatic wall.

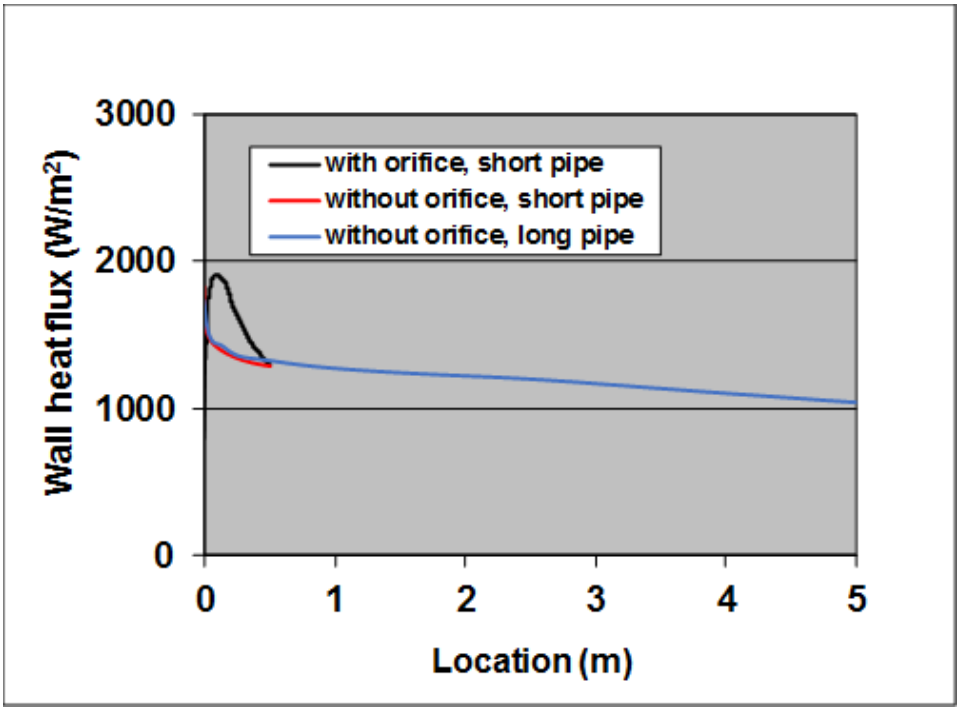

Figure 5.46: Wall heat transfer in 2D Fluent simulation with non-adiabatic wall.

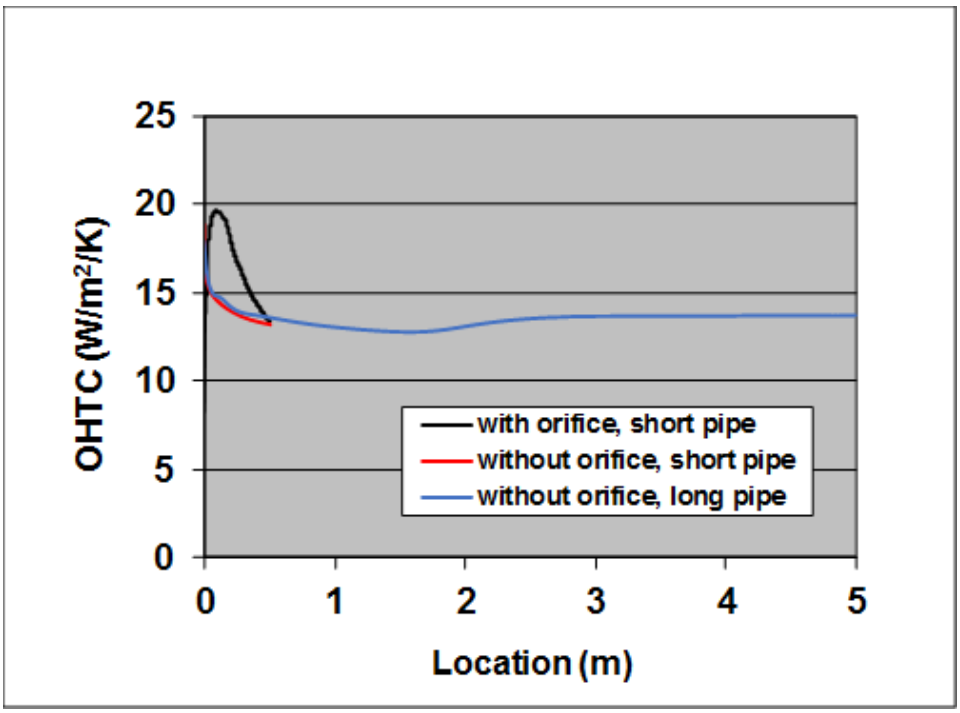

Figure 5.47: OHTC in 2D Fluent simulation with non-adiabatic wall.

6

CONCLUSIONS AND RECOMMENDATIONS

6.1. CONCLUSIONS

This study was aimed at improving the accuracy of the model predictions for the minimum fluid and inner wall temperatures for cold, low-pressure start-up of wells that produce oil or gas. Due to the large pressure drop over the well head choke, the so-called Joule-Thomson cooling will give a very low temperature of the expanding gas jet. Low-temperatures can give brittle fracture of the material in the piping downstream of the choke. Models are needed to verify whether the material temperature remains above the lower-design temperature. For this model validation, Imperial College in London (on request by Shell) has carried out lab experiments with argon gas that expands through an orifice from 120 bara to 1 bara. Awaiting the results of the lab experiments, detailed simulations were carried out in the present study using the Fluent CFD programme.

From the simulations the following conclusions can be drawn:

- The 3D, steady, compressible Reynolds-Averaged Navier-Stokes equations are solved with the SST $k-\omega$ model for the turbulence. The considered configuration is the same as in the lab. It consists of an upstream chamber with argon at 120 bara, that expands through a 5 mm long orifice with 1.55 mm diameter, into a square outlet section with 50 mm sides and 500 mm length. The inlet temperature is -17 ^{o}C and the outlet pressure is 1 bara. The supersonic flow leaving the orifice reaches a maximum Mach number of about 9 before a shock to subsonic flow is found. The jet reaches very low temperatures due to isentropic expansion (the minimum is 9 K), and reaches the isenthalpic expansion temperature of 196 K (or -77 ^{o}C) downstream of the shock. The jet reaches the sides of the outlet at a distance of about 100 mm.

- The maximum Mach number of about 9 predicted by Fluent is higher than the value of about 6 found in a previous simulation study that used the STAR-CCM+ CFD programme. To verify the Fluent results, the distributions of grid cells was varied and the number of grid cells was increased. Also a MATLAB programme was written that solved the inviscid compressible equations (Euler equations) for an axisymmetric jet. This confirmed the Fluent results.

- In addition to the 3D square outlet section, also 3D and 2D Fluent simulations were carried out for a cylindrical outlet (using an hydraulic diameter of 50 mm). The maximum Mach number and the jet structure (velocity, temperature) are not affected by the side walls. This is because the sides are sufficiently far from the jet.

- Furthermore, the temperature and the heat transfer at the walls of the outlet section were investigated. Thereto both adiabatic and non-adiabatic walls were considered. The ambient temperature is 20 ^{o}C. Thermal boundary layers are formed along the side walls, that are more or less exposed to a temperature of 196 K (the isenthalpic expansion temperature) in the centre of the pipe, up to a distance of about 1.5 m, where the outer edge of the boundary layer reaches the centre of the pipe. Thereafter the centre line temperature increases due to heat inflow from the ambient.

- The lowest temperature on the adiabatic and non-adiabatic walls is about the isenthalpic expansion temperature (196 K). For the non-adiabatic walls, the temperature rapidly increases in downstream

direction due to the heat inflow from the ambient. For the considered case, the wall temperature increases by 30 ^{o}C (from 196 K to 226 K, or from -77 ^{o}C to -47 ^{o}C) over a length as short as 0.5 m. These wall temperature results are of large importance for the design of brittle fracture prevention in engineering applications.

6.2. RECOMMENDATIONS

Recommendations for further research are the following:

- Imperial college has carried out lab experiments for the expanding jet. These consisted of Schlieren flow visualization, Particle Image Velocimetry (PIV) for the velocities, thermocouples for the temperature, and phosphoric temperature measurement with laser-induced phosphor thermometry (phosphorescence) (both for the wall surface temperature and for the flowing fluid temperature). These data still need to be processed. Once available, the experimental data can be used for the validation of the CFD results.
- Use simple 1D flow and heat transfer models (of the type that is used in engineering design in the oil and gas industry) in a further comparison with the CFD results.
- Include the effect of droplet formation in the cold expansion zones in the CFD simulations. This requires a multiphase flow simulation.
- Carry out additional simulations for the axisymmetric configuration. This can include parameter variation, such as different expansion rates and larger pipe diameters.

BIBLIOGRAPHY

[1] ANSYS. *FLUENT 6.3 User's Guide*. Nov. 2017. URL: https://www.sharcnet.ca/Software/Fluent6/index.htm.

[2] P. Bakker and B. Van Leer. *Lecture Notes on Gasdynamics AE4-140*. Delft University of Technology and University of Michigan, 2006.

[3] A. C. Bayeh. "Analysis of Mach disks from an underexpanded nozzle using experimental and computational methods". In: *47^{th} AIAA Aerospace Sciences Meeting Including The New Horizons Forum and Aerospace Exposition, Orlando, Florida* (2009).

[4] V. M. Boiko, V. I. Zapryagaev, and S. V. Poplavski. "Correction of PIV data for reconstruction of the gas velocity in a supersonic under-expanded jet". In: *Combustion, Explosion, and Shock Waves* 51 (2015), pp. 587–596.

[5] S. Crist, D. R. Glass, and P. M. Sherman. "Study of the highly underexpanded sonic jet." In: *AIAA Journal* 4 (1966), pp. 68–71.

[6] Design and Engineering Practice 30.10.02.31-Gen. "Metallic materials – Prevention of brittle fracture". In: *Shell Internal Report* (2010).

[7] W. Graebel. *Advanced Fluid Mechanics*. Elsevier India, 2000.

[8] R. Levenduski and R. Scarlotti. *Joule-Thomson cryocooler for space applications*. Elsevier, 1996.

[9] Y.H. Liu and G. Ai. "Numerical study on the heat transfer in the leakage of pressure vessels considering the Joule-Thomson cooling effect". In: *14^{th} Int. Conference on Pressure Vessel Technology* (2015).

[10] E. Love and C. Grigsby. "Studies of axisymmetric free jets exhausting from sonic and supersonic nozzles into still air and into supersonic streams". In: *National Advisory Committee for Aeronautics Collection* (1955).

[11] D. Priscoy M. M. Orescanin and J. M. Austinz. "Exhaust of Underexpanded Jets from Finite Reservoirs". In: *40^{th} Fluid Dynamics Conference and Exhibit (Chicago,illinois)* (July 2010).

[12] NASA. *Normal shock wave*. Nov. 2017. URL: https://www.grc.nasa.gov/WWW/K-12/airplane/normal.html.

[13] D. C. Pack. "A note on Prandtl's formula for the wave-length of a supersonic gas jet". In: *Quarterly J. Mech. and Appl. Math.* 3 (1950), pp. 173–181.

[14] S. B. Pope. *Turbulent flows*. Cambridge: Cambridge University Press, 2000.

[15] B.N. Roy. *Fundamentals of Classical and Statistical Thermodynamics*. Wiley, 2000.

[16] M.A. Saad. *Compressible Fluid Flow*. Vol. 2. Prentice Hall, 1993.

[17] S. Shankar and C. T'Joen. "Study of Joule-Thomson cooling in freely expanding flows simulation and experimental validation". In: *Shell Internal Report* (2016).

[18] A.H. Shapiro. *The Dynamics and Thermodynamics of Compressible Fluid Flow*. Vol. 1. The Ronald Press company, New York, 1953.

[19] W. Vickrey. "The Esso gas plant explosion". In: *Annual Symposium of the Business Forms Management Association* 16 (2006).

A

APPENDIX A

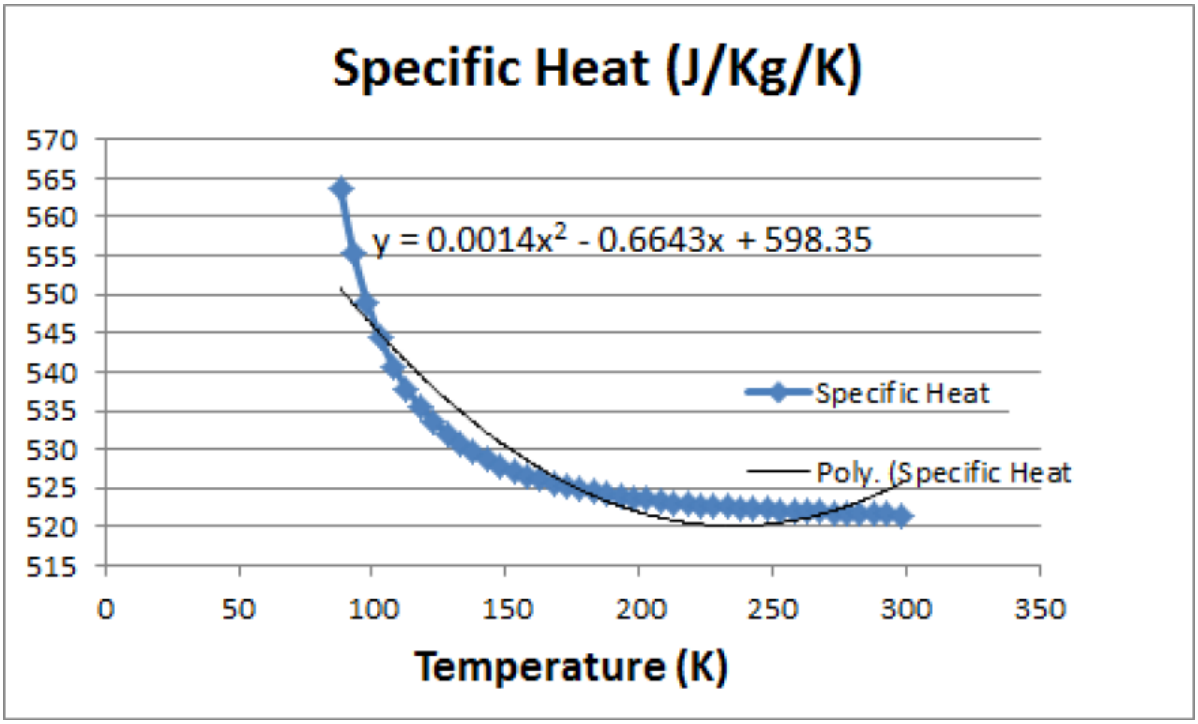

Figure A.1: Temperature dependent specific heat capacity of Argon gas at atmospheric pressure. source: http://webbook.nist.gov/

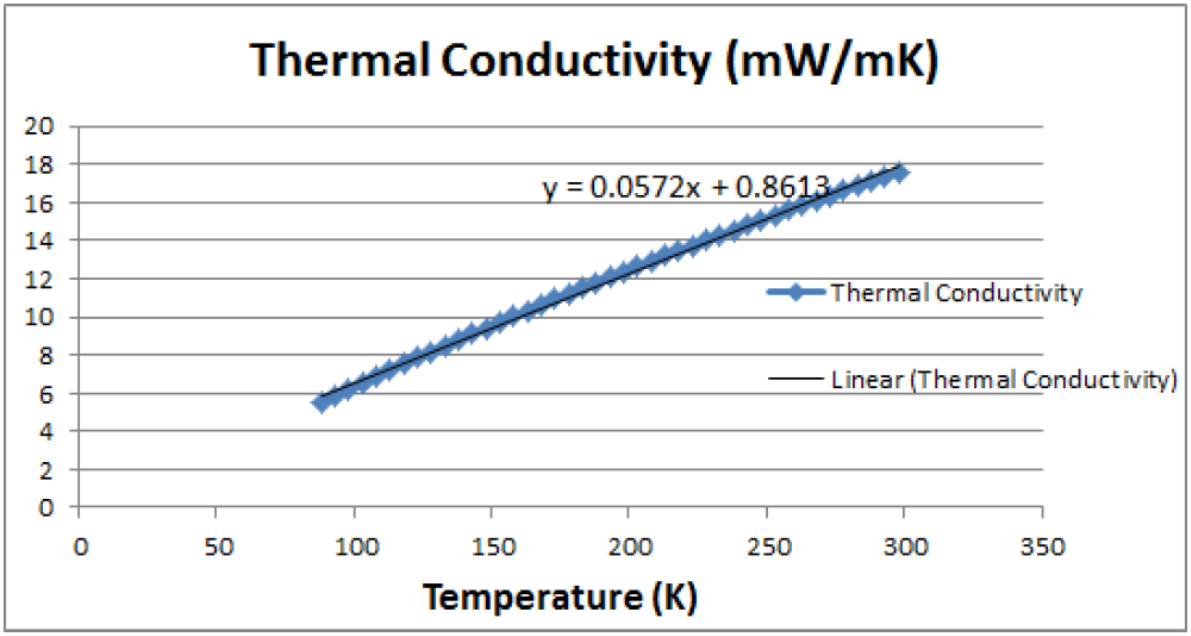

Figure A.2: Temperature dependent thermal conductivity of Argon gas at atmospheric pressure. source:http://webbook.nist.gov/

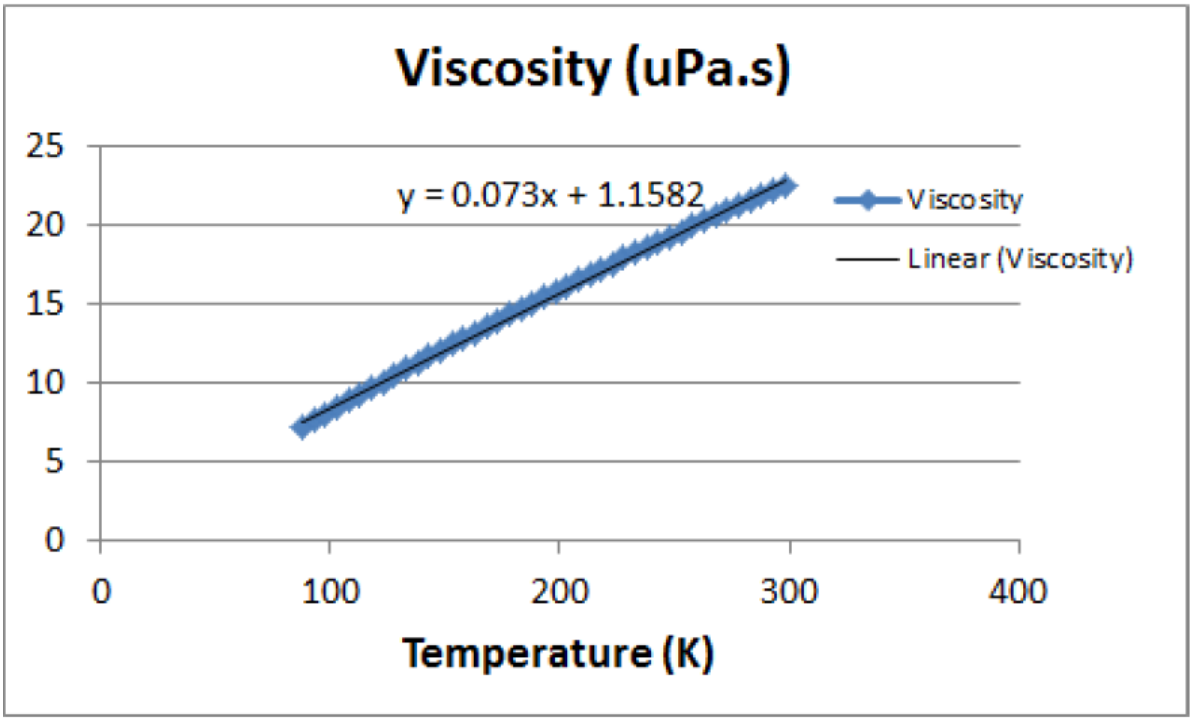

Figure A.3: Temperature dependent viscosity of Argon gas at atmospheric pressure. source: http://webbook.nist.gov/

B

APPENDIX B

```
1
2
3  end1 = 0;
4  %S = 1+C;
5  vv = 1;
6
7  for S = 1+C
8  kk = S;
9  r(S) = 0;
10 Theta(S) = 0;
11 f4(kk) = tand(Theta(S-C)-mu(S-C));
12 f5(kk) = 1/(tand(mu(S-C))*M(S-C)*(1+(k-1)/2*M(S-C)^2));
13 f6(kk) = sind(Theta(S-C))*sind(mu(S-C))/(r(S-C)*cosd(Theta(S-C)-mu(S-C)));
14
15 x(S) = x(S-C) - r(S-C)/(f4(kk));
16 M(S) = (degtorad(Theta(S-C)) + f6(kk)*(x(S)-x(S-C)))*(f5(kk)) + M(S-C);
17 mu(S) = asind(1/M(S));
18
19 [¬,nu(S-C),¬] =flowprandtlmeyer(k,M(S-C),'mach');
20
21 con = 1;
22 while con > 1e-10
23 vv = vv +1 ;
24
25 f4(kk) = tand((Theta(S-C)-mu(S-C)+Theta(S)-mu(S))/2);
26 x_new = x(S-C) - r(S-C)/(f4(kk));
27
28 f5(kk) = 0.5*(1/(tand(mu(S-C))*M(S-C)*(1+(k-1)/2*M(S-C)^2)))+ ...
29    0.5*(1/(tand(mu(S))*M(S)*(1+(k-1)/2*M(S)^2)));
30 [¬,nu_2,¬] =flowprandtlmeyer(k,M(S),'mach');
31 f6(kk) = 0.5*sind(Theta(S-C))*sind(mu(S-C)/(r(S-C)*cosd(Theta(S-C)-mu(S-C)))- ...
32    0.5*cotd(mu(S-C))*(degtorad(nu_2)-degtorad(nu(S-C)))/(x_new-x(S-C)));
33
34 M(S) = (degtorad(Theta(S-C)) + HULP*f6(kk)*(x(S)-x(S-C)))*(f5(kk)) + M(S-C);
35 mu(S) = asind(1/M(S));
36 con(vv) = abs(x_new-x(S));
37 x(S) = x_new;
38
39 end
40
41 for kk = S+1:S+C-2
42
43 f1(kk) = tand(Theta(kk-1)+mu(kk-1));
44 f2(kk) = 1/(tand(mu(kk-1))*M(kk-1)*(1+(k-1)/2*M(kk-1)^2));
45 if r(kk-1) > 0
46    f3(kk) = sind(Theta(kk-1))*sind(mu(kk-1))/(r(kk-1)*cosd(Theta(kk-1)+mu(kk-1)));
47    else
48    f3(kk) = 0;
49 end
```

```
50
51  f4(kk) = tand(Theta(kk-C)-mu(kk-C));
52  f5(kk) = 1/(tand(mu(kk-C))*M(kk-C)*(1+(k-1)/2*M(kk-C)^2));
53  f6(kk) = sind(Theta(kk-C))*sind(mu(kk-C))/(r(kk-C)*cosd(Theta(kk-C)-mu(kk-C)));
54
55  AA = [1 -f1(kk) ; 1 -f4(kk)];
56  BB = [-f1(kk)*x(kk-1)+r(kk-1) ; -f4(kk)*x(kk-C)+r(kk-C)];
57  r_x = AA\BB;
58
59  r(kk) = r_x(1);
60  x(kk) = r_x(2);
61
62  AA = [f2(kk) -1; f5(kk) +1];
63  BB = [HULP*f3(kk)*(x(kk)-x(kk-1)) - degtorad(Theta(kk-1)) + f2(kk)*M(kk-1) ; ...
        HULP*f6(kk)*(x(kk)-x(kk-C)) + degtorad(Theta(kk-C)) + f5(kk)*M(kk-C) ];
64  M_T = AA\BB;
65  M(kk) = M_T(1);
66  Theta(kk) = radtodeg(M_T(2));
67  mu(kk) = asind(1/M(kk));
68  conv = 1;
69
70  while conv>1e-10
71  f1(kk) = tand((Theta(kk-1)+mu(kk-1)+Theta(kk)+mu(kk))/2);
72  f2(kk) = 0.5*(1/(tand(mu(kk-1))*M(kk-1)*(1+(k-1)/2*M(kk-1)^2)))+...
73     +0.5*(1/(tand(mu(kk))*M(kk)*(1+(k-1)/2*M(kk)^2)));
74  if r(kk-1) > 0
75     f3(kk) = ...
           0.5*(sind(Theta(kk-1))*sind(mu(kk-1))/(r(kk-1)*cosd(Theta(kk-1)+mu(kk-1))))+...
76        +0.5*(sind(Theta(kk))*sind(mu(kk))/(r(kk)*cosd(Theta(kk-1)+mu(kk))));
77  else
78     [¬,nu_c,mu_c] =flowprandtlmeyer(k,M(kk),'mach');
79     [¬,nu_b,¬] =flowprandtlmeyer(k,M(kk-1),'mach');
80     f3(kk) = 0.5*(sind(Theta(kk))*sind(mu(kk))/(r(kk)*cosd(Theta(kk)+mu(kk))))+...
81        +0.5*cotd(mu_c)*(degtorad(nu_c)-degtorad(nu_b))/(x(kk)-x(kk-1))));
82  end
83
84  f4(kk) = tand((Theta(kk-C)-mu(kk-C)+Theta(kk)-mu(kk))/2);
85  f5(kk) = 0.5*(1/(tand(mu(kk-C))*M(kk-C)*(1+(k-1)/2*M(kk-C)^2))+...
86     +1/(tand(mu(kk))*M(kk)*(1+(k-1)/2*M(kk)^2)));
87  f6(kk) = 0.5*(sind(Theta(kk-C))*sind(mu(kk-C))/(r(kk-C)*cosd(Theta(kk-C)-mu(kk-C))))+...
88     +0.5*(sind(Theta(kk))*sind(mu(kk))/(r(kk)*cosd(Theta(kk)-mu(kk)))));
89
90  AA = [1 -f1(kk) ; 1 -f4(kk)];
91  BB = [-f1(kk)*x(kk-1)+r(kk-1) ; -f4(kk)*x(kk-C)+r(kk-C)];
92  r_x = AA\BB;
93
94  conv = abs(x(kk)-r_x(2));
95
96  r(kk) = r_x(1);
97  x(kk) = r_x(2);
98  AA = [f2(kk) -1; f5(kk) +1];
99  BB = [HULP*f3(kk)*(x(kk)-x(kk-1)) - degtorad(Theta(kk-1)) + f2(kk)*M(kk-1) ; ...
        HULP*f6(kk)*(x(kk)-x(kk-C)) + degtorad(Theta(kk-C)) + f5(kk)*M(kk-C) ];
100
101 M_T = AA\BB;
102 M(kk) = M_T(1);
103 Theta(kk) = radtodeg(M_T(2));
104 mu(kk) = asind(1/M(kk));
105
106 end
107 if x(kk) < x(kk-1)
108 Theta(kk) = (Theta(kk)+Theta(kk-1))/2;
109 x(kk)= x(kk-1);
110 r(kk)= r(kk-1);
111 end
112
113 end
114
115 kk = kk + 1;
116 f1(kk) = tand(Theta(kk-1)+mu(kk-1));
117 f4(kk) = tand(Theta(kk-C)-mu(kk-C));
```

```
f6(kk) = sind(Theta(kk-C))*sind(mu(kk-C))/(r(kk-C)*cosd(Theta(kk-C)-mu(kk-C)));



AA = [1 -f1(kk) ; 1 -f4(kk)];
BB = [-f1(kk)*x(kk-1)+r(kk-1) ; -f4(kk)*x(kk-C)+r(kk-C)];
r_x = AA\BB;

r(kk) = r_x(1);
x(kk) = r_x(2);
M(kk) = M(kk-C);
mu(kk) = asind(1/M(kk));

Theta(kk) = Theta(kk-C)+radtodeg(HULP*f6(kk)*(x(kk)-x(kk-C)));

conv = 1;

while conv>1e-10

f4(kk) = tand((Theta(kk-C)+Theta(kk))/2);

f1(kk) = tand((Theta(kk-1)+mu(kk-1)+Theta(kk)+mu(kk))/2);
f2(kk) = 0.5*(1/(tand(mu(kk-1))*M(kk-1)*(1+(k-1)/2*M(kk-1)^2)))+...
   +0.5*(1/(tand(mu(kk))*M(kk)*(1+(k-1)/2*M(kk)^2))));
f3(kk) = 0.5*(sind(Theta(kk-1))*sind(mu(kk-1))/(r(kk-1)*cosd(Theta(kk-1)+...
   +mu(kk-1))))+0.5*(sind(Theta(kk))*sind(mu(kk))/(r(kk)*cosd(Theta(kk-1)+mu(kk)))));


AA = [1 -f1(kk) ; 1 -f4(kk)];
BB = [-f1(kk)*x(kk-1)+r(kk-1) ; -f4(kk)*x(kk-C)+r(kk-C)];
r_x = AA\BB;

conv = abs(x(kk)-r_x(2));

r(kk) = r_x(1);
x(kk) = r_x(2);
M(kk) = M(kk-C);
mu(kk) = asind(1/M(kk));

Theta(kk) = Theta(kk-1)+radtodeg(f2(kk)*(M(kk)-M(kk-C))-HULP*f3(kk)*(x(kk)-x(kk-1)));

end
end

ss = 1;

for S = 1+C+C:C:1+C^2%:1+2*C
Start = S;
clear gem
kk = S;
gem = 1;
r(S) = 0;
Theta(S) = 0;
f4(kk) = tand(Theta(S-C+1)-mu(S-C+1));
f5(kk) = 1/(tand(mu(S-C+1))*M(S-C+1)*(1+(k-1)/2*M(S-C+1)^2));
f6(kk) = sind(Theta(S-C+1))*sind(mu(S-C+1))/(r(S-C+1)*cosd(Theta(S-C+1)-mu(S-C+1)));

x(S) = x(S-C+1) - r(S-C+1)/(f4(kk));
M(S) = (degtorad(Theta(S-C+1)) + HULP*f6(kk)*(x(S)-x(S-C+1)))*(f5(kk)) + M(S-C+1);
mu(S) = asind(1/M(S));

[¬,nu(S-C+1),¬] =flowprandtlmeyer(k,M(S-C+1),'mach');

con = 1;
while con > 1e-10
vv = vv +1 ;

f4(kk) = tand((Theta(S-C+1)-mu(S-C+1)+Theta(S)-mu(S))/2);
x_new = x(S-C+1) - r(S-C+1)/(f4(kk));

f5(kk) = 0.5*(1/(tand(mu(S-C+1))*M(S-C+1)*(1+(k-1)/2*M(S-C+1)^2))+...
```

```
   +1/(tand(mu(S))*M(S)*(1+(k-1)/2*M(S)^2)));
[¬,nu_2,¬] =flowprandtlmeyer(k,M(S),'mach');
f6(kk) = ...
    0.5*(sind(Theta(S-C+1))*sind(mu(S-C+1))/(r(S-C+1)*cosd(Theta(S-C+1)-mu(S-C+1)))- ...
    0.5*cotd(mu(S-C+1))*(degtorad(nu_2)-degtorad(nu(S-C+1)))/(x_new-x(S-C+1)));

M(S) = (degtorad(Theta(S-C+1)) + HULP*f6(kk)*(x(S)-x(S-C+1)))*(f5(kk)) + M(S-C+1);
mu(S) = asind(1/M(S));
con(vv) = abs(x_new-x(S));
x(S) = x_new;

end


for kk = S+1:S+C-2;
kk
f1(kk) = tand(Theta(kk-1)+mu(kk-1));
f2(kk) = 1/(tand(mu(kk-1))*M(kk-1)*(1+(k-1)/2*M(kk-1)^2));
if r(kk-1) > 0
   f3(kk) = sind(Theta(kk-1))*sind(mu(kk-1))/(r(kk-1)*cosd(Theta(kk-1)+mu(kk-1)));
   else
   f3(kk) = 0;
end

f4(kk) = tand(Theta(kk-C+1)-mu(kk-C+1));
f5(kk) = 1/(tand(mu(kk-C+1))*M(kk-C+1)*(1+(k-1)/2*M(kk-C+1)^2));
f6(kk) = sind(Theta(kk-C+1))*sind(mu(kk-C+1))/(r(kk-C+1)*cosd(Theta(kk-C+1)-mu(kk-C+1)));

AA = [1 -f1(kk) ; 1 -f4(kk)];
BB = [-f1(kk)*x(kk-1)+r(kk-1) ; -f4(kk)*x(kk-C+1)+r(kk-C+1)];
r_x = AA\BB;

r(kk) = r_x(1);
x(kk) = r_x(2);

AA = [f2(kk) -1; f5(kk) +1];
BB = [HULP*f3(kk)*(x(kk)-x(kk-1)) - degtorad(Theta(kk-1)) + f2(kk)*M(kk-1) ; ...
    HULP*f6(kk)*(x(kk)-x(kk-C+1)) + degtorad(Theta(kk-C+1)) + f5(kk)*M(kk-C+1) ];
M_T = AA\BB;
M(kk) = M_T(1);
Theta(kk) = (M_T(2));
mu(kk) = asind(1/M(kk));
conv = 1;

while conv>1e-10
f1(kk) = tand((Theta(kk-1)+mu(kk-1)+Theta(kk)+mu(kk))/2);
f2(kk) = 0.5*(1/(tand(mu(kk-1))*M(kk-1)*(1+(k-1)/2*M(kk-1)^2))+...
   +1/(tand(mu(kk))*M(kk)*(1+(k-1)/2*M(kk)^2)));
if r(kk-1) > 0
   f3(kk) = ...
       0.5*(sind(Theta(kk-1))*sind(mu(kk-1))/(r(kk-1)*cosd(Theta(kk-1)+mu(kk-1)))+...
      +sind(Theta(kk))*sind(mu(kk))/(r(kk)*cosd(Theta(kk-1)+mu(kk))));
else
   [¬,nu_c,mu_c] =flowprandtlmeyer(k,M(kk),'mach');
   [¬,nu_b,¬] =flowprandtlmeyer(k,M(kk-1),'mach');
   f3(kk) = 0.5*(sind(Theta(kk))*sind(mu(kk))/(r(kk)*cosd(Theta(kk)+mu(kk)))+...
      +0.5*cotd(mu_c)*(degtorad(nu_c)-degtorad(nu_b))/(x(kk)-x(kk-1)));
end

f4(kk) = tand((Theta(kk-C+1)-mu(kk-C+1)+Theta(kk)-mu(kk))/2);
f5(kk) = 0.5*(1/(tand(mu(kk-C+1))*M(kk-C+1)*(1+(k-1)/2*M(kk-C+1)^2))+...
   +1/(tand(mu(kk))*M(kk)*(1+(k-1)/2*M(kk)^2)));
f6(kk) = ...
    0.5*(sind(Theta(kk-C+1))*sind(mu(kk-C+1))/(r(kk-C+1)*cosd(Theta(kk-C+1)-mu(kk-C+1)))+
   ...+sind(Theta(kk))*sind(mu(kk))/(r(kk)*cosd(Theta(kk)-mu(kk))));

AA = [1 -f1(kk) ; 1 -f4(kk)];
BB = [-f1(kk)*x(kk-1)+r(kk-1) ; -f4(kk)*x(kk-C+1)+r(kk-C+1)];
r_x = AA\BB;

conv = abs(x(kk)-r_x(2));
```

```
255
256 r(kk) = r_x(1);
257 x(kk) = r_x(2);
258 AA = [f2(kk) -1; f5(kk) +1];
259 BB = [HULP*f3(kk)*(x(kk)-x(kk-1)) - degtorad(Theta(kk-1)) + f2(kk)*M(kk-1) ; ...
        HULP*f6(kk)*(x(kk)-x(kk-C+1)) + degtorad(Theta(kk-C+1)) + f5(kk)*M(kk-C+1) ];
260
261 M_T = AA\BB;
262 M(kk) = M_T(1);
263 Theta(kk) = radtodeg(M_T(2));
264 mu(kk) = asind(1/M(kk));
265
266 end
267
268 if x(kk) ≤x(kk-1)
269    if end1 == 0
270       Pre_shock_M = M(kk-1);
271       Pre_shock_Theta = Theta(kk-1);
272       Pre_shock_n = kk - 1;
273    end
274
275    end1 = 1;
276
277    post_shock_M = M(kk);
278    post_shock_Theta = Theta(kk);
279    post_shock_n = kk;
280
281    SAVE(ss) = kk-1;
282    ss = ss + 1;
283    SAVE(ss) = kk;
284    ss = ss +1;
285
286
287    x_mean = mean(x(unique(SAVE)));
288    r_mean = mean(r(unique(SAVE)));
289    M_mean = mean(M(unique(SAVE)));
290    Theta_mean = mean(Theta(unique(SAVE)));
291    mu_mean = mean(mu(unique(SAVE)));
292
293
294    x(unique(SAVE)) = x_mean;
295    r(unique(SAVE)) = r_mean;
296    M(unique(SAVE)) = M_mean;
297    Theta(unique(SAVE)) = Theta_mean;
298    mu(unique(SAVE)) = mu_mean;
299
300 end
301
302 end
303
304 kk = kk + 1;
305 f1(kk) = tand(Theta(kk-1)+mu(kk-1));
306 f4(kk) = tand(Theta(kk-C)-mu(kk-C));
307 f6(kk) = sind(Theta(kk-C))*sind(mu(kk-C))/(r(kk-C)*cosd(Theta(kk-C)-mu(kk-C)));
308
309
310
311 AA = [1 -f1(kk) ; 1 -f4(kk)];
312 BB = [-f1(kk)*x(kk-1)+r(kk-1) ; -f4(kk)*x(kk-C)+r(kk-C)];
313 r_x = AA\BB;
314
315 r(kk) = r_x(1);
316 x(kk) = r_x(2);
317 M(kk) = M(kk-C);
318 mu(kk) = asind(1/M(kk));
319
320 Theta(kk) = Theta(kk-C)+radtodeg(f6(kk)*(x(kk)-x(kk-C)));
321
322 conv = 1;
323
324 while conv>1e-10
```

```

f4(kk) = tand((Theta(kk-C)+Theta(kk))/2);

f1(kk) = tand((Theta(kk-1)+mu(kk-1)+Theta(kk)+mu(kk))/2);
f2(kk) = 0.5*(1/(tand(mu(kk-1))*M(kk-1)*(1+(k-1)/2*M(kk-1)^2))+...
   +1/(tand(mu(kk))*M(kk)*(1+(k-1)/2*M(kk)^2)));
f3(kk) = 0.5*(sind(Theta(kk-1))*sind(mu(kk-1))/(r(kk-1)*cosd(Theta(kk-1)+mu(kk-1)))+...
   +sind(Theta(kk))*sind(mu(kk))/(r(kk)*cosd(Theta(kk-1)+mu(kk))));


AA = [1 -f1(kk) ; 1 -f4(kk)];
BB = [-f1(kk)*x(kk-1)+r(kk-1) ; -f4(kk)*x(kk-C)+r(kk-C)];
r_x = AA\BB;

conv = abs(x(kk)-r_x(2));

r(kk) = r_x(1);
x(kk) = r_x(2);
M(kk) = M(kk-C);
mu(kk) = asind(1/M(kk));

Theta(kk) = Theta(kk-1)+radtodeg(f2(kk)*(M(kk)-M(kk-C))-HULP*f3(kk)*(x(kk)-x(kk-1)));
end



if end1 == 1

   f4(unique(SAVE)) = mean(f4(unique(SAVE)));
   return
end
end
```

```
clc
close all
clear all

%% parameters
Char = 2000;
Pressdiff =120;
R = 208;
k = 1.666666;
H=0.775*10^-3;
HULP = 1; % 0 is PLANAR, 1 is AXISYMMMETRIC

M = zeros(1,Char^2/10^2);
nu = zeros(1,Char^2/10^2);
r = zeros(1,Char^2/10^2);
x = zeros(1,Char^2/10^2);
Theta = zeros(1,Char^2/10^2);

M(1) = 1;
klas = 0;
P_stag = (1+(k-1)/2*M(1)^2)^-(k/(k-1)); % isentropic relation for stagnation pressure ...
    ratio
P_tot = 1/(Pressdiff*P_stag);

M(Char+1) = (2/(k-1)*(P_tot^((1-k)./k)-1))^(1/2); % Mach number in region #Char+1

[M(1),nu(1),mu(1)] =flowprandtlmeyer(k,M(1),'mach');
[M(1+Char),nu(1+Char),mu(1+Char)] =flowprandtlmeyer(k,M(1+Char),'mach');

Theta(Char+1) = nu(Char+1) - nu(1);
D_Theta = ((Theta(Char+1))/(Char^1.1));

for i = 1:Char-1
   Theta(i+1) = (Theta(1)+D_Theta*(i^1.1));
   nu(i+1) = (nu(1) + D_Theta*(i^1.1));

```

```
    [¬,¬,mu(i+1)] =flowprandtlmeyer(k,nu(i+1),'nu');

end

FI = Char/100;
D_Theta = Theta(FI)/(FI^4);

[M(1),nu(1),mu(1)] =flowprandtlmeyer(k,M(1),'mach');
[M(1+Char),nu(1+Char),mu(1+Char)] =flowprandtlmeyer(k,M(1+Char),'mach');

for i = 1:FI
   Theta(i+1) = (Theta(1)+D_Theta*(i^4));
   nu(i+1) = (nu(1) + D_Theta*(i^4));
      [¬,¬,mu(i+1)] =flowprandtlmeyer(k,nu(i+1),'nu');
end

for i = 1:Char-1
    Theta(i) = (Theta(i+1)+Theta(i))/2;
    mu(i) = (mu(i+1)+mu(i))/2;
end



M = 1./sind(mu);

Char = Char+1;

x(1:Char) = 0;
r(1:Char) = H;


axiJET


% figure(2)
% hold on
% for ii = Start:length(x)
%    plot(x(ii),r(ii),'*')
%    text(x(ii),0.01+r(ii),num2str(ii))
% end
%
% hold off


Begin_1 = S;

figure(1)
xlabel('x [cm]')
ylabel('y [cm]')
hold on
sss = 0;

x_shock = 0.65*sqrt(Pressdiff)*H*2;
r_shock = 0.35*sqrt(Pressdiff)*H/2;

plot(x_shock,r_shock,'o')

S_angle_pre = (atand(f4(SAVE(2)))-Theta(SAVE(2)));
M_a_pre = M(SAVE(2)-1);
def_pre = (atand(1/(((k+1)/2*M_a_pre^2/(M_a_pre^2*sind(S_angle_pre)^2-1)-1)*
...(tand(S_angle_pre)))));
press_pre = (2*k)/(k+1)*(M_a_pre^2*sind(S_angle_pre)^2-(k-1)/(2*k));
dens_pre = 1/((2)/(k+1)*(1/(M_a_pre^2*sind(S_angle_pre)^2)+(k-1)/(2)));
entropy_pre = ((R)/(k-1)*(-log(1/press_pre)+k*log(1/dens_pre)));
M_b_pre = sqrt((1/(tand(S_angle_pre)/(tand(S_angle_pre-def_pre))*
...(k+1)/2-(k-1)/2))/((sind(S_angle_pre-def_pre))^2));
W_a_pre = sqrt(1/(1+(2/(k-1))*1/M_a_pre^2));
W_b_pre = sqrt(1/(1+(2/(k-1))*1/M_b_pre^2));
dw_dd = 0;
ds_dd = 0;

```

```
BEGINNNN_angle = S_angle_pre;
aaaa = 0;
test = 1;

for S = Begin_1+Char:Char:Begin_1+Char*Char %Begin_1+Char

ss = 1;
aaaa = aaaa + 1;
Start(aaaa) = S;

kk = S;

r(S) = 0;
Theta(S) = 0;
f4 = tand(Theta(S-Char+1)-mu(S-Char+1));
f5 = 1/(tand(mu(S-Char+1))*M(S-Char+1)*(1+(k-1)/2*M(S-Char+1)^2));
f6 = sind(Theta(S-Char+1))*sind(mu(S-Char+1))/...
   (r(S-Char+1)*cosd(Theta(S-Char+1)-mu(S-Char+1)));

x(S) = x(S-Char+1) - r(S-Char+1)/(f4);
M(S) = (degtorad(Theta(S-Char+1)) + HULP*f6*(x(S)-x(S-Char+1)))*(f5) + M(S-Char+1);
mu(S) = asind(1/M(S));

[¬,nu(S-Char+1),¬] =flowprandtlmeyer(k,M(S-Char+1),'mach');

con = 1;

   while con > 1e-10
      f4 = tand((Theta(S-Char+1)-mu(S-Char+1)+Theta(S)-mu(S))/2);
      x_new = x(S-Char+1) - r(S-Char+1)/(f4);

      f5 = 0.5*(1/(tand(mu(S-Char+1))*M(S-Char+1)*(1+(k-1)/2*M(S-Char+1)^2))+
      ...+1/(tand(mu(S))*M(S)*(1+(k-1)/2*M(S)^2)));
      [¬,nu_2,¬] =flowprandtlmeyer(k,M(S),'mach');
      f6 = 0.5*(sind(Theta(S-Char+1))*sind(mu(S-Char+1))/...
         (r(S-Char+1)*cosd(Theta(S-Char+1)-mu(S-Char+1)))- ...
         0.5*cotd(mu(S-Char+1))*(degtorad(nu_2)-degtorad(nu(S-Char+1)))/(x_new-x(S-Char+1)));

      M(S) = (degtorad(Theta(S-Char+1)) + HULP*f6*(x(S)-x(S-Char+1)))*(f5) + M(S-Char+1);
      mu(S) = asind(1/M(S));
      con = abs(x_new-x(S));
      x(S) = x_new;

   end


  while x(kk) > x(kk-1) || kk == S

      kk = kk + 1;
      f1 = tand(Theta(kk-1)+mu(kk-1));
      f2 = 1/(tand(mu(kk-1))*M(kk-1)*(1+(k-1)/2*M(kk-1)^2));
         if r(kk-1) > 0
            f3 = sind(Theta(kk-1))*sind(mu(kk-1))/(r(kk-1)*cosd(Theta(kk-1)+mu(kk-1)));
         else
            f3 = 0;
         end
      f4 = tand(Theta(kk-Char+1)-mu(kk-Char+1));
      f5 = 1/(tand(mu(kk-Char+1))*M(kk-Char+1)*(1+(k-1)/2*M(kk-Char+1)^2));
      f6 = sind(Theta(kk-Char+1))*sind(mu(kk-Char+1))/
      ...(r(kk-Char+1)*cosd(Theta(kk-Char+1)-mu(kk-Char+1)));

      AA = [1 -f1 ; 1 -f4];
      BB = [-f1*x(kk-1)+r(kk-1) ; -f4*x(kk-Char+1)+r(kk-Char+1)];
      r_x = AA\BB;

      r(kk) = r_x(1);
      x(kk) = r_x(2);

      AA = [f2 -1; f5 +1];
      BB = [HULP*f3*(x(kk)-x(kk-1)) - degtorad(Theta(kk-1)) + f2*M(kk-1) ; ...
          HULP*f6*(x(kk)-x(kk-Char+1)) + degtorad(Theta(kk-Char+1)) + f5*M(kk-Char+1) ];
```

```
177         M_T = AA\BB;
178         M(kk) = M_T(1);
179         Theta(kk) = (M_T(2));
180         mu(kk) = asind(1/M(kk));
181         convp = 1;
182 
183         while convp>1e-12
184            f1 = tand((Theta(kk-1)+mu(kk-1)+Theta(kk)+mu(kk))/2);
185            f2 = ...
                   0.5*(1/(tand(mu(kk-1))*M(kk-1)*(1+(k-1)/2*M(kk-1)^2))+1/(tand(mu(kk))*M(kk)*(1+(k-1)/2*M(kk)^2)
186            if r(kk-1) > 0
187               f3 = ...
                       0.5*(sind(Theta(kk-1))*sind(mu(kk-1))/(r(kk-1)*cosd(Theta(kk-1)+mu(kk-1)))+
188               ...+sind(Theta(kk))*sind(mu(kk))/(r(kk)*cosd(Theta(kk-1)+mu(kk))));
189            else
190               [¬,nu_c,mu_c] =flowprandtlmeyer(k,M(kk),'mach');
191               [¬,nu_b,¬] =flowprandtlmeyer(k,M(kk-1),'mach');
192               f3 = 0.5*(sind(Theta(kk))*sind(mu(kk))/(r(kk)*cosd(Theta(kk)+mu(kk)))+
193                 ...+0.5*cotd(mu_c)*(degtorad(nu_c)-degtorad(nu_b))/(x(kk)-x(kk-1)));
194            end
195 
196            f4 = tand((Theta(kk-Char+1)-mu(kk-Char+1)+Theta(kk)-mu(kk))/2);
197            f5 = 0.5*(1/(tand(mu(kk-Char+1))*M(kk-Char+1)*(1+(k-1)/2*M(kk-Char+1)^2))+...+
198               1/(tand(mu(kk))*M(kk)*(1+(k-1)/2*M(kk)^2)));
199            f6 = 0.5*(sind(Theta(kk-Char+1))*sind(mu(kk-Char+1))/...
200               (r(kk-Char+1)*cosd(Theta(kk-Char+1)-mu(kk-Char+1)))+...
201               +sind(Theta(kk))*sind(mu(kk))/(r(kk)*cosd(Theta(kk)-mu(kk))));
202 
203            AA = [1 -f1 ; 1 -f4];
204            BB = [-f1*x(kk-1)+r(kk-1) ; -f4*x(kk-Char+1)+r(kk-Char+1)];
205            r_x = AA\BB;
206 
207            convp = abs(x(kk)-r_x(2));
208 
209            r(kk) = r_x(1);
210            x(kk) = r_x(2);
211            AA = [f2 -1; f5 +1];
212            BB = [HULP*f3*(x(kk)-x(kk-1)) - degtorad(Theta(kk-1)) + f2*M(kk-1) ; ...
                    HULP*f6*(x(kk)-x(kk-Char+1)) + degtorad(Theta(kk-Char+1)) + ...
                    f5*M(kk-Char+1) ];
213 
214            M_T = AA\BB;
215            M(kk) = M_T(1);
216            Theta(kk) = radtodeg(M_T(2));
217            mu(kk) = asind(1/M(kk));
218         end
219      end
220 
221   Checkker = 1;
222   testaa = 0;
223   S_angle_post = S_angle_pre;
224   kk = kk;
225 
226 
227   while Checkker == 1 ;
228         x = x(1:kk-1);
229         r = r(1:kk-1);
230         Theta = Theta(1:kk-1);
231         mu = mu(1:kk-1);
232         M = M(1:kk-1);
233 
234         Checkker = 0;
235 
236         kk = kk - 1;
237 
238         f1 = tand(Theta(kk-1)+mu(kk-1));
239         f4 = tand(Theta(kk-Char)+S_angle_post);
240 
241 
242         AA = [1 -f1 ; 1 -f4];
243         BB = [-f1*x(kk-1)+r(kk-1) ; -f4*x((kk-Char+1))+r((kk-Char+1))];
```

```
244         r_x = AA\BB;
245
246
247         r(kk) = r_x(1);
248         x(kk) = r_x(2);
249
250         dsdnplus_pre = ...
                (entropy_pre)*cosd(mu(kk-1)+Theta(kk-1))/(sind(mu(kk-1))*(x(kk)-x(kk-1)));
251
252         Theta(kk) = ...
                radtodeg(1/(tand(mu(kk-1))*M(kk-1)*(1+(k-1)/2*M(kk-1)^2))*(M(kk)-M(kk-1)) + ...
                HULP*(x(kk)-x(kk-1))*(-sind(Theta(kk-1))*sind(mu(kk-1))/
253         ...(r(kk-1)*cosd(Theta(kk-1)+mu(kk-1)))+dsdnplus_pre*sind(mu(kk-1))^3/(cosd(mu(kk-1)+Theta(kk-1)
254
255         M_a_post = M(kk-1);
256         def_post = Theta(kk) - Theta(kk-1);
257
258         S_angle_post = -radtodeg(obliquerelations('mach', M_a_post, ...
                'theta',abs(degtorad(def_post)),k));
259
260         press_post = (2*k)/(k+1)*(M_a_post^2*sind(S_angle_post)^2-(k-1)/(2*k));
261         dens_post = 1/((2)/(k+1)*(1/(M_a_post^2*sind(S_angle_post)^2)+(k-1)/(2)));
262         entropy_post = ((R)/(k-1)*(-log(1/press_post)+k*log(1/dens_post)));
263         M(kk) = sqrt((1/(tand((-S_angle_post))/(tand((-S_angle_post)-(def_post)))*...
264            (k+1)/2-(k-1)/2))/((sind((-S_angle_post)-(def_post)))^2));
265
266
267         convss = 1;
268         testaa = 0;
269
270         while convss > 10^-12
271
272         f1 = tand(Theta(kk-1)+mu(kk-1));
273
274
275
276            f4 = tand((Theta(kk-Char+1)+S_angle_pre+Theta(kk)+S_angle_post)/2);
277
278         AA = [1 -f1 ; 1 -f4];
279         BB = [-f1*x(kk-1)+r(kk-1) ; -f4*x(kk-Char+1)+r(kk-Char+1)];
280         r_x = AA\BB;
281
282         convss_new = abs(x(kk)-r_x(2));
283         r(kk) = r_x(1);
284         x(kk) = r_x(2);
285
286         dsdnplus_pre = ...
                (entropy_post)*cosd(mu(kk-1)+Theta(kk-1))/(sind(mu(kk-1))*(x(kk)-x(kk-1)));
287
288         Theta(kk) = ...
                radtodeg(1/(tand(mu(kk-1))*M(kk-1)*(1+(k-1)/2*M(kk-1)^2))*(M(kk)-M(kk-1)) + ...
                HULP*(x(kk)-x(kk-1))*(-sind(Theta(kk-1))*sind(mu(kk-1))/
289         ...(r(kk-1)*cosd(Theta(kk-1)+mu(kk-1)))+dsdnplus_pre*sind(mu(kk-1))^3/(cosd(mu(kk-1)+Theta(kk-1)
290
291         M_a_post = M(kk-1);
292         def_post = Theta(kk) - Theta(kk-1);
293
294         S_angle_post = -radtodeg(obliquerelations('mach', M_a_post, ...
                'theta',abs(degtorad(def_post)),k));
295
296         press_post = (2*k)/(k+1)*(M_a_post^2*sind(S_angle_post)^2-(k-1)/(2*k));
297         dens_post = 1/((2)/(k+1)*(1/(M_a_post^2*sind(S_angle_post)^2)+(k-1)/(2)));
298         entropy_post = ((R)/(k-1)*(-log(1/press_post)+k*log(1/dens_post)));
299         M(kk) = sqrt((1/(tand(S_angle_post)/(tand(S_angle_post+def_pre))*(k+1)/2-(k-1)/2))/
300         ...((sind(S_angle_post+def_pre))^2));
301
302
303         convss = convss_new;
304         end
305
306   end
```

```
307
308         S_angle_pre = S_angle_post;
309         M_a_pre = M_a_post;
310         def_pre = def_post;
311         press_pre = press_post;
312         dens_pre = dens_post;
313         entropy_pre = entropy_post
314         %M(kk) = M_b_post;
315         %mu(kk) = asind(1/M(kk));
316
317         SAVE(1) = kk;
318
319      sss = sss + 1;
320      SHOCK(sss) = kk;
321
322      plot(x(SHOCK(sss)),r(SHOCK(sss)),'*')
323      text(x(SHOCK(sss)),0.0001+r(SHOCK(sss)),num2str(SHOCK(sss)))
324      drawnow
325      S_angle_pre
326      kk = kk + 1;
327         f1 = tand(Theta(kk-1)+mu(kk-1));
328         f2 = 1/(tand(mu(kk-1))*M(kk-1)*(1+(k-1)/2*M(kk-1)^2));
329            if r(kk-1) > 0
330               f3 = sind(Theta(kk-1))*sind(mu(kk-1))/(r(kk-1)*cosd(Theta(kk-1)+mu(kk-1)));
331            else
332               f3 = 0;
333            end
334         f4 = tand(Theta(kk-Char+1)-mu(kk-Char+1));
335         f5 = 1/(tand(mu(kk-Char+1))*M(kk-Char+1)*(1+(k-1)/2*M(kk-Char+1)^2));
336         f6 = sind(Theta(kk-Char+1))*sind(mu(kk-Char+1))/...
337            (r(kk-Char+1)*cosd(Theta(kk-Char+1)-mu(kk-Char+1)));
338
339         AA = [1 -f1 ; 1 -f4];
340         BB = [-f1*x(kk-1)+r(kk-1) ; -f4*x(kk-Char+1)+r(kk-Char+1)];
341         r_x = AA\BB;
342
343         r(kk) = r_x(1);
344         x(kk) = r_x(2);
345
346         AA = [f2 -1; f5 +1];
347         BB = [HULP*f3*(x(kk)-x(kk-1)) - degtorad(Theta(kk-1)) + f2*M(kk-1) ; ...
              HULP*f6*(x(kk)-x(kk-Char+1)) + degtorad(Theta(kk-Char+1)) + f5*M(kk-Char+1) ];
348         M_T = AA\BB;
349         M(kk) = M_T(1);
350         Theta(kk) = (M_T(2));
351         mu(kk) = asind(1/M(kk));
352         convp = 1;
353
354         while convp>1e-12
355            f1 = tand((Theta(kk-1)+mu(kk-1)+Theta(kk)+mu(kk))/2);
356            f2 = 0.5*(1/(tand(mu(kk-1))*M(kk-1)*(1+(k-1)/2*M(kk-1)^2))+...
357            +1/(tand(mu(kk))*M(kk)*(1+(k-1)/2*M(kk)^2)));
358            if r(kk-1) > 0
359               f3 = 0.5*(sind(Theta(kk-1))*sind(mu(kk-1))/(r(kk-1)*cosd(Theta(kk-1)+...
360                  +mu(kk-1)))+sind(Theta(kk))*sind(mu(kk))/(r(kk)*cosd(Theta(kk-1)+mu(kk))));
361            else
362               [¬,nu_c,mu_c] =flowprandtlmeyer(k,M(kk),'mach');
363               [¬,nu_b,¬] =flowprandtlmeyer(k,M(kk-1),'mach');
364               f3 = 0.5*(sind(Theta(kk))*sind(mu(kk))/(r(kk)*cosd(Theta(kk)+mu(kk)))+...
365               +0.5*cotd(mu_c)*(degtorad(nu_c)-degtorad(nu_b))/(x(kk)-x(kk-1)));
366            end
367
368            f4 = tand((Theta(kk-Char+1)-mu(kk-Char+1)+Theta(kk)-mu(kk))/2);
369            f5 = 0.5*(1/(tand(mu(kk-Char+1))*M(kk-Char+1)*(1+(k-1)/2*M(kk-Char+1)^2))+...
370            +1/(tand(mu(kk))*M(kk)*(1+(k-1)/2*M(kk)^2)));
371            f6 = 0.5*(sind(Theta(kk-Char+1))*sind(mu(kk-Char+1))/...
372            (r(kk-Char+1)*cosd(Theta(kk-Char+1)-mu(kk-Char+1)))+...
373               +sind(Theta(kk))*sind(mu(kk))/(r(kk)*cosd(Theta(kk)-mu(kk))));
374
375            AA = [1 -f1 ; 1 -f4];
376            BB = [-f1*x(kk-1)+r(kk-1) ; -f4*x(kk-Char+1)+r(kk-Char+1)];
```

```
377             r_x = AA\BB;
378
379             convp = abs(x(kk)-r_x(2));
380
381             r(kk) = r_x(1);
382             x(kk) = r_x(2);
383             AA = [f2 -1; f5 +1];
384             BB = [HULP*f3*(x(kk)-x(kk-1)) - degtorad(Theta(kk-1)) + f2*M(kk-1) ; ...
                    HULP*f6*(x(kk)-x(kk-Char+1)) + degtorad(Theta(kk-Char+1)) + ...
                    f5*M(kk-Char+1) ];
385
386             M_T = AA\BB;
387             M(kk) = M_T(1);
388             Theta(kk) = radtodeg(M_T(2));
389             mu(kk) = asind(1/M(kk));
390         end
391 end
392
393
394
395
396
397 % figure(3)
398 % hold on
399 % for ii = 1:length(x)
400 %    plot(x(ii),r(ii),'*')
401 %    text(x(ii),0.01+r(ii),num2str(ii))
402 % end
403 %
404 % hold off
```

C

APPENDIX C

Wall temperatures for the non-adiabatic case as simulated with STAR-CCM+ in [17].

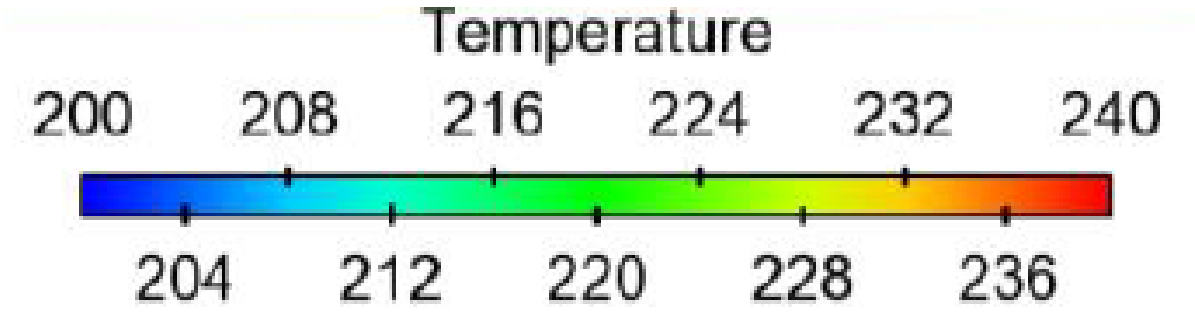

Figure C.1: Legend of the contour plots shown below

Figure C.2: Temperature on the aluminum wall (positive X end). Results obtained from CFD using PR EOS and the $k-\omega$ turbulence model

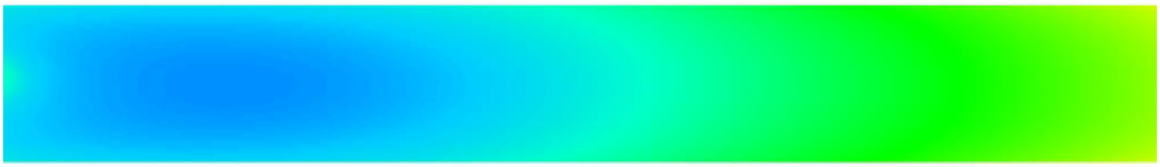

Figure C.3: Temperature on the fused-silica wall at the negative X end. Results obtained from CFD using PR EOS and the $k-\omega$ turbulence model

Figure C.4: Temperature on the poly-urethane wall (positive Y end). Results obtained from CFD using PR EOS and the $k-\omega$ turbulence model

Figure C.5: Temperature on the fused-silica wall (negative Y end). Results obtained from CFD using PR EOS and the $k-\omega$ turbulence model